

COMSAT
Technical Review

Volume 4 Number 1, Spring 1974

COMSAT TECHNICAL REVIEW

Volume 4 Number 1, Spring 1974

Advisory Board Joseph V. Charyk
William W. Hagerty
John V. Harrington
Sidney Metzger

Editorial Board Pier L. Bargellini, Chairman
Simon B. Bennett
S. Browne
S. J. Campanella
N. K. M. Chitre
Denis J. Curtin
Joachim Kaiser
R. W. Kreutel
Helmo Raag
Edmund S. Rittner

Editorial Staff Larry G. Hastings
MANAGING EDITOR
Leonard F. Smith
TECHNICAL EDITOR
Edgar Bolen
PRODUCTION

The COMSAT TECHNICAL REVIEW is published twice a year by the Communications Satellite Corporation (COMSAT). Subscriptions including postage, \$5.00 U.S. per year; single copies, \$3.00 U.S. Bulk rates are available upon request. Remittances for subscriptions should be made payable to the Treasurer, COMSAT, and addressed to COMSAT TECHNICAL REVIEW, Room 5273, 950 L'Enfant Plaza, S. W., Washington, D.C. 20024, U.S.A.

- 1 GRAVITY-GRADIENT TORQUE EFFECTS ON AN INTELSAT IV SPACECRAFT IN TRANSFER ORBIT **V. J. Slabinski** 45-271-1
- 21 STABILIZATION ASPECTS OF A WHEEL ENERGY STORAGE AND ATTITUDE CONTROL SYSTEM FOR GEOSTATIONARY SATELLITES **M. H. Kaplan** 49-271-1
- 41 EFFECTS OF RADIATION ON THE VIOLET SOLAR CELL **R. A. Arndt**
- 53 DEVELOPMENT OF ADVANCED INTERCONNECTORS FOR SOLAR CELLS **D. J. Curtin** AND **W. J. Billerbeck**
- 69 METALLURGICAL EVALUATION OF FABRICATION TECHNOLOGIES FOR HIGH-PRECISION MICROWAVE FILTERS FOR SPACE APPLICATION **J. M. Sandor**
- 91 DOMESTIC AND/OR REGIONAL SERVICES THROUGH INTELSAT IV SATELLITES **J. L. Dicks**
- 119 AN EXPERIMENTAL SHIP-SHORE SATELLITE COMMUNICATIONS DEMONSTRATION **J. Kaiser**
- 139 METHOD FOR COMPUTING THE OPTIMUM POWER BALANCE IN MULTIBEAM SATELLITES **H. J. Meyerhoff**
- 147 REVIEW OF INTELSAT EARTH STATION RF OUT-OF-BAND EMISSION CRITERIA **M. P. Brown, Jr.**
- 169 15.3-GHZ PRECIPITATION ATTENUATION MEASUREMENTS USING A TRANSPORTABLE EARTH STATION AT UTIBE, PANAMA **H. J. Meyerhoff, A. Buige, AND E. A. Robertson**
- 187 CTR NOTE:
RAIN DEPOLARIZATION: THEORY AND EXPERIMENT **R. R. Taur**
- 191 TRANSLATIONS OF ABSTRACTS IN THIS ISSUE
FRENCH 191
SPANISH 197
- 203 ERRATA

Gravity-gradient torque effects on an Intelsat IV spacecraft in transfer orbit

V. J. SLABINSKI

(Manuscript received August 1, 1973)

Abstract

This paper derives the gravity-gradient torque on a dual-spin spacecraft in terms of the mass properties of each section. Elementary functions yield the resulting spin-axis motion in terms of the spacecraft position in its elliptical orbit, along with the spin-axis change per orbit period. Graphs illustrate the spin-axis motion of the INTELSAT IV F-4 spacecraft while in its highly elliptical transfer orbit and in synchronous orbit. The net spin-axis motion in synchronous orbit is a negligible 10^{-4} degree/day.

INTELSAT IV F-4 sun sensor data show the spin-axis direction in space shifted by 0.05° during each perigee passage while in transfer orbit. This agrees with the theoretical value within a measurement precision of 0.01° .

Introduction

The apogee rocket motor of a spin-stabilized INTELSAT communications satellite has its thrust direction fixed along the spacecraft spin axis. Thus,

This paper is based upon work performed at COMSAT under the sponsorship of the International Telecommunications Satellite Organization (INTELSAT). Views expressed in this paper are not necessarily those of INTELSAT.

the spacecraft spin axis must have the proper attitude in space at the time of apogee motor firing so that the rocket thrust can change the elliptical transfer orbit to the desired circular, equatorial, synchronous orbit. Sun and earth sensors are used to determine whether the spacecraft has been maneuvered into the proper attitude for firing. Data must be collected and analyzed during an apogee pass preceding the pass for apogee motor firing to allow time for any additional attitude maneuvers that may be required. Thus, the analysis must allow for any torques that might significantly change the attitude during the time remaining until apogee motor firing. Gravity gradient can produce torques of this kind.

Gravity-gradient torques occur because the end of the spacecraft which is nearer to the earth feels a slightly stronger gravitational pull than the opposite end. Because this torque varies as the inverse cube of the spacecraft distance from the earth's center, its greatest effects occur when the spacecraft passes through the perigee of the transfer orbit. Although the torque near this perigee is small, attitude data from the INTELSAT IV sun sensors are sufficiently precise (0.01°) to show the resulting change in the spin-axis direction for each perigee passage in the transfer orbit.

Theory

Basic torque equation

A derivation similar to that given by Nidey [1] will be used with the following notation: \vec{r} is the position vector of a spacecraft mass element from the earth's center of mass, \vec{r}_s is the position vector of this element from the spacecraft center of mass, and \vec{r}_c is the position vector of the spacecraft center of mass from the earth's center of mass. Hence,

$$\vec{r} = \vec{r}_c + \vec{r}_s \quad (1)$$

The gravitational force $d\vec{F}$ due to the earth's attracting the mass in an element of spacecraft volume dV at \vec{r} is

$$d\vec{F}(\vec{r}) = \rho(\vec{r}) dV \text{grad } \Phi(\vec{r}) \quad (2)$$

where ρ is the spacecraft mass density, and Φ is the earth's gravitational potential (defined as the negative of the potential energy per unit mass of spacecraft). The torque about the spacecraft center of mass due to this force element is $\vec{r}_s \times d\vec{F}$. Integrating the torque over all the spacecraft

volume elements gives the gravitational torque $\vec{\tau}$ about the spacecraft center of mass:

$$\vec{\tau} = \int_V \rho(\vec{r}_s) \vec{r}_s \times \text{grad } \Phi(\vec{r}) dV \quad (3)$$

The gravitational potential for points above the earth's surface is usually expressed in a series of spherical harmonics:

$$\Phi(\vec{r}) = \frac{GM_e}{r} \left[1 - J_2 \left(\frac{a_e}{r} \right)^2 \left(\frac{3}{2} \sin^2 \delta - \frac{1}{2} \right) + \dots \right] \quad (4)$$

where G is the universal constant of gravitation, M_e is the earth's mass, a_e is the earth's equatorial radius, and δ is the geocentric latitude of \vec{r} . Only the (second harmonic) term with coefficient J_2 has been explicitly displayed in this equation, since its value is about 10^3 larger than the neglected harmonic terms. A Taylor series expansion of the vector grad Φ about $\vec{r}_s = 0$ is used to evaluate the integral in equation (3) for this potential.

Terms from the k th derivative of grad Φ in the Taylor series expansion will be of the order $(GM_e/r_c^2) (r_s/r_c)^k$ or smaller, and since $(r_s/r_c) < 10^{-5}$, even for spacecraft 63 m long, terms corresponding to large values of k are negligible, and only the lower order terms need to be considered in the expansion. The $k = 0$ term is $[\text{grad } \Phi]_{\vec{r}=\vec{r}_c}$, which is independent of \vec{r}_s ; hence, it contributes nothing to the integral in equation (3) since by the definition of center of mass,

$$\int_V \rho(\vec{r}_s) \vec{r}_s dV = 0 \quad (5)$$

Thus, it is also necessary to consider the $k = 1$ terms in the expansion. Computation of these terms indicates that the contribution of the J_2 and other harmonic terms is less than the contribution of the leading term in Φ by a factor of about J_2 . Since $J_2 = 1.0827 \times 10^{-3}$ for the earth, omission of the harmonic term contribution results in an accuracy of about 0.1 percent in the calculated torque. Thus,

$$\text{grad } \Phi = [\text{grad } \Phi]_{\vec{r}=\vec{r}_c} + \frac{GM_e}{r_c^3} [3\hat{r}_c(\hat{r}_c \cdot \vec{r}_s) - \vec{r}_s] \quad (6)$$

where a caret over a symbol denotes a unit vector. The use of equations (6) and (5) in equation (3) yields

$$\dot{\tau} = -\frac{3GM_e}{r_c^3} \int_V (\hat{r}_c \cdot \hat{r}_s) (\hat{r}_c \times \hat{r}_s) \rho dV \quad (7)$$

which is the basic result obtained by Nidey.

Instantaneous torque on a dual-spin spacecraft

A multispin spacecraft consists of several rigid sections free to rotate relative to each other about a common bearing axis, which will be designated the Z_s axis. The spacecraft is so constructed that each section's center of mass lies on this bearing axis, which is also a principal moment-of-inertia axis for each section. A dual-spin spacecraft is a special case consisting of only two such sections.

An expression for the gravity-gradient torque on a multispin spacecraft will now be developed in terms of the mass properties of each section. First, the position of a volume element in the j th section is expressed in terms of \hat{r}_j , the position vector from the section's center of mass. For volume elements in the j th section,

$$\hat{r}_s = \hat{r}_j + \bar{z}_{s,j} \hat{z}_s \quad (8)$$

where $\bar{z}_{s,j}$ is the displacement of the section's center of mass along the Z_s axis from the mass center of the complete spacecraft. The integral in equation (7) can be replaced by the sum of the integrals from each section and equation (8) can be used to eliminate \hat{r}_s . From the definition of the center of mass,

$$\int_{V_j} \hat{r}_j \rho dV = 0 \quad (9)$$

and since

$$\int_{V_j} \rho dV = m_j \quad (10)$$

where m_j is the mass of the j th section, the result is

$$\begin{aligned} \dot{\tau} = & -\frac{3GM_e}{r_c^3} \left[(\hat{r}_c \cdot \hat{z}_s) (\hat{r}_c \times \hat{z}_s) \sum_j m_j (\bar{z}_{s,j})^2 \right. \\ & \left. + \sum_j \int_{V_j} (\hat{r}_c \cdot \hat{r}_j) (\hat{r}_c \times \hat{r}_j) \rho dV \right] \quad (11) \end{aligned}$$

To evaluate the integral in this equation, the principal moment-of-inertia axes at each section's center of mass are used to define a right-hand Cartesian coordinate system X_j, Y_j, Z_j for that section. Each Z_j axis is taken along the bearing axis, with the positive direction given by $+Z_s$. In the j th section, with respect to the axes for that section,

$$\hat{r}_j = \begin{pmatrix} x_j \\ y_j \\ z_j \end{pmatrix} \quad (12)$$

$$\hat{r}_c = \begin{pmatrix} \hat{r}_c \cdot \hat{x}_j \\ \hat{r}_c \cdot \hat{y}_j \\ \hat{r}_c \cdot \hat{z}_s \end{pmatrix} \quad (13)$$

and

$$\hat{z}_s = \begin{pmatrix} 0 \\ 0 \\ 1 \end{pmatrix} \quad (14)$$

The moments of inertia of the j th section about its coordinate axes are

$$I_{x,j} = \int_{V_j} \rho (y_j^2 + z_j^2) dV \quad (15a)$$

$$I_{y,j} = \int_{V_j} \rho (x_j^2 + z_j^2) dV \quad (15b)$$

$$I_{z,j} = \int_{V_j} \rho (x_j^2 + y_j^2) dV \quad (15c)$$

Since the products of inertia $\int_{V_j} \rho x_j y_j dV$ etc. are zero for these axes, use of equations (12)–(15) in equation (11) yields

$$\begin{aligned} \dot{\tau} = & \frac{3GM_e}{r_c^3} \sum_j \left[(I_{z,j} - I_{y,j}) (\hat{r}_c \cdot \hat{z}_s) (\hat{r}_c \cdot \hat{y}_j) \hat{x}_j \right. \\ & + (I_{x,j} - I_{z,j}) (\hat{r}_c \cdot \hat{x}_j) (\hat{r}_c \cdot \hat{z}_s) \hat{y}_j \\ & \left. + (I_{y,j} - I_{x,j}) (\hat{r}_c \cdot \hat{y}_j) (\hat{r}_c \cdot \hat{x}_j) \hat{z}_s \right] \quad (16) \end{aligned}$$

where

$$I_{x,j} = I_{x,j} + m_j (\bar{z}_{s,j})^2 \quad (17)$$

and

$$I_{y,j} = I_{y,j} + m_j (\bar{z}_{s,j})^2 \quad (18)$$

are the moments of inertia of the j th section about axes through the spacecraft center of mass and parallel to the X_j and Y_j axes, respectively. For a spacecraft consisting of a single section, $z_{s,j} = 0$ and equation (16) reduces to a result given by Roberson [2].

The orientation of the j th spacecraft section with respect to the vertical may be specified in terms of the polar angle θ between the \hat{z}_s and \hat{r}_c directions, and the azimuth ϕ_j of \hat{r}_c about the Z_s axis measured from the $+X_j$ direction positive toward the $+Y_j$ direction so that, in the coordinate system for this section,

$$\hat{r}_c = \begin{pmatrix} \sin \theta \cos \phi_j \\ \sin \theta \sin \phi_j \\ \cos \theta \end{pmatrix} . \quad (19)$$

Equation (16) may then be put in the form

$$\begin{aligned} \dot{\tau} = & -\frac{3GM_e}{2r_c^3} \sum_j \left\{ \left[-(I_{x,j} + I_{y,j} - 2I_{z,j}) \right. \right. \\ & \left. \left. + (I_{y,j} - I_{x,j}) \cos 2\phi_j \right] \hat{\theta} \sin \theta \cos \theta \right. \\ & \left. + \left[(I_{y,j} - I_{x,j}) \sin \theta \sin 2\phi_j \right] (\hat{z}_s \sin \theta - \hat{p} \cos \theta) \right\} \quad (20) \end{aligned}$$

where $\hat{\theta}$ and \hat{p} are unit vectors, common to all sections and orthogonal to \hat{z}_s and each other:

$$\hat{\theta} \sin \theta \equiv \hat{r}_c \times \hat{z}_s \quad (21)$$

$$\hat{p} \equiv \hat{z}_s \times \hat{\theta} . \quad (22)$$

Application to INTELSAT IV

An INTELSAT IV is a dual-spin spacecraft consisting of a spinning section (a solar-cell-covered cylinder spinning about the cylinder axis) and a despun section. A bearing and power transfer assembly constitutes the interface between the two sections whereby the cylinder and bearing axes are coincident. This axis is designated the Z_s axis and its positive direction

points toward the antenna platform end of the spacecraft. This direction is also the (positive) direction of the angular velocity vector for each spacecraft section. Nutation dampers are mounted on the spacecraft to remove any angular velocity component perpendicular to this axis.

A despun motor spins the antenna platform relative to the rotor section to keep the antennas pointing toward the earth. The spacecraft rotational angular momentum \vec{A} is

$$\vec{A} = [I_{z,r} w_r + (I_z - I_{z,r}) w_p] \hat{z}_s \quad (23)$$

where the r subscripts refer to the rotor and the p subscript refers to the antenna platform. I_z is the total spacecraft moment of inertia about the spin axis:

$$I_z = I_{z,r} + I_{z,p} , \quad (24)$$

and w is the angular velocity in inertial space. A change in the despun motor speed ($w_r - w_p$) will affect both w_r and w_p without changing \vec{A} , since the motor exerts only internal torques on the spacecraft. In synchronous orbit w_r is about +50 rev/min, while w_p is about 10^{-3} rev/min (1 rev/orbit period). Hence, the second term in brackets in equation (23) may be neglected when \vec{A} is evaluated for the despun condition.

Table 1 shows that the transverse moments of inertia $I_{x,j}$ and $I_{y,j}$ for each spacecraft section are approximately equal. (Their difference remains nearly constant throughout the spacecraft life.) This near equality makes it possible to neglect in equation (20) the terms for the torque which depend on ϕ_j . In addition, the rapid rotation of a spacecraft section results in a zero average contribution of its ϕ_j terms to the torque; the rotor section is always spinning while the INTELSAT IV F-4 antenna platform is allowed to rotate in inertial space at 4 rev/min for approximately an hour before to an hour after each perigee passage, the time period when the spacecraft is nearest the earth and gravity-gradient torques are largest. Hence, the instantaneous torque contribution represented by the ϕ_j terms in equation (20) gives an imperceptible fluctuation in each section's angular velocity vector.

By neglecting the ϕ_j terms, equation (20) for the torque becomes

$$\dot{\tau} = -\frac{3GM_e}{2r_c^3} (I_x + I_y - 2I_z) (\hat{r}_c \times \hat{z}_s) (\hat{r}_c \cdot \hat{z}_s) \quad (25)$$

TABLE 1. PRINCIPAL AXIS MOMENTS OF INERTIA FOR INTELSAT IV F-4

	Moment of Inertia (kg-m ²)
In transfer orbit (after spin-up)	
Whole spacecraft	
I_x	1,121.0
I_y	1,132.9
About roll axis, I_z	408.6
Spun section	
$I_{x,r}$	392.4
$I_{y,r}$	403.3
About its roll axis, $I_{z,r}$	315.0
Despun section	
$I_{x,p}$	117.8
$I_{y,p}$	123.9
After apogee motor firing	
I_x	693.7
I_y	705.6
I_z	343.7
$I_{z,r}$	250.0
After exhaustion of hydrazine maneuvering fuel	
I_x	655.8
I_y	667.6
I_z	289.6
$I_{z,r}$	195.8

$$\text{where } I_x = \sum_j [I_{x,j} + m_j (\bar{z}_{s,j})^2] \quad (26)$$

$$I_y = \sum_j [I_{y,j} + m_j (\bar{z}_{s,j})^2] \quad (27)$$

I_x and I_y give the moments of inertia of the whole spacecraft about axes through the spacecraft center of mass and parallel to the X_j and Y_j axes, respectively, when the X_j axes of all the sections are parallel. The numerical values of I_x and I_y for a multispin spacecraft are not necessarily unique, since for any section the X_j and Y_j axis labels may be interchanged, but equation (25) requires only the sum ($I_x + I_y$), which is unique.

The torque given by equation (25) has no component along the spin axis so that the magnitude A of the rotational angular momentum remains constant. Equating the torque to the time derivative of the rotational angular momentum yields

$$\dot{\hat{r}} = A \frac{d\hat{z}_s}{dt} \quad (28)$$

as the equation to be solved for the spin-axis motion.

Spin-axis motion in space

In this section, for the purpose of determining the motion of the spin axis in space, a right-hand Cartesian coordinate system XYZ with origin at the earth's center of mass is adopted. The positive Z axis points north along the earth's rotation axis and the positive X axis points toward the vernal equinox. The positive Y axis thus lies in the equatorial plane and points toward a right ascension of 90° . In terms of the right ascension α and declination δ of the spin-axis direction,

$$\hat{z}_s = \begin{pmatrix} \cos \delta \cos \alpha \\ \cos \delta \sin \alpha \\ \sin \delta \end{pmatrix} \quad (29)$$

in this coordinate system.

The satellite position can be expressed in terms of the orbital elements

a = semi-major axis of the elliptical orbit

e = eccentricity

i = inclination of orbit plane to the equator

Ω = right ascension of the ascending node

ω = argument of perigee

ν = true anomaly.

The unit radius vector may be written as

$$\hat{r}_e = \hat{u}_n \cos L + \hat{u}_s \sin L \quad (30)$$

where

$$L = \omega + \nu \quad (31)$$

is the argument of latitude,

$$\hat{u}_n = \begin{pmatrix} \cos \Omega \\ \sin \Omega \\ 0 \end{pmatrix} \quad (32)$$

is a unit vector in the geocentric direction of the node, and

$$\hat{u}_v = \begin{pmatrix} -\cos i \sin \Omega \\ \cos i \cos \Omega \\ \sin i \end{pmatrix} \quad (33)$$

is a unit vector in the orbit plane in the geocentric direction of $L = 90^\circ$ (the north vertex of the orbit plane).

Combining equations (25), (28), and (30) gives

$$\frac{d\hat{z}_s}{dt} = -\frac{3GM_e(I_x + I_y - 2I_z)}{4r_e^3 A} [\hat{u}_1 + 2\hat{u}_2 \cos 2L + 2\hat{u}_3 \sin 2L] \quad (34)$$

$$\text{where } \hat{u}_1 \equiv (\hat{u}_n \cdot \hat{z}_s) (\hat{u}_n \times \hat{z}_s) + (\hat{u}_v \cdot \hat{z}_s) (\hat{u}_v \times \hat{z}_s) \quad (35)$$

$$\hat{u}_2 \equiv \frac{1}{2}[(\hat{u}_n \cdot \hat{z}_s) (\hat{u}_n \times \hat{z}_s) - (\hat{u}_v \cdot \hat{z}_s) (\hat{u}_v \times \hat{z}_s)] \quad (36)$$

$$\hat{u}_3 \equiv \frac{1}{2}[(\hat{u}_n \cdot \hat{z}_s) (\hat{u}_v \times \hat{z}_s) + (\hat{u}_v \cdot \hat{z}_s) (\hat{u}_n \times \hat{z}_s)] \quad (37)$$

The motion of the spin axis during a time interval of several orbit periods is of interest here. Because of the rotor section's high spin rate, the rate of change of \hat{z}_s is small enough to permit the evaluation of equation (34) on the basis of unperturbed satellite orbital motion with little error. The direction of the spin axis changes only slightly during the time interval; hence, the unit spin vector \hat{z}_s may be regarded as constant on the right side of the last four equations. Thus, the vectors \hat{u}_1 , \hat{u}_2 , and \hat{u}_3 may be assumed to be constant in equation (34), and they may be evaluated for any convenient time within the time interval.

For unperturbed motion, Kepler's First Law gives

$$r_e = \frac{a(1 - e^2)}{1 + (e \cos \omega) \cos L + (e \sin \omega) \sin L} \quad (38)$$

which may be used to eliminate r_e from equation (34). Kepler's Second Law gives

$$\frac{dL}{dt} = n \left(\frac{a}{r_e}\right)^2 \sqrt{1 - e^2} \quad (39)$$

where n is the mean motion (2π rad/orbit period) given by Kepler's Third Law,

$$n^2 a^3 = GM_e \quad (40)$$

Equation (39) makes it possible to integrate equation (34) by changing the variable of integration from t to L :

$$\begin{aligned} \hat{z}_s - (\hat{z}_s)_{t=t_0} &= \int_{L=L_0}^L \frac{d\hat{z}_s}{dt} \left(\frac{dt}{dL}\right) dL \\ &= -\frac{3n(I_x + I_y - 2I_z)}{4A(1 - e^2)^{3/2}} \left[\hat{u}_1 \{L + (e \cos \omega) \sin L \right. \\ &\quad \left. - (e \sin \omega) \cos L\} + \hat{u}_2 \{\sin 2L \right. \\ &\quad \left. + e \cos \omega (\sin L + \frac{1}{3} \sin 3L) \right. \\ &\quad \left. + e \sin \omega (\cos L - \frac{1}{3} \cos 3L) \right. \\ &\quad \left. + \hat{u}_3 \{-\cos 2L - e \cos \omega (\cos L + \frac{1}{3} \cos 3L) \right. \\ &\quad \left. + e \sin \omega (\sin L - \frac{1}{3} \sin 3L)\} \right]_{L_0}^L \quad (41) \end{aligned}$$

This equation gives the spin axis direction at a time t in terms of the unit spin axis at some epoch t_0 and the argument of latitude values L and L_0 corresponding to the two times. Although \hat{z}_s at time t computed from this last equation differs slightly from a unit vector because the vectors \hat{u}_1 , \hat{u}_2 , and \hat{u}_3 have been treated as constants in integrating equation (34), \hat{z}_s gives the spin axis direction with good accuracy.

Net change in spin axis per orbit period

Sometimes the net displacement $\Delta\hat{z}_s$ of the unit spin-axis vector over one orbital period is of interest, and it can be found by evaluating equation (41) with $L = L_0 + 2\pi$ rad used for the upper limit. The result is

$$\Delta\hat{z}_s = - \left[\frac{\Psi}{\hat{u}_w \cdot \hat{z}_s} \right] \hat{u}_1 \quad (42)$$

$$\text{where} \quad \Psi \equiv \frac{3\pi n(I_x + I_y - 2I_z)}{2A(1 - e^2)^{3/2}} (\hat{u}_w \cdot \hat{z}_s) \quad (43)$$

Now \hat{z}_s can be expressed in terms of its components along three mutually orthogonal unit vectors as

$$\hat{z}_s = (\hat{u}_n \cdot \hat{z}_s) \hat{u}_n + (\hat{u}_v \cdot \hat{z}_s) \hat{u}_v + (\hat{u}_w \cdot \hat{z}_s) \hat{u}_w \quad (44)$$

where

$$\begin{aligned} \hat{u}_w &\equiv \hat{u}_n \times \hat{u}_v \\ &= \begin{pmatrix} \sin i \sin \Omega \\ -\sin i \cos \Omega \\ \cos i \end{pmatrix} \end{aligned} \quad (45)$$

is a unit vector normal to the orbit plane. The cross product of equation (44) with \hat{z}_s yields

$$\begin{aligned} 0 &= (\hat{u}_n \cdot \hat{z}_s) (\hat{u}_n \times \hat{z}_s) + (\hat{u}_v \cdot \hat{z}_s) (\hat{u}_v \times \hat{z}_s) \\ &+ (\hat{u}_w \cdot \hat{z}_s) (\hat{u}_w \times \hat{z}_s) \end{aligned} \quad (46)$$

Combining this equation with equation (35) gives

$$\vec{u}_1 = -(\hat{u}_w \cdot \hat{z}_s) (\hat{u}_w \times \hat{z}_s) \quad (47)$$

hence, equation (42) becomes

$$\Delta \hat{z}_s = \Psi (\hat{u}_w \times \hat{z}_s) \quad (48)$$

This result also follows from the expressions given by Thomas and Cappellari [3] for the gravity-gradient torque time averaged over one orbit period.

Summary of spin-axis motion equations

The following procedure is used to compute the spin-axis motion in space in the presence of gravity-gradient torques. Equation (29) is used to compute the components of a unit vector \hat{z}_s along the spin axis at some initial time t_0 , and equation (23) is used to compute the magnitude A of the spacecraft's rotational angular momentum. If the moments of inertia I_x , I_y , and I_z of the whole spacecraft are not given, they may be computed from the mass properties of the rotor and antenna platform sections using equations (26), (27), and (24).

To find \hat{z}_s at other times t within a few orbit periods of t_0 , equations (32) and (33) are used to compute the unit vectors \hat{u}_n and \hat{u}_v from the orbital elements, which in turn make it possible to compute the vectors \vec{u}_1 , \vec{u}_2 , and \vec{u}_3 from equations (35)–(37) using \hat{z}_s for the initial time. Once the arguments of latitudes L and L_0 (in radians) at times t and t_0 are known (where the difference $L - L_0$ reflects any completed orbital revolutions of the earth between the times), equation (41) gives a vector \hat{z}_s along the spin axis at time t .

To find the net displacement $\Delta \hat{z}_s$ of the unit spin-axis vector over one orbital period, equation (45) is used to compute the unit orbit normal \hat{u}_w and equation (43) is used to obtain the angle Ψ in radians. Equation (48) then yields $\Delta \hat{z}_s$. Equation (48) shows that the net effect of gravity-gradient torques on a spacecraft such as INTELSAT IV over one orbital period is a rotation of the spin-axis direction through a polar angle Ψ about the orbit normal. A positive Ψ value indicates a spin-axis rotation in the direction of orbital motion. The magnitude of $\Delta \hat{z}_s$ gives the net great circle change in the spin-axis direction. This magnitude is proportional to $\sin 2\beta$, where β is the angle between the spin-axis direction and the orbit normal. It should be noted that the net change does not depend on the perigee position!

The net change ΔH in the solar aspect angle H over one orbital period due to gravity-gradient torques can be determined once $\Delta \hat{z}_s$ has been found. The solar aspect angle is the angle between the spin-axis direction and the direction of the sun from the spacecraft:

$$\cos H = \hat{h} \cdot \hat{z}_s \quad (49)$$

where \hat{h} is a unit vector toward the sun:

$$\hat{h} = \begin{pmatrix} \cos \delta_h \cos \alpha_h \\ \cos \delta_h \sin \alpha_h \\ \sin \delta_h \end{pmatrix} \quad (50)$$

and α_h and δ_h are, respectively, the apparent right ascension and declination of the sun. Once H has been found from these two equations ($0 \leq H \leq \pi$ rad), ΔH is obtained from the differential of equation (49):

$$\Delta H = -\frac{\hat{h} \cdot \Delta \hat{z}_s}{\sin H} \quad (51)$$

Comparison of theory with attitude data

Attitude data collected during the transfer orbit of the INTELSAT IV F-4 launch illustrate the effect of gravity-gradient torques because of the long time interval between satellite maneuvers. Tables 1 and 2 provide the basic orbital and spin-axis data used in equation (41) to predict the spin-axis motion under gravity-gradient torques. Figure 1 shows the predicted spin-axis motion in space for INTELSAT IV F-4, but the motion illustrated is typical of any INTELSAT IV spacecraft in transfer orbit. This figure shows that most of the spin-axis motion occurs from one hour before to one hour after perigee passage. The spin axis moves only 0.004° during the four hours before or after an apogee passage. The net spin-axis displacement over one orbital period (apogee to apogee) is 0.053° .

TABLE 2. ORBITAL ELEMENTS AND SPIN DATA USED IN TORQUE ANALYSIS

	INTELSAT IV F-4 Transfer Orbit	Geostationary Orbit Example	
Epoch of elements UT	1972 Jan 23 ^d 07 ^h	—	
a (km)	24,553	42,160	
e	0.717645	0.0	
i (deg)	28.164	0.0	
Ω (deg)	296.643	0.0	
ω (deg)	178.772	0.0	
Mean anomaly (deg)	217.12	0.0	
Orbit period (min)	638.14	1,436	
Epoch of spin axis UT	1972 Jan 23 ^d 17 ^h	1972 Jan 24 ^d 13 ^h	—
Right ascension, α_s (deg)	25.38	24.40	0.0
Declination, δ_s (deg)	-26.40	-24.43	89.5
Spin rate, ω_r (rev/min)	50.15	50.13	50.0
(rad/s)	5.25	5.25	5.24
Application	Figure 2	Figure 3	Figure 4

Figure 1 shows that two cusps occur in the spin-axis path during each orbital period. A cusp occurs when the torque reverses direction. This reversal occurs when the radius vector \vec{r}_e to the satellite is perpendicular to the spin axis \hat{z}_s , since equation (25) for the instantaneous torque involves a

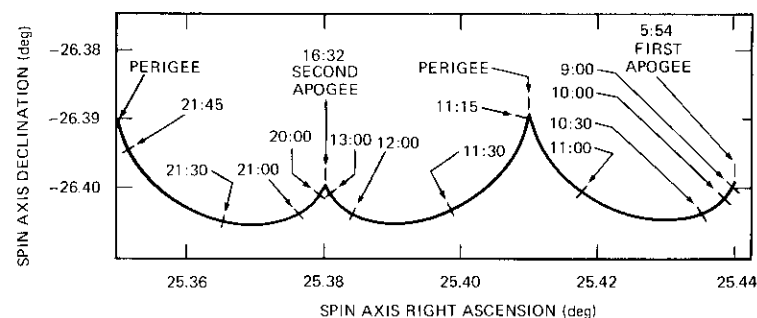


Figure 1. Spin-Axis Motion Caused by Gravity-Gradient Torque for INTELSAT IV F-4 in Transfer Orbit (Labels along the spin-axis path give the time in hours:minutes since 1972 Jan. 23^d0^h UT.)

vector dot product which changes sign and reverses the torque direction at such times. Since the vector \vec{r}_e sweeps out a plane in space during each orbital period, it is perpendicular to \hat{z}_s twice each period, giving two cusps per period to the spin-axis motion in general. The cusps occur near perigee and apogee in Figure 1 only because the spacecraft is in the proper attitude for apogee motor firing, which requires the spin axis to be nearly perpendicular to the line of apsides.

Figures 2 and 3 compare sun sensor data with the theoretical spin-axis motion. These graphs give only the first good aspect angle measurement in every 12-minute time interval. Gaps occur in the data near perigee, when the satellite is not within view of any of the tracking stations.

The dotted lines indicate the linear decrease in the aspect angle due solely to the sun's apparent motion across the celestial sphere at about $1^\circ/\text{day}$. The departure of the data from these dotted lines near perigee, where the gravity-gradient torque has its greatest effect, is readily apparent. The solid lines include the theoretical gravity-gradient effects and give a good fit to all of the data. In Figure 2, the 0.001° offset of the solid line below the data is due to a constant systematic error (measurement bias) in the data.

The theoretical analysis used for these graphs neglects spin-axis motion caused by solar radiation torque, which can precess the axis at about $0.005^\circ/\text{period}$. Solar radiation torque may be omitted from Figures 2 and 3, since this torque rotates the spin axis about the sun's direction as an axis, which introduces no direct change in the sun sensor data.

Two other torques which might be invoked to explain the observed spin-axis motion near perigee are aerodynamic torque and magnetic

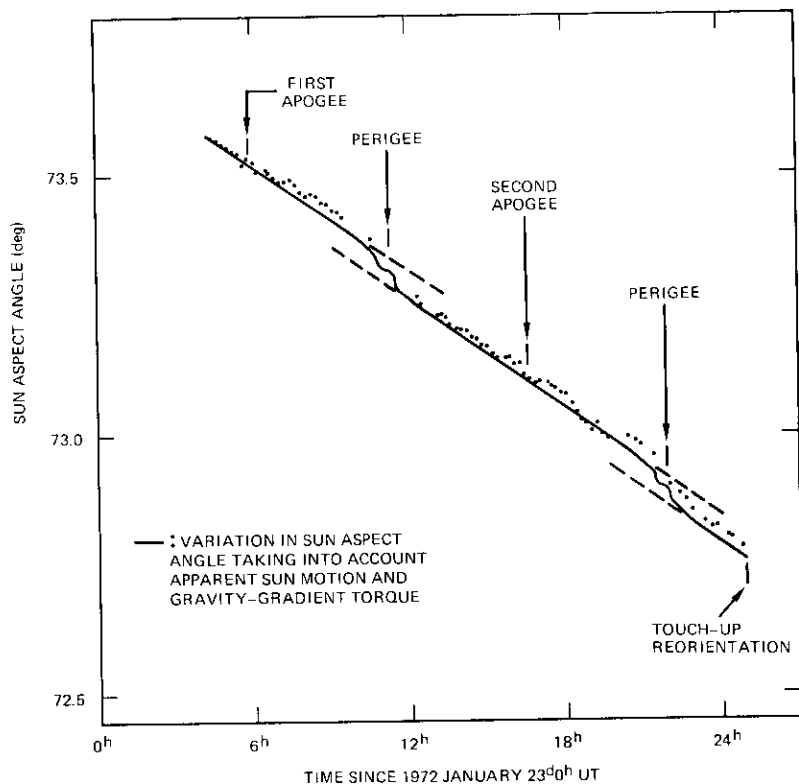


Figure 2. Comparison of Sun Sensor Measurements with Theory for INTELSAT IV F-4 from the End of Nutation Damper Testing to the "Touch-up" Reorientation of the Spin Axis

torque, since the atmospheric density and the geomagnetic field strength are highest along this part of the orbit. Calculations indicate that each torque would move the spin axis of an INTELSAT IV less than 0.002° on each perigee pass. It can then be concluded that the observed spin-axis change near perigee of the transfer orbit is due to the gravity-gradient torque, and that the scatter of the aspect angle data about the theoretical curves in Figures 2 and 3 may be attributed to random measurement errors.

Finally, Figure 4 shows the expected spin-axis motion due to gravity-gradient torques for a satellite in geostationary orbit. This figure uses spacecraft data from Table 1 for INTELSAT IV F-4 immediately after apogee

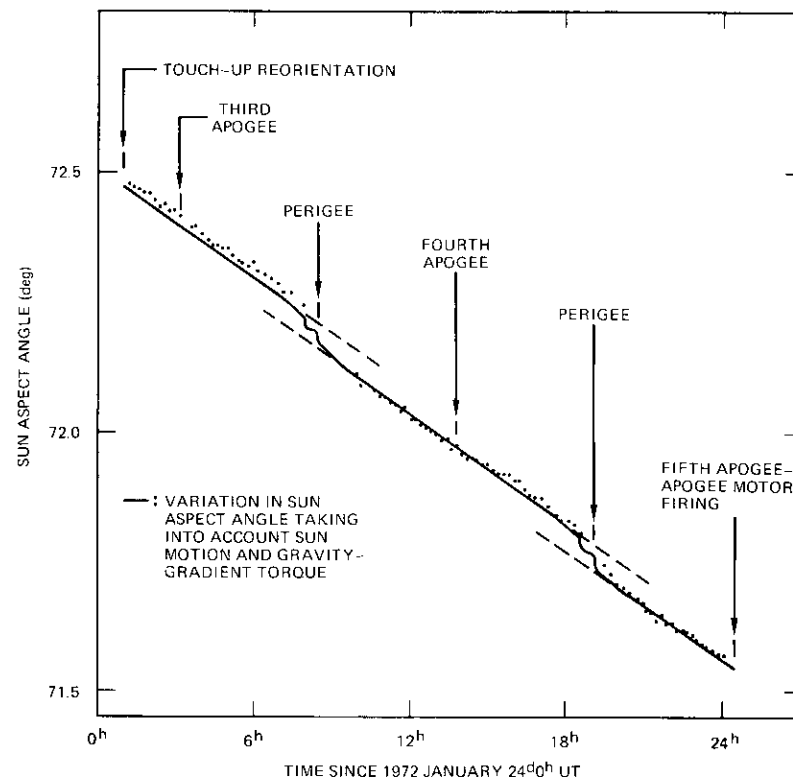


Figure 3. Comparison of Sun Sensor Measurements with Theory for INTELSAT IV F-4 from the "Touch-up" Reorientation of the Spin Axis to Apogee Motor Firing

motor firing, and orbital data from Table 2. The spin axis has its maximum allowed 0.5° offset from the orbit normal to maximize the torque. This figure shows that the net displacement of the spin axis over one day is a negligible 10^{-4} degree.

For an INTELSAT IV in synchronous orbit, the change in its moments of inertia with depletion of the hydrazine maneuvering fuel results in an increased spin-axis motion due to gravity-gradient torques. If the moment of inertia values from Table 1 for INTELSAT IV F-4 after exhaustion of its hydrazine fuel had been used for Figure 4, the spin-axis motion would have been 33 percent larger, but still negligible.

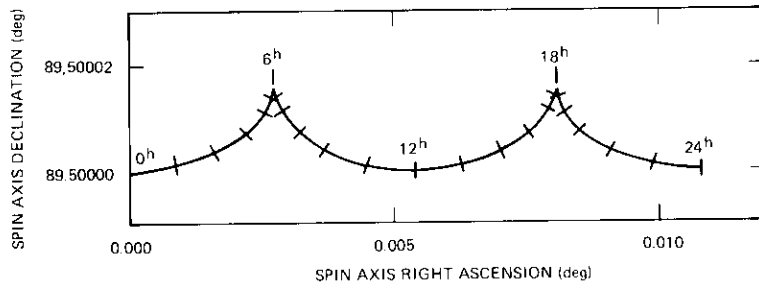


Figure 4. *Maximum Expected Spin-Axis Motion Caused by Gravity-Gradient Torque for an INTELSAT IV in Geostationary Orbit (Tick marks are at 1-hour intervals; the right ascension axis approximates the same arc-distance scale as the declination axis.)*

Conclusions

Sun sensor data from INTELSAT IV spacecraft in transfer orbit clearly show the effect of gravity-gradient torques. The spin-axis shift of only 0.05° per perigee pass is not presently important for transfer orbit operations, since a transient asymmetry in the apogee motor thrust at ignition shifts the spin-axis direction by several tenths of a degree. However, future INTELSATS may have moments of inertia leading to large shifts of the spin axis under gravity-gradient torques.

Gravity-gradient torques can presently be neglected for spin-stabilized INTELSATS in synchronous orbit because

- a. for a given satellite attitude, the torque occurring at synchronous altitude is only 0.4 percent of the torque magnitude at the perigee height (548 km) of the transfer orbit;
- b. the spin axis in synchronous orbit is maintained nearly perpendicular to the orbit plane, an orientation which gives zero torque; and
- c. the torque is more than an order of magnitude less than the solar radiation torque.

References

- [1] Russell A. Nidey, "Gravitational Torque on a Satellite of Arbitrary Shape," *ARS Journal*, Vol. 30, 1960, p. 203, equations (1)–(7).
- [2] Robert E. Roberson, "Alternate Form of a Result by Nidey," *ARS Journal*, Vol. 31, 1961, pp. 1292–1293, equation (8).

- [3] Lewis C. Thomas and James O. Cappellari, "Attitude Determination and Prediction of Spin-Stabilized Satellites," *Bell System Technical Journal*, Vol. 43, 1964, pp. 1678–1680.



Victor J. Slabinski received a B.S. in Physics from Case Institute of Technology in 1961. He was a part-time instructor with the Physics Department at Case Western Reserve University until he received his Ph.D. in 1970. He then became a member of the technical staff of COMSAT's Celestial Mechanics Division, where he is concerned primarily with problems of satellite orbital and attitude mechanics and prediction.

Dr. Slabinski is a member of Tau Beta Pi, Sigma Xi, and the American Astronomical Society.

Index: attitude control, alignment, communications satellites, stabilization, energy storage.

Stabilization aspects of a wheel energy storage and attitude control system for geostationary satellites

M. H. KAPLAN

(Manuscript received October 20, 1973)

Abstract

An investigation of the stabilization aspects of a wheel energy storage and attitude control system is presented for a geostationary, body-stabilized satellite configuration with bias momentum attitude stiffness. Paired counterrotating wheels with net momentum are assumed to be a basic energy storage and attitude control system. Primary power balance relationships are included to illustrate the interaction between energy and momentum parameters. Although it appears that the assumptions regarding material and design technologies do not violate attitude control requirements, critical development problems associated with these assumptions are identified. A slight misalignment of paired wheel axes appears to be the principal concern. In-orbit measurements and corrections of such errors will probably be necessary.

Introduction

Advances in magnetic bearing technology and flywheel design and construction should make possible high-speed wheels with high angular

This paper is based upon work performed at COMSAT Laboratories under the sponsorship of the International Telecommunications Satellite Organization (INTELSAT). Views expressed in the paper are not necessarily those of INTELSAT.

momentum and large kinetic energy storage for application to satellite attitude control and power management. For synchronous communications satellites with operational requirements during eclipse intervals, such wheels may be useful as battery replacements with significant mass and size advantages. Body-stabilized configurations may further use the net angular momentum from pairs of counterrotating wheels for attitude stabilization. Thus, the objective of developing high-speed wheels may be twofold: energy storage and attitude stiffness at a significant mass reduction. Combinations of paired energy storage wheels and single momentum wheels are also possible.

Interactions between energy storage wheels and the attitude control system are discussed as a basis for such efforts as a preliminary evaluation of the concept feasibility with respect to attitude control requirements and operational sequences. Spacecraft compatibility is also considered. Perturbations peculiar to such systems are identified, and responses and corrections discussed. In addition, possible solutions to the critical design problems identified herein are suggested, and power extraction and replenishment balances are discussed with regard to speed control requirements.

The configuration of interest is a body-stabilized geostationary satellite with bias momentum. Horizon and sun sensors are provided for attitude information. It is assumed that the 800-kg (1,760-lbm) vehicle has pitch and roll accuracy requirements of $\pm 0.1^\circ$, while the yaw accuracy is relaxed to $\pm 0.4^\circ$. It is further assumed that the magnitude of solar pressure torque is 3×10^{-6} N-m (2.2×10^{-5} lbf-ft). Since the 4.45-N (1-lbf) latitude control thrusters produce 0.1° pointing scatter, the maximum thruster misalignment torque about any axis is 7×10^{-3} N-m (5.2×10^{-3} lbf-ft). It should be possible to compensate for other thruster misalignments through prelaunch adjustments, and possibly by active mass redistribution. On-orbit programming of attitude thrust sequences during north-south (N-S) firings may also be possible after sufficient observation of actual perturbing torques.

Attitude control system description

High-speed wheels used for energy storage can be applied to attitude control functions when paired in a counterrotating manner with constant differential momentum. This configuration is equivalent to a bias momentum system. Since gimbaling for attitude torque generation does not seem

operationally feasible for high-speed energy storage wheels in magnetic bearings during the time period of interest (late 1970s to mid 1980s), such systems are assumed to perform as fixed-gimbal momentum wheels. Although a pair of counterrotating wheels with zero nominal net momentum can be used for energy storage in conjunction with a separate attitude control system, the basic configuration considered here consists of paired wheels with net bias momentum. Other combinations will be considered as possible alternatives and their performance discussed.

Figure 1 is a basic block diagram of a wheel energy storage and attitude control (WESAC) system. To define functional modes and operational interaction, this scheme will be compared with that of a basic double-gimbaled momentum wheel (DGMW) attitude control system. Both have the same sensor requirements, but there are significant differences in the application of attitude torques and power interaction with attitude control. The DGMW requires more logic to operate roll/yaw gimbals, while WESAC requires somewhat complicated power balancing. Basic fixed wheel systems provide attitude stiffness through large bias momentum and limit yaw errors through gyrocompassing at the orbital rate. The DGMW can compensate for at least part of the solar torques, thus permitting lower bias momentum. Both systems use attitude thrusters for dumping excess momentum. Table 1 lists WESAC system components and functions, including yaw information sun sensors for N-S corrections. The WESAC system also includes a passive nutation damper to eliminate transients during wheel realignment and N-S thrusting.

In the WESAC system, it may be possible to provide compensation of solar torques through the use of magnetic torquers. However, such devices have not been used at synchronous altitudes where their effectiveness is questionable because of the variation in magnitude and direction of the earth's magnetic field. In addition, attitude thrusters will be required during N-S corrections because of probable high misalignment torques. At best, magnetic compensation is expected to be less effective than DGMW techniques which use gimbaling for compensation and attitude jets for momentum dumping. Of course, compensation will work only if the torque variations are at least partially predictable. There will always be some unpredictable portion caused by such factors as mass shift, structural bending, and changing reflectivities. On-orbit reprogramming seems to be a must if maximum compensation is to be achieved. Such a capability results in a lower bias momentum requirement, although this must be selected before flight for DGMW systems.

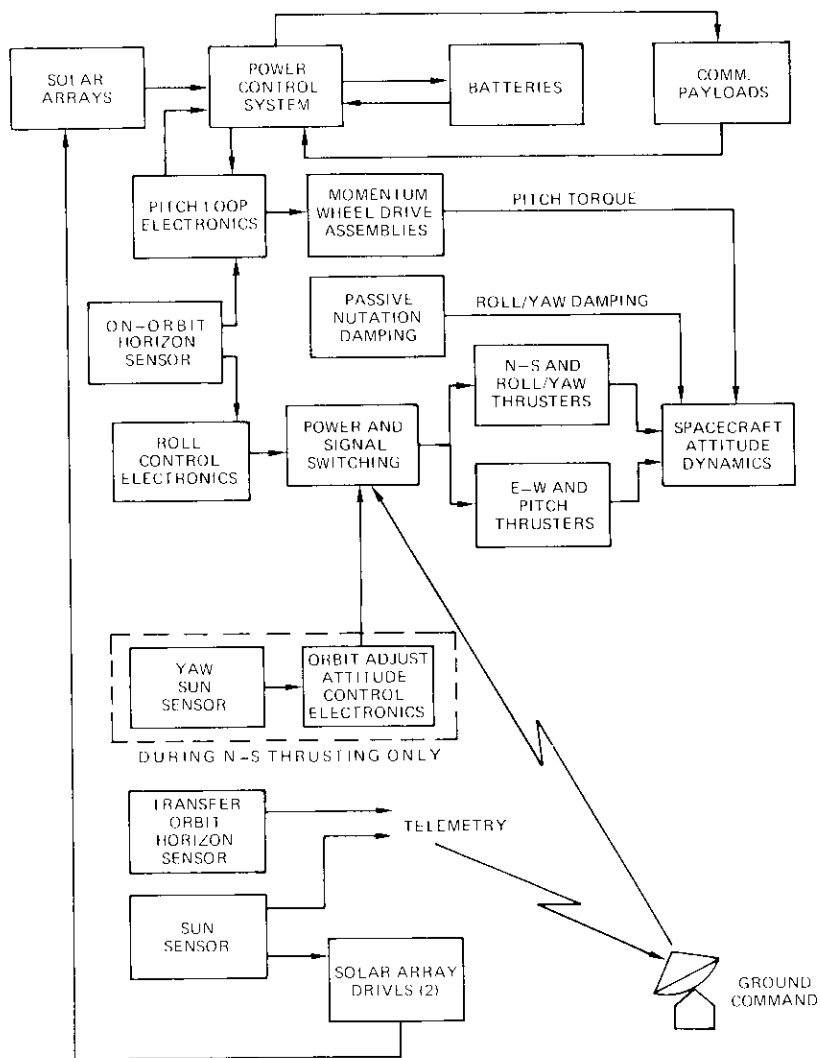


Figure 1. Basic Block Diagram of WESAC System

TABLE 1. CANDIDATE WESAC SYSTEM DESCRIPTION

Component	Function	Comments
Wheel Assembly	gyro stiffness, momentum sink for pitch control, and energy storage	brushless motor drive
Wheel Drive Electronics	pitch position loop and motor drive, and maintenance of bias momentum	must work with alternators and power control loop
Vernier Realignment Gimbal Electronics	detection and measurement of wheel misalignment and correction	error detection and compensation
Propulsion Electronics	transfer orbit reorientation, spin-up and spin-down, momentum adjustment, and orbit adjustment	
On-orbit Horizon Sensor	pitch and roll attitude information	scanning or passive IR
Sun Sensor	attitude determination and thruster gating during transfer orbit	digital, transfer orbit
Transfer Orbit Horizon Sensor	transfer orbit attitude determination	body-mounted, passive, CO ₂ spectral band, transfer orbit only
Passive Nutation Damper	attenuation of nutation	toroidal liquid tube
Sun Sensor for Yaw Information	yaw angle data during N-S thrusting	digital, includes rate logic and electronics

Figure 2 illustrates the relationship between bias momentum, H_N , and yaw error limit, $|\psi|_{\max}$, for different values of compensation for the yaw component of solar torque. It is assumed that $|T_z|_{\max} = 3 \times 10^{-5}$ N-m and that [1]

$$H_N > \frac{|\Delta T_z|}{|\psi|_{\max} \omega_0} \quad (1)$$

where ΔT_z is the unpredictable part of T_z . (The other parameters are defined in the Glossary.) This is the condition required to limit the steady-state value of ψ . A basic WESAC or fixed-gimbal momentum wheel system has no compensation capability and would lie on the uppermost

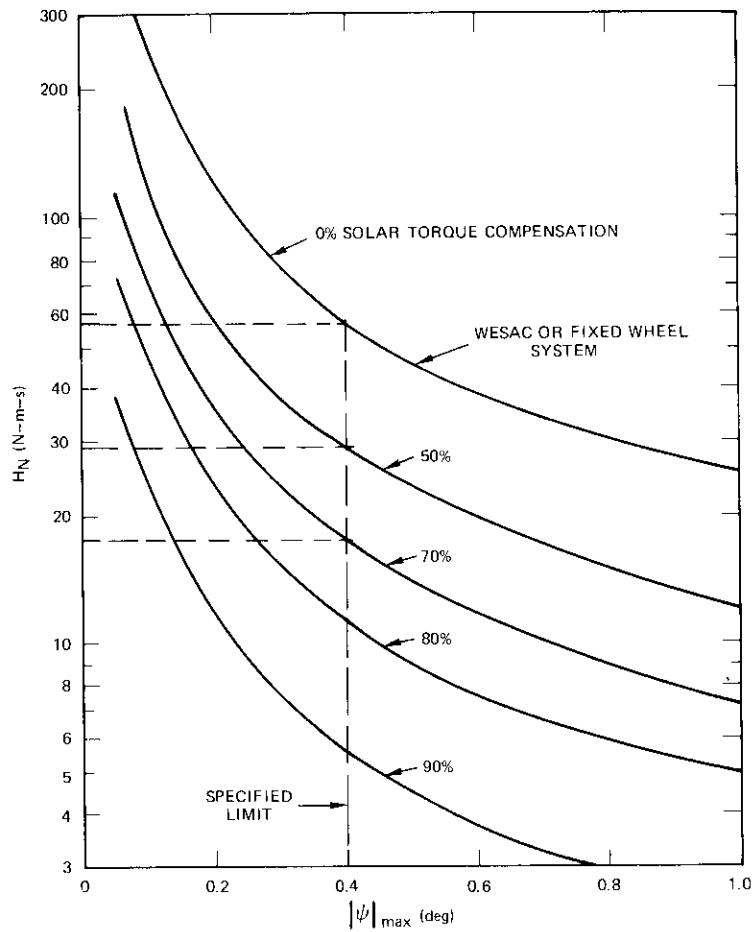


Figure 2. Effect of Compensation on Required Net Momentum

curve. The DGMW system should be capable of 70-percent compensation and the WESAC system with magnetic torquers may be capable of 50-percent compensation. The magnitude of H_N determines the weight of fixed wheel and DGMW systems. However, weight estimation methods for WESAC are only very rough at best; hence, estimates are not attempted here.

Figure 3 presents estimated mass curves for present fixed wheel [2] and DGMW designs based on empirical data [3]. Mass values include the wheel, housing, and associated electronics. Thus, once a value of H_N

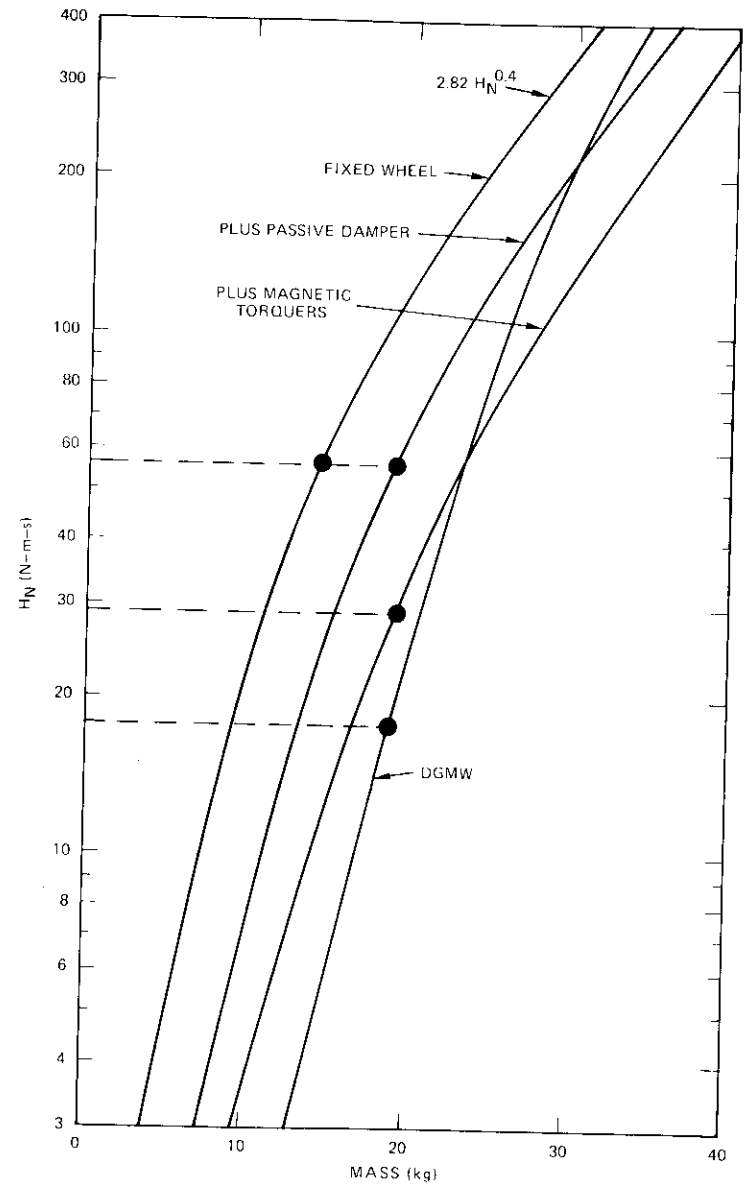


Figure 3. Weight Comparisons of Momentum Wheel Systems

satisfying equation (1) is selected, Figure 3 should provide a mass estimate for a given system. This equation assumes no errors in the compensation mechanism. For the double-gimbaled wheel, this assumption is satisfactory. However, magnetic torquers are effective only for the predictable part of the field; hence, equation (1) is not sufficient for the WESAC system with magnetic torquers. One way to correct this is to adjust $|\Delta T_z|$ accordingly.

An appropriate example, corresponding to a maximum allowable yaw error of 0.4° , is depicted in Figures 2 and 3. Three systems have been considered. WESAC without compensation requires $H_N > 59.0$ N-m-s (43.2 ft-lb-s); WESAC plus magnetic torquers, assumed to be capable of 50-percent compensation, requires $H_N > 29.5$ N-m-s (21.7 ft-lb-s); and DGMW, assumed to be capable of 70-percent compensation, requires $H_N > 17.7$ N-m-s (13.0 ft-lb-s).

Figure 3 gives mass estimates corresponding to current technology for fixed wheel and DGMW systems. The WESAC system would certainly have a lower mass for a given H_N . Thus, a comparison between fixed wheel and DGMW systems should be helpful. The fixed wheel system appears lighter if no nutation damper is used. However, if such a damper is required, then all three systems have about the same weight for $|\psi|_{\max} = 0.4^\circ$. If the assumptions used to form Figure 3 are correct (i.e., if the weight of the double-gimbaled system increases less rapidly than that of the fixed wheel system), then the gimbaled system has a greater weight advantage at higher values of H_N . As a final observation, 90-percent compensation seems possible for the DGMW system if on-orbit reprogramming is available. Hence, such a system would have a definite mass advantage over current fixed wheel designs, but not over WESAC systems. Magnetic torquers are limited by the unpredictability of the magnetic field, however.

Power relationships

For WESAC operation, the balance between the power extraction (or addition) profile and the net momentum is an important consideration. The case of two wheels with equal inertia is of interest here. The power balance between wheels is critical to attitude control. Worst-case power requirements occur at the maximum shadow length (72 min). The power profile over this interval is illustrated in Figure 4, where P_M is the constant power drain in full shadow (totality). The time to totality from initiation of shadow is 128 seconds, or about 2 minutes. Analytically, the total power required can be expressed as

$$\begin{aligned} P &= \frac{P_M}{\tau} t, & 0 \leq t \leq \tau \\ P &= P_M, & \tau \leq t \leq (T - \tau) \\ P &= \frac{P_M}{\tau} (T - t), & (T - \tau) \leq t \leq T \end{aligned}$$

for phases A, B, and C, respectively, where $T_{\max} = 72$ minutes at the equinoxes.

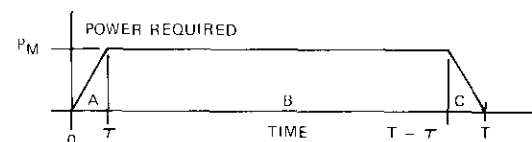


Figure 4. Required Power Profile

The electrical power available from stored kinetic energy in the wheels can be expressed as the rate of change of this energy with an efficiency factor

$$P_a = \eta \frac{d}{dt} \left[\frac{1}{2} I \omega^2 \right] = \frac{1}{2} \eta I \frac{d}{dt} (\omega^2) \quad (2)$$

for each wheel. It is sufficient to consider only phase B, $P = P_M$, to determine momentum and power relationships. Application of equation (2) to each wheel yields

$$\omega_1^2 - \omega_{01}^2 = -\frac{2}{I\eta} \int_0^t P_1 dt$$

$$\omega_2^2 - \omega_{02}^2 = -\frac{2}{I\eta} \int_0^t P_2 dt$$

where power is being extracted from the wheels and $P_M = P_1 + P_2$. Adding these two expressions results in

$$\omega_1^2 + \omega_2^2 = -\frac{2}{I\eta} P_M t + (\omega_{01}^2 + \omega_{02}^2) \quad (3)$$

where $P_M t = E$, the energy extracted over the interval t . Thus, equation (3) gives the combined final state of energy remaining in the wheels. Figure 5 illustrates the relationship between wheel speed and stored energy for

different values of axial inertia. Figure 6 shows the dependence of final wheel speed and angular momentum on initial wheel speed for various values of energy depth of discharge.

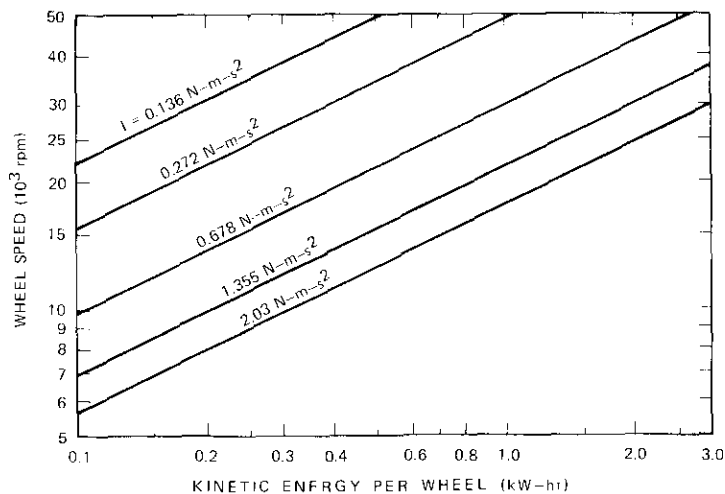


Figure 5. Available Kinetic Energy

Each wheel has a momentum magnitude of $H = I\omega$. The torque associated with power extraction or addition is merely the time rate of change of H :

$$M = \dot{H} = I\dot{\omega}$$

Of course, friction and pitch control torques must be superimposed on this expression. It is essential that a constant net momentum

$$H_p = I(\omega_2 - \omega_1)$$

is maintained at all times. Thus,

$$\dot{H}_1 = I\dot{\omega}_1 = I\dot{\omega}_2 = \dot{H}_2$$

and the torque on wheel 1 must match that on wheel 2; i.e.,

$$M_1 = M_2$$

at all times. Hence,

$$\dot{\omega}_1 = \dot{\omega}_2$$

and

$$\omega_2 - \omega_1 = \omega_{02} - \omega_{01} = \text{const} \stackrel{\Delta}{=} \Omega \quad (4)$$

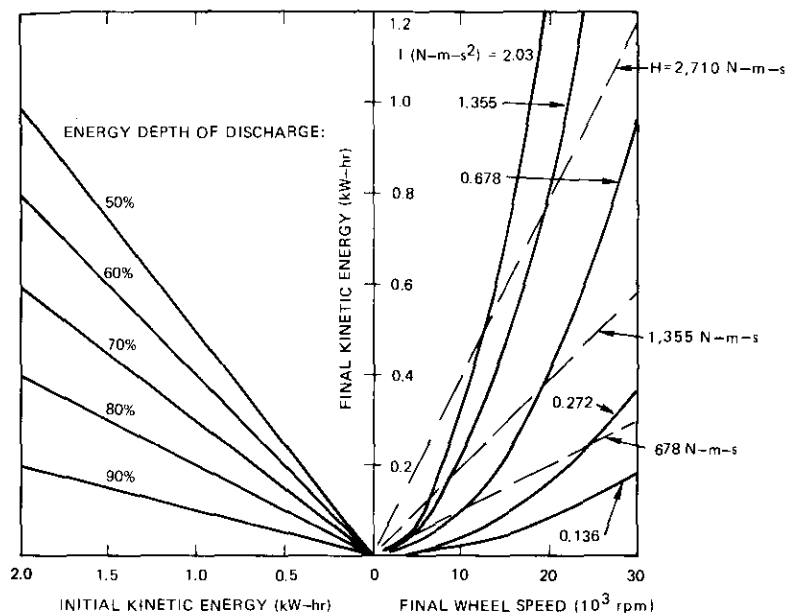


Figure 6. Effect of Energy Extraction on Wheel Speed and Momentum

Equations (3) and (4) can be combined to yield an expression which can be solved for ω_1 :

$$2\omega_1^2 + 2\omega_1\Omega - C = 0$$

where $C \stackrel{\Delta}{=} - (2/I\eta) E + \omega_{01}^2 + \omega_{02}^2 - \Omega^2$. This quadratic is quickly solved for the positive value of ω_1 ,

$$\omega_1 = -\frac{\Omega}{2} + \frac{1}{2} \sqrt{\Omega^2 + 2C}$$

Of course, ω_2 is obtained from equation (4). This derivation is valid for the power extraction phase and ω_{02} is assumed to be greater than ω_{01} .

Consider an example with the following values:

$$I = 0.68 \text{ N-m-s}^2 \text{ (0.5 ft-lb-s}^2\text{)}$$

$$E = 1.0 \text{ kW-hr} = 36.0 \times 10^6 \text{ N-m}$$

$$\eta = 0.5$$

$$H_p = 136 \text{ N-m-s (100 ft-lb-s)}$$

$$\omega_{02} = 36,000 \text{ rpm} = 3,770 \text{ rad/s}$$

In this case,

$$\begin{aligned} \Omega &= 200 \text{ rad/s} = 1,910 \text{ rpm} \\ \omega_{01} &= 36,000 - \Omega = 34,090 \text{ rpm} = 3,570 \text{ rad/s} \\ C &= 6 \times 10^6 \text{ rad/s}^2 \end{aligned}$$

and hence,

$$\begin{aligned} \omega_1 &= 1,635 \text{ rad/s} = 15,613 \text{ rpm} \\ \omega_2 &= 1,835 \text{ rad/s} = 17,523 \text{ rpm} \end{aligned}$$

The energy loss in each wheel is then

$$\begin{aligned} \Delta E_1 &= \frac{1}{2} I(\omega_{01}^2 - \omega_1^2) = 3.43 \times 10^6 \text{ N-m} (2.53 \times 10^6 \text{ ft-lb}) \\ \Delta E_2 &= \frac{1}{2} I(\omega_{02}^2 - \omega_2^2) = 3.68 \times 10^6 \text{ N-m} (2.71 \times 10^6 \text{ ft-lb}) \end{aligned}$$

or

$$\begin{aligned} \Delta E_1 &= 0.953 \text{ kW-hr} \\ \Delta E_2 &= 1.022 \text{ kW-hr} \end{aligned}$$

which can be obtained directly from Figure 5 once ω_1 and ω_2 are known. Figure 6 gives depths of discharge of 79 and 76 percent for wheels 1 and 2, respectively.

Paired wheel attitude equations

To determine the performance, responses, and requirements of a pair of high-speed wheels with net momentum, a set of linearized differential equations has been developed. The derivation is presented here and the equations are compared with those of a doubled-gimbaled momentum wheel. The equations presented here may be applied to realignment responses, variations in net momentum, and development of alignment correction logic.

The general vector equation for a rigid spacecraft is Euler's equation [4]:

$$\vec{T} + \vec{G} = \frac{d\vec{H}}{dt} = \left[\frac{d\vec{H}}{dt} \right]_b + \vec{\omega} \times \vec{H}$$

where $[d\vec{H}/dt]_b$ is the time derivative of \vec{H} with respect to body coordinates. In this case, the spacecraft contains two internal momentum wheels. Hence,

$$\vec{H} = \vec{H}_B + \vec{H}_1 + \vec{H}_2$$

The components of \vec{H}_B , \vec{H}_1 , and \vec{H}_2 (see Figure 7) become

$$\begin{aligned} \vec{H}_B &= I_x \omega_x \vec{e}_x + I_y \omega_y \vec{e}_y + I_z \omega_z \vec{e}_z \\ \vec{H}_1 &= -H_1 \gamma_{z1} \vec{e}_z + H_1 \vec{e}_y + H_1 \gamma_{x1} \vec{e}_x \\ \vec{H}_2 &= H_2 \gamma_{z2} \vec{e}_z - H_2 \vec{e}_y - H_2 \gamma_{x2} \vec{e}_x \end{aligned}$$

where γ_{x1} , γ_{z1} , γ_{x2} , and γ_{z2} are misalignment (or gimbal) components of the wheels. Thus,

$$\begin{aligned} \left[\frac{d\vec{H}}{dt} \right]_b &= [I_x \dot{\omega}_x - (\dot{H}_1 \gamma_{z1} + H_1 \dot{\gamma}_{z1}) + (\dot{H}_2 \gamma_{z2} + H_2 \dot{\gamma}_{z2})] \vec{e}_x \\ &+ [I_y \dot{\omega}_y + \dot{H}_1 - \dot{H}_2] \vec{e}_y \\ &+ [I_z \dot{\omega}_z + (\dot{H}_1 \gamma_{x1} + H_1 \dot{\gamma}_{x1}) - (\dot{H}_2 \gamma_{x2} + H_2 \dot{\gamma}_{x2})] \vec{e}_z \end{aligned}$$

Since $\vec{\omega} = \omega_x \vec{e}_x + \omega_y \vec{e}_y + \omega_z \vec{e}_z$,

$$\begin{aligned} \vec{\omega} \times \vec{H} &= [\omega_y (H_1 \gamma_{z1} - H_2 \gamma_{z2} + I_x \omega_z) - \omega_z (H_1 - H_2 + I_y \omega_y)] \vec{e}_x \\ &+ [\omega_z (H_2 \gamma_{z2} - H_1 \gamma_{z1} + I_x \omega_x) - \omega_x (H_1 \gamma_{z1} - H_2 \gamma_{z2} + I_z \omega_z)] \vec{e}_y \\ &+ [\omega_x (H_1 - H_2 + I_y \omega_y) - \omega_y (H_2 \gamma_{z2} - H_1 \gamma_{z1} + I_x \omega_x)] \vec{e}_z \end{aligned}$$

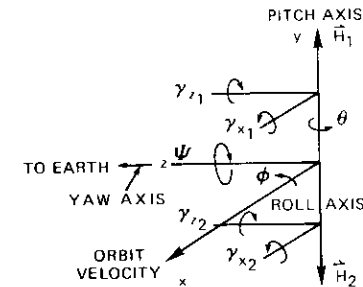


Figure 7. Nomenclature for WESAC Momentum Components

Specializing these vector equations and using the transformations given in Reference 5 yields the desired forms. Ignoring products of small angles, e.g., $\theta \gamma_{z1}$ and $\theta \gamma_{z2}$, and noting that roll, pitch, and yaw angles are ϕ , θ , and ψ , respectively, results in

$$\begin{aligned} T_x &= I_x \ddot{\phi} + [a + \omega_0 (H_2 - H_1)] \dot{\phi} + [b + (H_2 - H_1)] \dot{\psi} \\ &+ (\dot{H}_2 \gamma_{z2} + H_2 \dot{\gamma}_{z2}) - (\dot{H}_1 \gamma_{z1} + H_1 \dot{\gamma}_{z1}) \\ &+ \omega_0 (H_2 \gamma_{x2} - H_1 \gamma_{x1}) \end{aligned} \tag{5}$$

$$T_y = I_y \ddot{\theta} + e\theta - (\dot{H}_2 - \dot{H}_1) \quad (6)$$

$$T_z = I_z \ddot{\psi} + [c + \omega_0(H_2 - H_1)] \psi - [b + (H_2 - H_1)] \dot{\phi} - (\dot{H}_2 \gamma_{x_2} + H_2 \dot{\gamma}_{x_2}) + (\dot{H}_1 \gamma_{x_1} + H_1 \dot{\gamma}_{x_1}) + \omega_0(H_2 \gamma_{z_2} - H_1 \gamma_{z_1}) \quad (7)$$

where

$$\begin{aligned} a &\triangleq 4\omega_0^2(I_y - I_z) \\ b &\triangleq -\omega_0(I_x - I_y + I_z) \\ c &\triangleq \omega_0^2(I_y - I_z) \\ e &\triangleq 3\omega_0^2(I_x - I_z) \end{aligned}$$

Equations (5)–(7) represent a general case in which either wheel may be slightly gimbaled and angular speeds changed. The constants a , b , and c are relatively small for synchronous orbits. Thus, if the net momentum, $H_2 - H_1$, is greater than about 10 N-m-s, these constants can be ignored.

Corresponding equations for a double-gimbaled wheel system (see Figure 8) are similar [4], [5]:

$$\begin{aligned} T_x &= I_x \ddot{\phi} + (a + \omega_0 H_N) \phi + (b + H_N) \dot{\psi} + (\dot{H}_N \gamma_z + H_N \dot{\gamma}_z) + \omega_0 H_N \gamma_x \\ T_y &= I_y \ddot{\theta} + e\theta - \dot{H}_N \\ T_z &= I_z \ddot{\psi} + (c + \omega_0 H_N) \psi - (b + H_N) \dot{\phi} - (\dot{H}_N \gamma_x + H_N \dot{\gamma}_x) + \omega_0 H_N \gamma_z \end{aligned}$$

where

H_N = bias momentum

γ_x, γ_z = gimbal angles and are the control inputs

\dot{H}_N = rate of change of wheel momentum for pitch control.

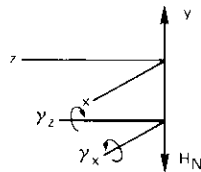


Figure 8. Nomenclature for DGMW System

Since ϕ , θ , ψ , γ_x , and γ_z are assumed to be small, and a and c are small compared to $\omega_0 H_N$, $b \ll H_N$, then the roll and yaw equations for paired wheels are

$$T_x = I_x \ddot{\phi} + \omega_0(H_2 - H_1) \phi + (H_2 - H_1) \dot{\psi} + (H_2 \dot{\gamma}_{x_2} - H_1 \dot{\gamma}_{x_1}) + \omega_0(H_2 \gamma_{x_2} - H_1 \gamma_{x_1}) \quad (8)$$

$$T_z = I_z \ddot{\psi} + \omega_0(H_2 - H_1) \psi - (H_2 - H_1) \dot{\phi} - (H_2 \dot{\gamma}_{x_2} - H_1 \dot{\gamma}_{x_1}) + \omega_0(H_2 \gamma_{z_2} - H_1 \gamma_{z_1}) - (\dot{H}_2 \gamma_{x_2} - \dot{H}_1 \gamma_{x_1}) \quad (9)$$

Equations (8) and (9) can be used to investigate realignment responses, misalignment detection, and alignment correction logic. Equation (6) yields the pitch response to varying net momentum.

Paired wheel problems

The use of two counterrotating momentum wheels, as in the WESAC systems, introduces several unique design and operational problems associated with attitude control performance. Principal areas of concern are identified and discussed in this section.

To study the effects of momentum misalignment on attitude performance, it is sufficient to consider the case of a slight misalignment of one wheel. Assume that wheel 1 has a deviation from the pitch axis of Γ , an angle whose components about the x and z axes are γ_x and γ_z , respectively. Specializing equations (8) and (9) for this torque-free situation yields

$$\begin{aligned} I_x \ddot{\phi} + \omega_0 H_p \phi + H_p \dot{\psi} &= \Gamma_x \\ I_z \ddot{\psi} + \omega_0 H_p \psi - H_p \dot{\phi} &= \Gamma_z \end{aligned}$$

where

$$\begin{aligned} \Gamma_x &\triangleq \omega_0 H_1 \gamma_x \\ \Gamma_z &\triangleq \omega_0 H_1 \gamma_z \end{aligned}$$

and the \dot{H}_1 and \dot{H}_2 terms are assumed to be negligible. Using Laplace transforms results in

$$\begin{aligned} I_x s^2 \Phi + \omega_0 H_p \Phi + H_p s \Psi &= \Gamma_x(s) \\ I_z s^2 \Psi + \omega_0 H_p \Psi - H_p s \Phi &= \Gamma_z(s) \end{aligned}$$

Solving for Ψ and Φ gives

$$\begin{aligned} \Psi &= \frac{(I_x s^2 + \omega_0 H_p) \Gamma_z(s) + H_p s \Gamma_x(s)}{(I_x s^2 + \omega_0 H_p) (I_z s^2 + \omega_0 H_p) + H_p^2 s^2} \\ \Phi &= \frac{(I_z s^2 + \omega_0 H_p) \Gamma_x(s) - H_p s \Gamma_z(s)}{(I_x s^2 + \omega_0 H_p) (I_z s^2 + \omega_0 H_p) + H_p^2 s^2} \end{aligned}$$

For the cases of interest here, $\omega^2 \gg \omega_0^2$ and $H_p \gg \omega_0(I_x + I_z)$; thus, the denominator can be replaced by $I_x I_z (s^2 + \omega^2) (s^2 + \omega_0^2)$. Note that $\omega \triangleq H_p / \sqrt{I_x I_z}$. Taking the inverse and assuming that Γ_x and Γ_z are step functions at $t = 0$ gives

$$\psi(t) = -\frac{I_x \Gamma_z}{H_p^2} (\cos \omega t - \cos \omega_0 t) + \frac{\Gamma_z}{\omega_0 H_p} \left(1 - \cos \omega_0 t + \frac{\omega_0^2}{\omega^2} \cos \omega t \right) + \frac{\Gamma_x}{H_p} \left(\frac{\omega \sin \omega_0 t - \omega_0 \sin \omega t}{\omega_0 \omega} \right)$$

$$\phi(t) = -\frac{I_z \Gamma_x}{H_p^2} (\cos \omega t - \cos \omega_0 t) + \frac{\Gamma_x}{\omega_0 H_p} \left(1 - \cos \omega_0 t + \frac{\omega_0^2}{\omega^2} \cos \omega t \right) + \frac{\Gamma_z}{H_p} \left(\frac{\omega_0 \sin \omega t - \omega \sin \omega_0 t}{\omega_0 \omega} \right)$$

These equations indicate that the effect of misalignment on roll and yaw is a periodic oscillation of "average" magnitude

$$|\psi|_{\max} \sim \frac{\Gamma_z}{\omega_0 H_p} + \frac{\Gamma_x}{\omega_0 H_p}$$

$$|\phi|_{\max} \sim \frac{\Gamma_x}{\omega_0 H_p} + \frac{\Gamma_z}{\omega_0 H_p}$$

Consider, for example, the case in which $\gamma_x = 0$, $\gamma_z = \Gamma = 0.1^\circ$, and $\omega_0 = 7.28 \times 10^{-5}$ rad/s. If the wheels are at the maximum energy storage state and the values of I and ω_{02} appearing in the previous example are used, then $H_1 = 2,428$ N-m-s (1,785 ft-lb-s) and $H_p = 136$ N-m-s (100 ft-lb-s). Calculation results in

$$\Gamma_z = 3.08 \times 10^{-4} \text{ N-m } (2.27 \times 10^{-4} \text{ ft-lb})$$

$$\omega = 0.136 \text{ rad/s}$$

which lead to

$$|\psi|_{\max} = 1.8^\circ$$

$$|\phi|_{\max} = 1.8^\circ$$

Thus, alignment of a single wheel in the WESAC system is critical to attitude control accuracy. It is sufficient to say that attitude accuracy is sensitive to misalignment with a factor of H_1/H_p . In this example, H_1/H_p is almost 18. For a fixed roll limit of $\pm 0.1^\circ$ and the values used here, one wheel misalignment is limited to 20 arc seconds.

In the general case, both wheels may have some misalignment which may not be detectable before launch. Thus, some sort of "vernier" gimbaling for fine alignment is a probable requirement. Of course, prelaunch alignment will eliminate major errors, but the orbital environment and duration may cause slight mass distribution and magnetic bearing profile changes.

Since pitching motion is decoupled from roll and yaw for small angles, wheel misalignment components can be considered in a similar fashion. From equation (6) it is apparent that small angular misalignments of the wheels are negligible with respect to pitch. The primary consideration for this axis is the variation of H_p with time, which can be detected and measured with the horizon sensor. Superimposition of a pitch control loop onto the power loop should be sufficient to control H_p .

Design and configuration aspects

The WESAC system with two counterrotating wheels of equal inertia and constant speed difference is considered to be the baseline configuration. It includes fixed gimbals with some in-orbit alignment capability. Of course, the net momentum is nominal along the vehicle pitch axis. Sensor requirements include a horizon sensor and possibly a high-resolution sun sensor for yaw sensing during N-S thrusting. Additional sensors may be required for periodic wheel alignment in orbit.

Since N-S thrusting introduces a requirement for additional sensing, it would be advantageous to use more momentum stiffness during these thrusting intervals if possible. This would eliminate direct yaw sensing requirements. One conceptual method of increasing the momentum stiffness involves releasing the gimbal-fixed condition on one wheel, thus allowing it to "float" at constant angular speed. The other wheel remains gimbal-fixed and therefore applies its stiffness to the attitude control function. This is equivalent to increasing the net momentum by an order of magnitude. Of course, after each N-S thrusting interval, the floating wheel must be "locked" into its previous orientation with a series of discrete gimbal increments over a 6-hour period, hence introducing only roll errors which are directly detectable and corrected with attitude thrusters.

Another possible configuration in which wheel energy storage is used includes both a pair of high-speed wheels and a DGMW system. The former would normally have zero net momentum and be used only as a battery replacement, while the latter would provide attitude control functions only. Certain advantages can be obtained from such a combination of devices. Orientation with respect to satellite axes of the paired wheels becomes a problem of optimization. Such orientation is arbitrary for a perfect pair of wheels which do not generate net momentum. However, perturbations about all three axes may be expected, at least during power extraction and addition cycles.

Alignment of paired wheels along the pitch axis is an obvious possibility and has certain advantages. Perturbations along the wheel axis, such as differential deceleration, produce no yaw errors and can be countered directly with the pitch loop of the DGMW. However, misalignment of these wheels can produce roll and yaw torques, which may or may not be countered by the DGMW system. The yaw component must first be detected or predicted to control yaw without direct sensing.

When wheel energy storage systems are considered for commercial applications, reliability becomes a critical factor and appropriate redundancy must be designed into the unit. For other systems containing momentum wheels, a spare wheel is usually assumed to satisfy part of this requirement. It appears that a third energy storage wheel may also fulfill the backup requirement for the configurations of interest here. This wheel would be idle until a paired wheel approached failure and would be capable of replacing either wheel. Of course, if a DGMW system were also on-board, it would require its own redundant wheel.

Conclusions

The basic objective at this early stage of wheel energy storage development has been the investigation of the compatibility of such systems with the attitude control functions of the spacecraft. Obvious violations of attitude-holding requirements and critical development problems have been sought. There appear to be no basic incompatibilities within the assumptions used here. In fact, the WESAC system may provide several advantages in terms of mass and overall simplification of subsystems. Critical problems regarding attitude control performance have been identified. Conclusions presented here are premised on the availability of material and bearing technology associated with construction of a WESAC system.

Critical problem areas associated with attitude control performance, which could be identified at this stage of development, are summarized in the following paragraphs.

Alignment of the net momentum vector appears to be most critical to attitude performance because of the individual high momentum values of each wheel. In orbit, periodic realignment of these wheels seems to be essential. This will require detection, measurement, and correction methods which may involve special sensors. Techniques for performing these operations should be developed. Of course, prelaunch alignment techniques must be perfected and accurate estimates of in-orbit misalignments will be helpful.

It is essential that load torques on each wheel are nominally equal during power extraction and addition processes to minimize long-term variations in net momentum. The pitch control loop on a WESAC system must be superimposed on the power control system so that satisfactory performance is maintained.

Selection of an optimum configuration for a wheel energy storage and attitude control system will depend on the state of technology, vehicle design and function, and mission requirements. Three possible modes of operation have been identified here. The basic WESAC system is conceptually simple and has a net momentum equivalent to that of a fixed-gimbal wheel for a satellite of the same size. If one wheel can be floating during N-S thrusting, direct yaw sensing will not be necessary. Finally, the zero net momentum configuration can be used with a DGMW system, allowing a large selection of orientations. This combination is advantageous because the DGMW can be used to counter misalignment and differential power balance torques.

In summary, a wheel energy storage system appears feasible with respect to attitude control functions if cited technologies become available.

Acknowledgment

The author would like to thank Messrs. C. J. Pentlicki, W. J. Billerbeck, and A. Ramos of COMSAT Laboratories for their invaluable help in this study.

Glossary

$\bar{e}_x, \bar{e}_y, \bar{e}_z$	Unit vectors along the vehicle x , y , and z axes, respectively
\bar{G}	Gravity-gradient torque
\bar{H}	Total angular momentum
H_N	Magnitude of bias nominal momentum
\bar{H}_p	Net momentum of a paired wheel system
$\bar{H}_B, \bar{H}_1, \bar{H}_2$	Momentum of the vehicle, wheel 1, and wheel 2, respectively
I	Axial moment of inertia of each paired wheel
I_x, I_y, I_z	Satellite principal moments of inertia
P	Power required by satellite subsystems
\bar{T}	Disturbance torque
γ_x, γ_y	Gimbal angles or angular misalignment components of momentum
η	Energy conversion efficiency
ϕ, θ, ψ	Roll, pitch, and yaw attitude angles, respectively

ω_0 Orbital rate = 7.28×10^{-5} rad/s

ω_{01}, ω_{02} Initial angular speeds of wheels 1 and 2, respectively

Ω Paired wheel speed difference

References

- [1] H. L. Mork, "Synthesis and Design of a Gimballed Reaction Wheel Attitude Stabilization Package (GRASP)," *AIAA Guidance, Control and Flight Mechanics Conference*, Hofstra University, Hempstead, New York, August 1971, AIAA Paper No. 71-950.
- [2] J. E. Keigler, W. J. Lindorfer, and L. Muhlfelder, "Stabilite Attitude Control for Synchronous Communications Satellites," *AIAA 4th Communications Satellite Systems Conference*, Washington, D.C., April 1972, AIAA Paper No. 72-572.
- [3] H. J. Dougherty, K. L. Lebsack, and J. J. Rodden, "Attitude Stabilization of Synchronous Communications Satellites Employing Narrow-Beam Antennas," *Journal of Spacecraft and Rockets*, Vol. 8, No. 8, August 1971, pp. 834-841.
- [4] M. G. Lyons, K. L. Lebsack, and E. D. Scott, "Double Gimballed Reaction Wheel Attitude Control System for High Altitude Communications Satellites," *AIAA Guidance, Control and Flight Mechanics Conference*, Hofstra University, Hempstead, New York, August 1971, AIAA Paper No. 71-949.
- [5] M. H. Kaplan, "Active Attitude and Orbit Control of Body-Oriented Geostationary Communications Satellites," *AIAA Progress Series in Astronautics and Aeronautics, Communications Satellite Technology*, P. L. Bargellini, Ed., Vol. 33, MIT Press, 1974, pp. 29-56.



Marshall H. Kaplan is Associate Professor of Aerospace Engineering at the Pennsylvania State University and a consultant to COMSAT Laboratories on satellite dynamics and control. His teaching and research interests include astrodynamics, spacecraft autopilots, propulsion, and planetary gravity analysis. Recently, he has published papers on the use of electric thrusters for complete satellite control, retrieval of spinning objects from orbit, and modeling of the lunar

gravity field. Dr. Kaplan received a B.S. in aeronautical engineering from Wayne State University, an S.M. in aeronautics and astronautics from M.I.T., and a Ph.D. in aeronautics and astronautics from Stanford University. He is an Associate Fellow of AIAA, a member of Sigma Xi, and a Founder Member of the American Academy of Mechanics.

Index: solar cells, Intelsat IV, radiation effects.

Effects of radiation on the violet solar cell

R.A. ARNDT

(Manuscript received November 26, 1973)

Abstract

The violet solar cell, which generates nearly 5 mW/cm² more power than solar cells employed in present commercial communications satellites, hereafter referred to as "satellite cells," has been irradiated with 1-MeV electrons to a fluence of 10^{16} cm⁻² and with 2- and 4-MeV protons to a fluence of 10^{13} cm⁻². An electron fluence of about 10^{16} cm⁻² or a proton fluence of 2×10^{10} cm⁻² is required to reduce the power output of the violet cell to that of the satellite cell at beginning of life. The violet cell produces more power after low neutron fluences than a fully recovered Li-doped cell and only a few percent less power after high neutron fluences.

Introduction

A new *n/p* solar cell with substantially higher efficiency than satellite cells was recently announced [1]. At the maximum power point, this cell, known as the violet cell, typically produces 74 mW under simulated AM0 conditions, while satellite cells produce about 56 mW (cell area = 4 cm²). This increased power is the result of improvement in four areas:

- a. the diode characteristic of the cell has been improved with an accompanying improvement in fill factor,

b. the collection efficiency in the wavelength region below $5,000 \text{ \AA}$ has been increased,

c. the open-circuit voltage has been increased primarily due to a reduction of the reverse saturation current,

d. a new antireflective coating [2] on the cell provides greater transmission at short wavelengths and better optical matching with the cover-slide.

The higher power output of the violet cell will be advantageous in future satellite power sources provided that it is maintained after exposure to space radiation. Violet cells have been irradiated by electrons and protons to fluences beyond those expected on a satellite in synchronous orbit for a period of 10 years. (Although communications satellites are not normally subjected to neutron bombardment, some potential users of the violet cell will be interested in their effects, particularly in relationship to Li-doped cells which are under development, because of their annealing characteristics after irradiation [3]. Neutron irradiations have therefore been included.) Current-voltage characteristics under AM0 simulated sunlight have then been determined.

Samples and Procedure

The violet cells used in the radiation tests were n/p cells constructed at COMSAT Laboratories from 2×2 -cm slices, 0.010 in. thick. Cells of the type used on satellites (2×2 cm, $10 \text{ } \Omega\text{-cm}$, n/p , 12-mil-thick pulled crystal) were included for comparison in the electron and proton irradiations. Those cells (except the Li-doped cells) that were irradiated with electrons and neutrons were covered with 6-mil, fused silica covers having a MgF_2 antireflective coating, while those cells that were irradiated with protons were uncovered. Two types of Li-doped, p/n cells were also irradiated with neutrons. One was made from crucible-grown silicon and the other from float-zone material with the lithium introduced by ion implantation. Both types of Li-doped cells were irradiated without covers.

Electron and proton irradiations were performed at the Naval Research Laboratory. The cells were mounted on an air-cooled substrate held at room temperature and each cell received the full range of particle fluence. Electron irradiations to fluences of 10^{14} – 10^{16} cm^{-2} were performed in air with 1-MeV electrons having a nominal flux of $3 \times 10^{12} \text{ cm}^{-2} \text{ s}^{-1}$. Proton irradiations were performed in vacuum with fluxes of the order of 10^8 – $10^9 \text{ cm}^{-2} \text{ s}^{-1}$; fluences varied from 10^{10} – 10^{13} cm^{-2} . Neutron irradiations of

violet cells similar to those used for the electron irradiations were included in the test program of the Air Force Aero Propulsion Laboratory (AFAPL) at the White Sands Missile Range Fast Burst Reactor for comparison with $20\text{-}\Omega\text{-cm}$, Li-doped, p/n cells. Neutron fluences (1-MeV equivalent) varied from $1.7 \times 10^{11} \text{ cm}^{-2}$ to $2.5 \times 10^{13} \text{ cm}^{-2}$. At all times, except during measurement and annealing cycles, the neutron-irradiated cells were kept at dry-ice temperature.

Current-voltage measurements of the electron- and proton-irradiated cells were conducted at COMSAT Laboratories, whereas the neutron-irradiated cells were measured at Wright-Patterson Air Force Base. The solar simulator at COMSAT Laboratories is a Spectrolab X-25L which is periodically monitored for spectral distribution; filters are added when necessary to keep the distribution as close to AM0 [4] as possible. The total intensity of the simulator is set with a secondary standard cell which was calibrated with a balloon flight cell. In some cases filters were placed in front of the measured cells to obtain quick relative measurements in the red and blue portions of the spectrum. The two filters used were Corning CS4-97 and CS2-58, the former transmitting below and the latter transmitting above a wavelength of $6,500 \text{ \AA}$. All measurements were made at room temperature.

Results

Electrons

Figure 1 shows the maximum output power as a function of electron fluence for solar cells illuminated with simulated AM0 light after irradiation with 1-MeV electrons. The experimental points are averages of at least two closely matched cells. Two features of the curves are noteworthy: the violet cell shows greater output power than the satellite cell at all fluences studied, and the power output of the violet cell drops somewhat more rapidly* with fluence than that of the satellite cell. This latter feature is a result of using p -type silicon with moderately low

* Previous data on electron-irradiated cells [1] showed that the power curves of the violet cell and a satellite cell remained parallel as the fluence increased. Comparison with unpublished data showed that one violet cell datum point in Figure 12 of Reference 2 was misplaced. When this point is corrected, as reported here, the power vs fluence curve does drop somewhat more rapidly for the violet cell than for the satellite cell.

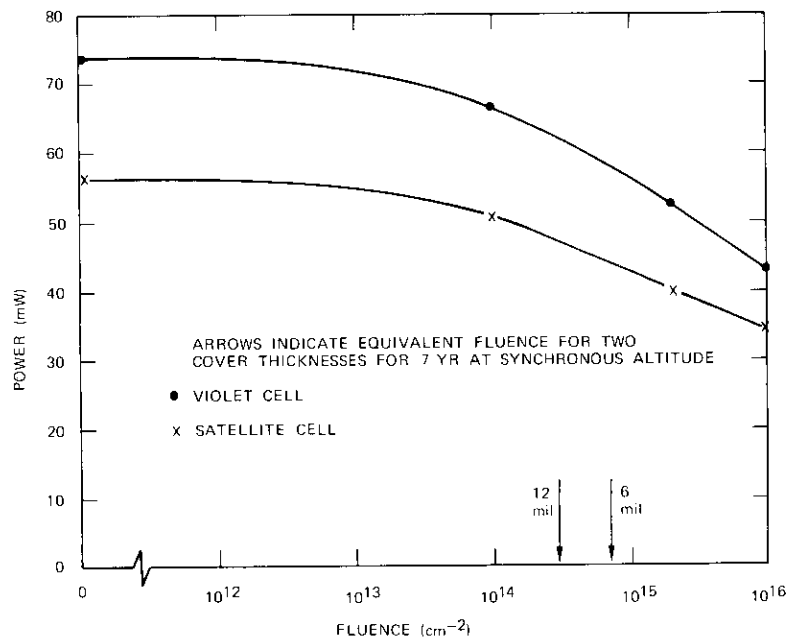


Figure 1. Maximum Power of a Violet Cell and a Satellite Cell vs 1-MeV Electron Fluence under AMO Illumination

resistivity as the starting material of the violet cells.* There are only minor changes in fill factor for either type of cell up to the highest fluence used. For comparison, the 1-MeV equivalent electron fluences after seven years at synchronous altitude are also shown in Figure 1 for a satellite cell with 6- and 12-mil covers. The violet cell is clearly preferable to the satellite cell for use on satellites.

Protons

For the solar cells studied the maximum power after 2- and 4-MeV proton irradiation is shown in Figure 2. One cell was used for fluences of

* For the violet cell, the rate of power loss at the higher fluences was about 3.3 mW/cm²/decade, whereas for the satellite cell the loss was about 2.2 mW/cm²/decade. Satellite cells made from float-zone material show about 2.0 mW/cm²/decade. Measurements on irradiated conventional cells with 2-Ω-cm resistivity showed a power loss of 3.5 mW/cm²/decade [5].

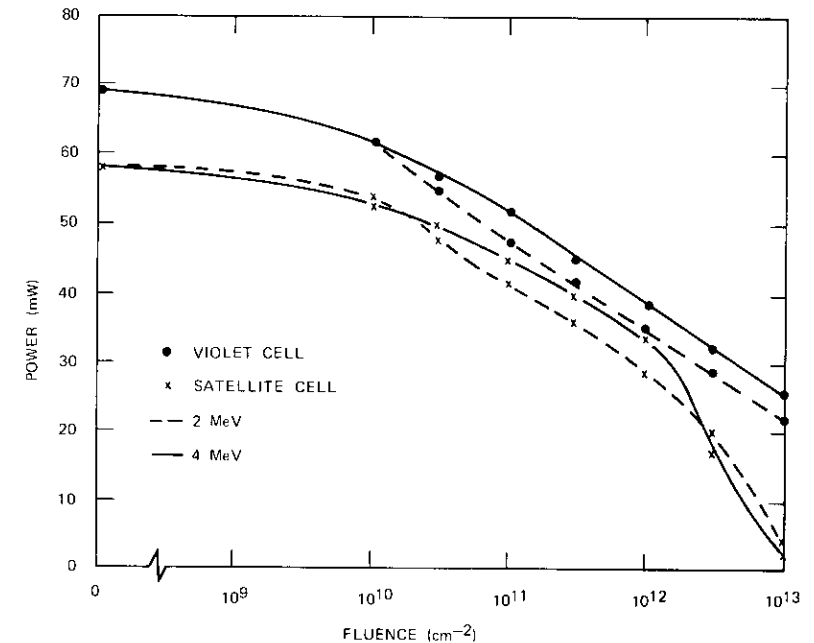


Figure 2. Maximum Power under AMO Illumination of a Violet Cell and a Satellite Cell vs 2- and 4-MeV Proton Irradiation

even powers of 10 and a second cell was used for the other fluences; however, both cells received the maximum fluence of 10¹³ cm⁻². These cells, which were closely matched, were irradiated and measured without covers. It can be seen by comparison with Figure 1 that the power output of the violet cell before irradiation is greater with a cover than without a cover. This is due to the improved optical match that results from using the new antireflective coating on the cells. A noteworthy feature of Figure 2 is the precipitate drop in output power of the satellite cells as the fluence approaches 10¹³ cm⁻². The scatter in the data (including the electron data) was generally too small to be shown, i.e., at most, of the order of 1 mW.

Figures 3a and 3b are graphs of short-circuit current as a function of proton fluence for the blue and red portions of the spectrum, respectively. These two figures show that, while the degradation of the red response of an irradiated violet cell with proton fluence is similar to that of a satellite cell, the blue response of the violet cell changes very little up to a proton fluence of 10¹³ cm⁻². The improvement of the short wavelength response

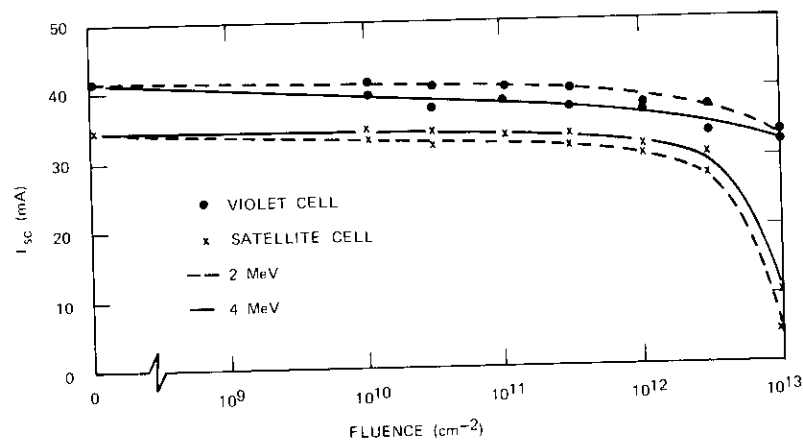


Figure 3a. Short-Circuit Current vs 2- and 4-MeV Proton Fluence (illuminating wavelengths less than 6,500 Å)

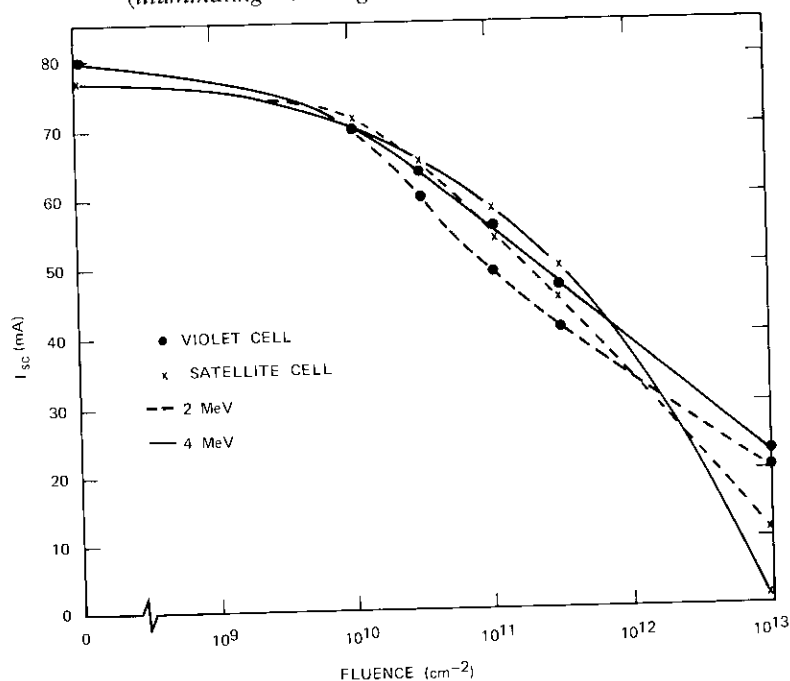


Figure 3b. Short-Circuit Current vs 2- and 4-MeV Proton Fluence (illuminating wavelengths greater than 6,500 Å)

achieved in the violet cell is thus seen to be radiation resistant.

Figure 4 shows current-voltage curves after a 4-MeV proton fluence of 10^{13} cm^{-2} . The maximum power output is 1.6 mW with a fill factor of 0.32 for the satellite cell, and 25 mW with a fill factor of 0.73 for the violet cell. Before irradiation the fill factors were 0.77 and 0.74 for the violet cell and the satellite cell, respectively. This indicates that the improved diode characteristic of the violet cell is also radiation resistant.

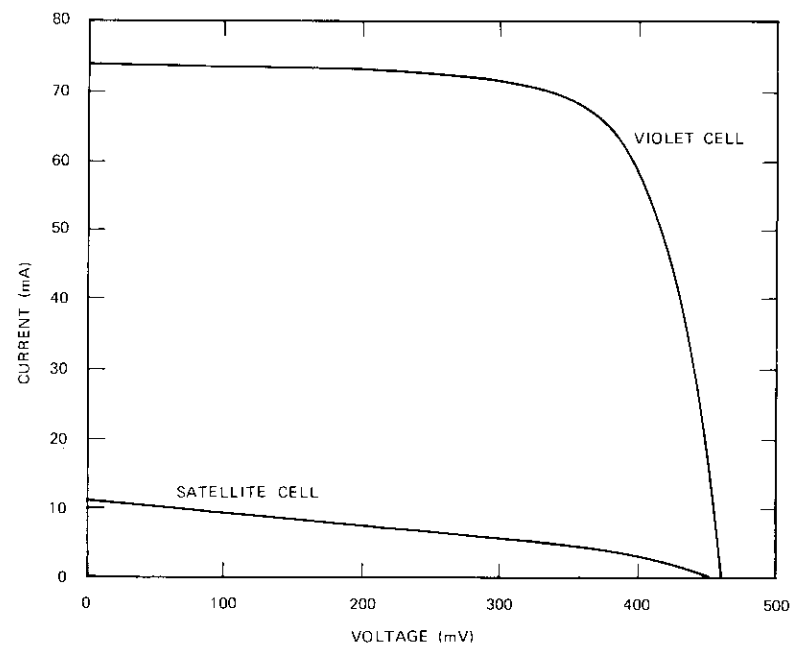


Figure 4. Current-Voltage Curves, under AM0 Illumination, After 4-MeV Proton Irradiation to a Fluence of 10^{13} cm^{-2}

Neutrons

Figure 5 shows the maximum output power, measured before any annealing, as a function of neutron fluence for a violet cell, a float-zone Li-doped cell, and a crucible-grown Li-doped cell. The power output of all cells shows some improvement after annealing for 14 days at room temperature, but the output of the violet cell remains greater than that of either of the Li-doped cells.

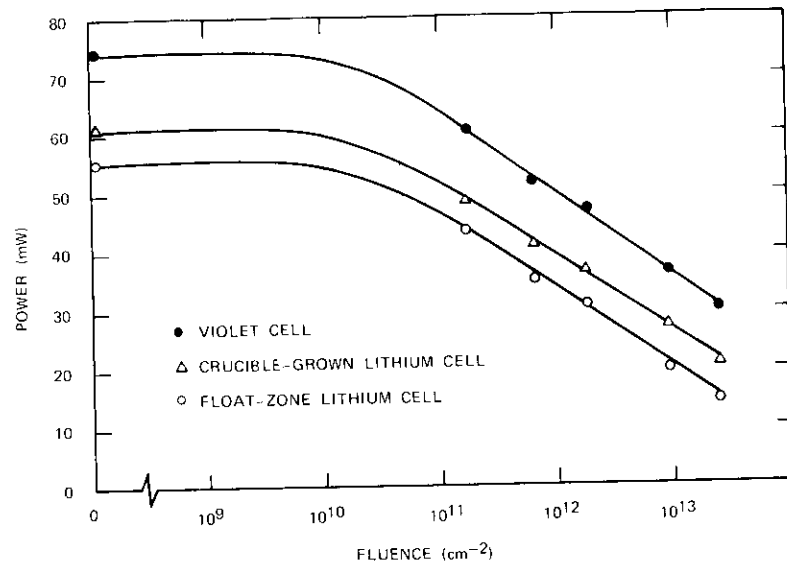


Figure 5. Maximum Power, Immediately After Irradiation, vs 1-MeV Equivalent Neutron Fluence

Figure 6 compares the maximum power of the violet cell after annealing for 14 days at room temperature with that of the float-zone Li-doped cell after annealing at both room temperature (for 14 days) and 80°C. Although the crucible-grown Li-doped cells were generally more stable than the float-zone cells, the latter are shown because they recover more of their radiation-induced power loss and they recover more rapidly. Figure 7 shows the recovery of power for the Li-doped cells and the violet cell, all irradiated to $2.47 \times 10^{13} \text{ cm}^{-2}$ and annealed at 80°C. Although the float-zone cell recovers faster, it can be seen that approximately 10 hours of annealing at 80°C are required before the output of the Li-doped cell is greater than that of the violet cell.

It should be pointed out that, although all cells were measured by AFAPL, the violet cell measurements reported here were performed at COMSAT Laboratories. A comparison of the solar simulators at COMSAT and AFAPL indicated that the COMSAT simulator had a higher blue content. This difference would tend to make COMSAT's violet cell current measurements several percent higher than AFAPL's measurements because of the increased blue response of the violet cell compared to that of the Li-doped cells.

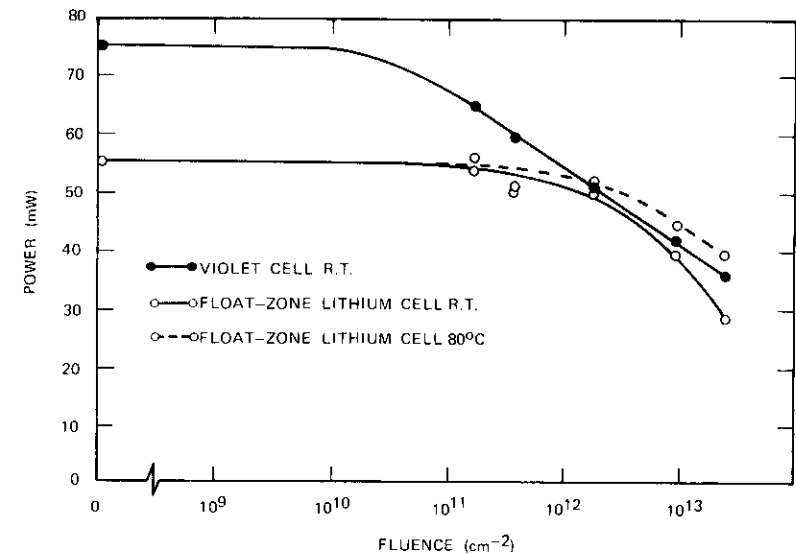


Figure 6. Maximum Power vs 1-MeV Equivalent Neutron Fluence

Discussion

There are two unexpected results in the proton data. The first of these is seen in Figure 2, where the curves for the satellite cells irradiated by 2- and 4-MeV protons cross at a fluence of about $2 \times 10^{12} \text{ cm}^{-2}$. The short-circuit current curves for wavelengths greater than 6,500 Å also cross in Figure 3b. It would be expected, from the ranges and damage constants of 2- and 4-MeV protons, that these curves would converge at some fluence, e.g., $\sim 10^{12} \text{ cm}^{-2}$, and remain together at all higher fluences. However, in the case of 2-MeV protons there is a higher concentration of photo-induced carriers in the heavily damaged region occurring at the end of the proton range than in the case of 4-MeV protons. This would tend to fill the traps at the end of the range more in the 2-MeV case than in the 4-MeV case and might result in the observed crossover.

The other unexpected result, seen in Figure 3a, is that the short-circuit current produced by the blue end of the spectrum in violet cells irradiated with 2-MeV protons is greater than in those irradiated with 4-MeV protons. It is possible that a similar factor is responsible for this effect.

The fill factor of electron-irradiated cells, both violet cells and satellite cells, does not change much with fluence; the fill factor of violet cells

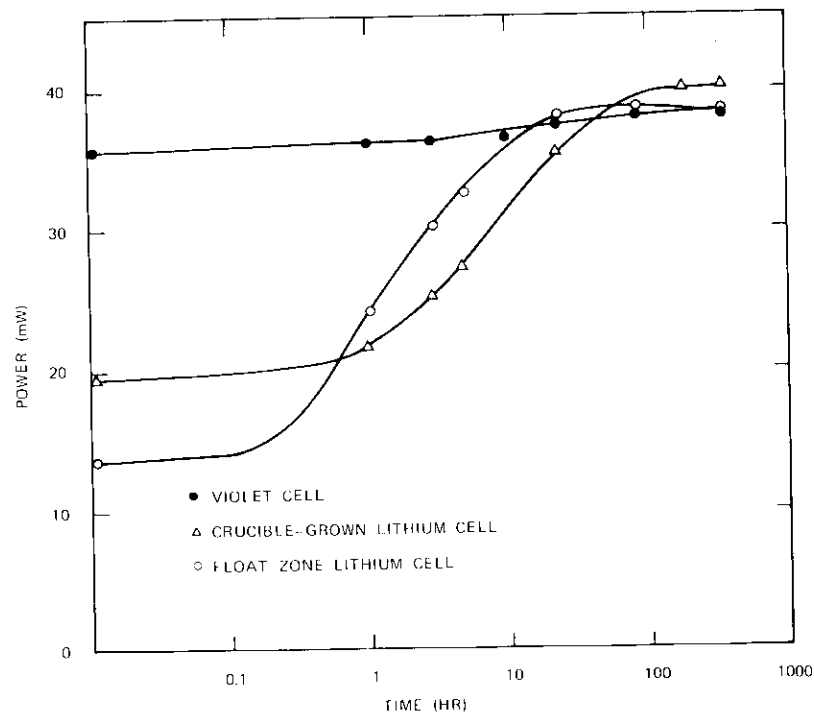


Figure 7. Maximum Power vs Time of Anneal at 80°C

drops by about 2.5 percent after an electron fluence of 10^{16} cm^{-2} and that of satellite cells drops by about 4 percent. This slight change is typical of conventional cells [6]. However, after irradiation with a 4-MeV proton fluence of 10^{13} cm^{-2} , the fill factor of the satellite cells decreased by more than 50 percent while that of the violet cells decreased only by about 4 percent.

After irradiation with the highest fluences used, Li-doped cells exhibited greater output power after recovery than the violet cell. At the lower fluences, however, the violet cell had greater power output than fully recovered Li-doped cells.

Conclusions

It has been shown that the violet cell can receive an electron fluence of about 10^{15} cm^{-2} or a proton fluence of $2 \times 10^{10} \text{ cm}^{-2}$ before its output

power is reduced to that of a satellite cell at beginning of life. One reason for this superiority is the violet cell's increased response to the short wavelength part of the solar spectrum which is not degraded by particle irradiation. A second reason is the improvement in the diode characteristic of the cell, which is also radiation resistant. The resistance of the violet cell to high proton fluences will make it particularly useful on satellites in the event of solar flares which give rise to a large flux of protons whose energy is greater than that found in the trapped proton environment. The advantage of using a violet cell in a neutron environment is that, immediately after irradiation, its power is greater than that of the lithium cell. Hence, it is unnecessary to anneal the cells while mounted on a satellite.

Acknowledgment

Special thanks are extended to the Air Force Aero Propulsion Laboratory for performing the neutron irradiations and subsequent measurements and providing the results on other cells prior to publication. The guidance of Drs. E. S. Rittner and J. Lindmayer and discussions with Dr. A. Meulenberg were also helpful. The violet cells were produced by the Semiconductor Technology Department under J. F. Allison.

References

- [1] J. Lindmayer and J. Allison, "An Improved Silicon Solar Cell—The Violet Cell," *Conference Record of the Ninth IEEE Photovoltaic Specialists Conference*, 1972, p. 83; J. Lindmayer and J. F. Allison, "The Violet Cell: An Improved Silicon Solar Cell," *COMSAT Technical Review*, Vol. 3, No. 1, Spring 1973, pp. 1-23.
- [2] A. G. Revesz, "Vitreous Oxide Antireflection Films in High-Efficiency Solar Cells," *COMSAT Technical Review*, Vol. 3, No. 2, Fall 1973, pp. 449-452.
- [3] *Proceedings of the Fourth Annual Conference on Effects of Lithium Doping on Silicon Solar Cells*, edited by P. A. Berman, April 29, 1971.
- [4] F. S. Johnson, "The Solar Constant," *Journal of Meteorology*, Vol. 11, No. 6, December 1954, pp. 431-439.
- [5] A. Meulenberg and D. Curtin, private communication.
- [6] J. R. Carter and H. Y. Tada, "Solar Cell Radiation Handbook," TRW Systems Group, Report 21945-6001-RU-00, January 28, 1973.



Dr. Richard A. Arndt received his Ph.D. from Northwestern University in 1961. From 1961-1969 he was a staff scientist at the Brookhaven National Laboratory. Since he joined COMSAT Laboratories in 1969, he has been a member of the technical staff of the Physics Laboratory.

Index: solar cells, Invar, thermal stresses, electric connectors.

Development of advanced interconnectors for solar cells

D. J. CURTIN AND W. J. BILLERBECK

(Manuscript received October 23, 1973)

Abstract

This paper examines the electrical interconnection of solar cells into lightweight, deployed solar arrays and the results of a thermal stress analysis of these interconnects. New data on the stresses and fatigue life of welded silver bonds, obtained from a 3-dimensional, finite element computer program, are presented for interconnectors cycled down to -196°C . It is shown by the development of a module that passed a 1,000-cycle test that the use of silver-plated Invar can result in an order of magnitude improvement in fatigue life compared with that of the materials used previously. The results of the first extended thermal cycle tests of solar cell modules fabricated from silver-plated Invar are also described.

Introduction

A number of engineering projects have been directed toward the development of lightweight solar arrays. The impetus for this work is the cost of placing a power system in orbit, as well as the additional benefits (or revenue) which can be gained from a heavier payload in the spacecraft. Presently available solar arrays have been surveyed [1]-[4]. The

This paper is based upon work performed in COMSAT Laboratories under the sponsorship of the International Telecommunications Satellite Organization (INTELSAT). Views expressed in this paper are not necessarily those of INTELSAT.

array output power after 5 years in synchronous orbit vs weight for various types of solar arrays is shown in Figure 1. To provide a fair comparison, the weights of solar cells, covers, substrate, and any stowage, deployment, or orientation equipment associated with the array are included. Oriented, flexible substrate arrays provide significantly higher power output per weight than other types of solar arrays for power levels over 1 kW.

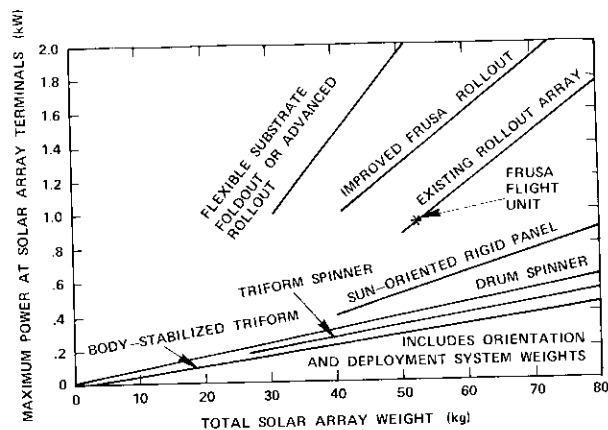


Figure 1. Solar Array Power at End of 5-Year Mission (at summer solstice) vs Weight

Flexible substrate solar arrays are usually made of Kapton sheet or reinforced Kapton sheet. Various deployable structures are used to apply tension. One design uses a pantograph deployment mechanism with a pallet at the outboard end [5], while another employs a single SPAR boom having a tubular spar member. Both rollout and "accordion pleat" foldout designs are under development.

The application of these deployable solar arrays to long-life synchronous orbit missions results in several new problem areas. One of these is the stress induced in the solar cells at low temperatures. A transient thermal analysis, shown in Figure 2, indicates that the total temperature range experienced by a sun-oriented, flexible substrate array at synchronous orbit is more than twice that of a drum spinner solar array. This is mainly due to the low thermal capacity of the thin substrate. Furthermore, the maximum rate of temperature change (i.e., thermal shock) of the flexible array is increased more than six times.

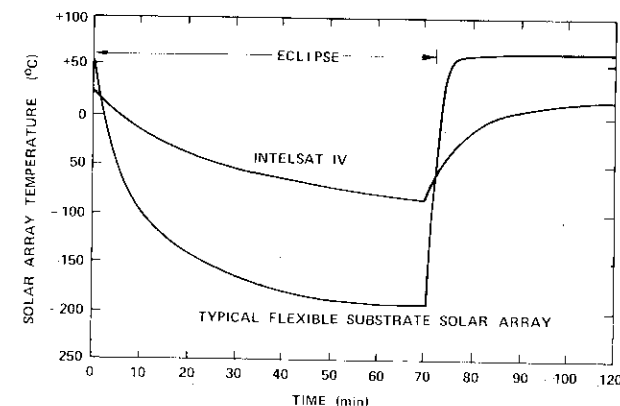


Figure 2. Solar Array Temperature Profiles (longest eclipse) at Synchronous Orbit

Flexible solar arrays used on long-life missions in geostationary orbit must operate successfully through about 450 to 900 temperature cycles from +60°C to -196°C. The investigations reported in this paper clearly demonstrate that this requirement can be met with solar cell interconnectors fabricated from silver-plated Invar.

Limits of solder joining

Traditionally, pure silver or solder- or silver-plated materials have been used for electrical interconnections between solar cells. A variety of mechanical configurations have been used. In almost all cases the cells have been joined by soldering.

Few comprehensive correlations of cyclic life data on solar cell solder bonds have been performed. Luft and Maiden [6] studied the incidence of fatigue cracking of solder on 75- μ m copper interconnects vs number of cycles at various temperatures. The number of cracks increases an order of magnitude when the minimum temperature is decreased from -80°C to -175°C; about 90 percent of the joints are cracked after several hundred cycles. The number of cracked joints decreases an order of magnitude when the interconnect is changed from copper to Kovar, and two orders of magnitude when it is changed to molybdenum.

Ralph and Roger [7] identified four potential mechanisms for interconnection failure:

- a. silicon stressed beyond its ultimate strength,
- b. interconnect stressed beyond its ultimate strength,
- c. interconnect fatigue failure,
- d. solder joint fatigue failure.

These mechanisms are principally related to differential thermal expansion effects. Ralph and Roger also developed a 2-dimensional analysis of stresses b and c for a simple loop configuration. With suitable materials and geometry, it was concluded that a system designed to avoid the first three failure mechanisms should be possible. Another interesting conclusion of this paper was that the conventional 36Pb/62Sn/2Ag solder is heavily stressed during thermal cycling to -150°C , and appears to be subject to solder-fatigue failure.

A more detailed analytical technique with a finite element digital computer program [8] has been used to account for stress concentrations at the edge of the bond. This JPL study presents new and important data on the thermophysical properties of the materials, particularly at low temperatures.

Independent calculations show that, with the best conventional 25- to 50- μm -thick interconnector materials, the solder is in yield at temperatures above 90°C and below about -60°C to -120°C . If a solar array experiences cyclic operating conditions outside this temperature range, the solder bonds should be subject to low-cycle fatigue.

An analytical procedure is needed to estimate the fatigue life of soldered interconnector bonds. Once a detailed 3-dimensional stress analysis including plastic flow has been used to calculate the effective total strain range, the expected cyclic life of the bonds can be obtained from the low cycle plastic strain analysis methods of Manson [9], [10]. Initial work utilizing these techniques has been described by Rauschenbach and Gaylard [11]. A preliminary estimate of the fatigue life vs effective strain range of 36 Pb/62Sn/2Ag has been derived at COMSAT Labs by using Manson's universal slope method (see Figure 3) and further work is underway to refine this estimate. The reduced ductility of solder at cryogenic temperature is expected to significantly shorten its fatigue life.

The lack of specific experimental fatigue data on the solder material limits the accuracy with which the cyclic life of soldered array bonds can be calculated. Such data are urgently needed to eliminate order of magnitude errors in the estimates.

The analysis described in the preceding paragraphs predicts the number of cycles at which microcracks first appear in the highly stressed area of the solder fillet. Complete failure of the solder joint will occur later. Data

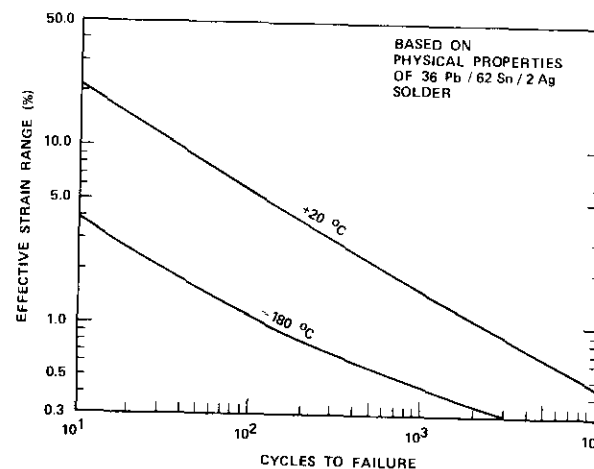


Figure 3. *Fatigue Life of Solder Predicted by Method of Universal Slopes*

obtained by Garner and Rauschenbach [12] show the probability of microcracks and open circuits. Boretz and Boring [13] state that, for 25- μm Kovar interconnects, when 2 percent of the joints are cracked, approximately 0.1 percent are failed on open circuit. A generalized relationship between the number of cycles at initiation of microcracks and the number of cycles to complete solder bond failure is needed.

Stress analysis of welded interconnects

Because lightweight flexible arrays at synchronous altitude will experience severe thermal cycling, an alternate interconnection technique may be required. This process should eliminate thermal stress and fatigue problems, permit automatic fabrication, reduce costs, increase reliability, and be independent of operator variation.

Thorough analysis of the stresses involved in solar cells, interconnectors, adhesives, and substrate materials is critical. This analysis requires a knowledge of the material properties, particularly mechanical properties, of cells, interconnectors, adhesives, and substrates from -196°C to $+100^{\circ}\text{C}$.

Alternate solar cell interconnecting schemes have been studied. Clarke [14] studied thermal compressing bonding. Good results were obtained; the main drawback was the long time needed to make each bond. Fischer,

et al. [15] studied parallel gap resistance welding, thermal compression bonding, and ultrasonic bonding. The best results were obtained using resistance welding. These studies were intended to derive processes for use with solderless solar cells.

On the basis of these studies and continuing efforts [16]-[18], it was decided at COMSAT Laboratories to study parallel gap resistance welding as the primary alternative to soldering. Since more work had been undertaken on this approach, it could progress faster through cooperative efforts with other investigators. The other two techniques may be good candidates [19], but resistance welding is still the prime candidate. At least four satellites will use resistance welded solar arrays: HELIOS, the ESRO GEOS, the Communications Technology Satellite (CTS), and the International Ultraviolet Explorer (IUE).

The intent of this program was to determine the feasibility of parallel gap welding for synchronous orbit missions and to analyze the stresses in solar cells, interconnectors, adhesives, and substrate materials. A literature search was performed to determine material properties over the temperature range. Available data and previous analytical work [20] were used to perform a simplified calculation of the expected thermal stresses in various materials. A thorough experimental study of the feasibility of resistance welding for synchronous missions was completed. Finally, the solar cell modules were fabricated and thermal shock tested from -190°C to $+65^{\circ}\text{C}$ for 100 cycles [21].

A parallel effort examined the overall processes required before advanced solar cell modules could be used. This effort included an examination of interconnector material annealing and plating, material properties, solar cell contact plating, solar cell and interconnector cleaning, storage before and after welding, welding parameter characterization, thermal shock testing, and thermal cycle testing.

The feasibility of parallel gap resistance welding for various types of solar arrays was demonstrated. The next step needed was a detailed, 3-dimensional analysis of the stresses in a welded interconnect system including fatigue analysis. The stress analysis [22] was performed with a 3-dimensional computer program [23]. Luft and Kaplan used the finite element direct stiffness method which is the predominant numerical method for 2- and 3-dimensional structural analysis. A program which included both the elastic and plastic regions of the stress-strain curves was used, since plastic flow usually occurs in the silver layer on the solar cells and on the interconnector. Both a microscale analysis of the 3-dimensional stresses in the weld joint between the interconnector and the

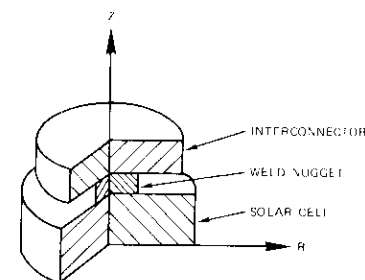


Figure 4. *Disk Model Used in the Computer Analysis*

cell and in the silicon immediately below the weld, and a separate analysis of the effects of external interconnector forces and moments on the weld, were performed.

The structure is divided into a large number of individual elements. The deformation and stresses are expressed in terms of the displacements. The equivalent forces acting at the nodes are obtained in terms of the nodal deflections. These forces are then equated to the externally applied forces at each of the external nodes to yield a set of simultaneous equilibrium equations.

A mathematical model was used to determine the stresses and strains caused by the differential thermal contraction on the weld joint itself. This model assumed that the weld joint was approximately circular so that the stresses were symmetrical about its centerline, as shown in Figure 4. This 3-dimensional disk model included the stresses acting in all three directions: the radial and tangential directions parallel to the weld surface, and the axial direction normal to the weld surface. For areas in which the stress changes rapidly, such as at the edge of a weld, small elements were used, while for the areas in which it varies slowly, larger elements were satisfactory (see Figure 5).

For lightweight, deployed solar arrays with flexible substrates in synchronous orbit, the worst stress occurs at the lowest temperature, -196°C . The two dominant material properties are the coefficient of thermal expansion, and the absolute value of Young's modulus. These properties were averaged over the temperature range of interest. Table 1 lists the data.

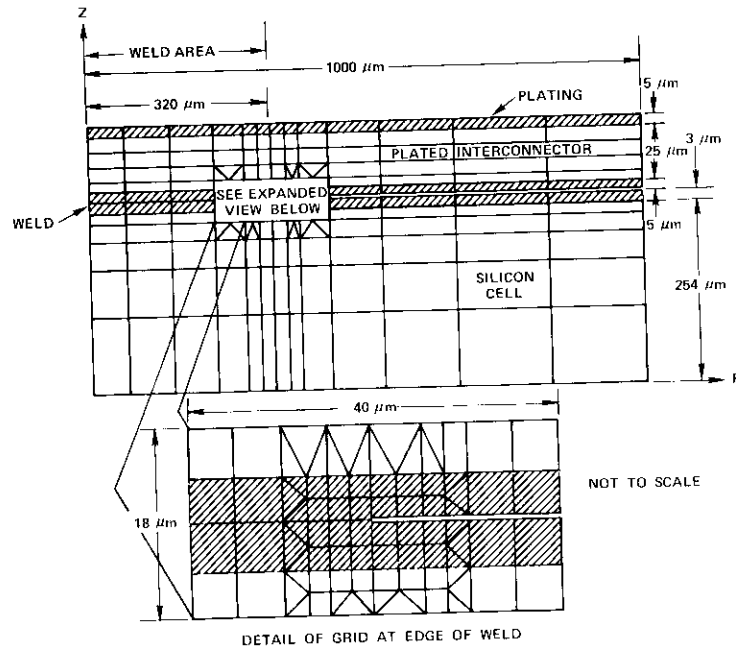


Figure 5. Finite Element Representation of Welded Joint Disk Model

TABLE I. MATERIAL PROPERTIES USED IN WELD ANALYSES

Material	Young's Modulus, E (GN/m ²)	Poisson's Ratio, ν	Mean Thermal Expansion Coefficient, α (10 ⁻⁶ /°C)	Yield Strength, σ_y (MN/m ²)	Ratio of Post-yield Modulus to Initial Young's Modulus
Silicon	84 ^a	0.20	0.90	100 ^b	—
Silver	89	0.37	17.0	86	0.01
Kovar	138	0.33	6.6	410	—
Molybdenum	340	0.32	4.1	1,000	—
Invar 36	136	0.29	1.69	950	—

^a A 2-to-1 range is seen in the value of Young's modulus for silicon. The largest value is used since it is expected to cause the highest stress.

^b Minimum ultimate strength.

In the literature search, potential new materials which had appropriate α and E values were examined. As shown in Table 1, one interesting material was Invar 36, i.e., ³⁶Ni/⁶³Fe, whose behavior approximates that of silicon better than that of any other material examined.

The finite element direct stiffness method and the material properties were used to analyze the thermal stresses and strains. The silver interconnector was assumed to be 35 μ m thick, while the molybdenum, Kovar, and Invar interconnectors were all 25 μ m thick with 5 μ m of silver plating on each face. As an example, Figures 6 and 7 show the radial stresses at the lower surface of the weld at -196°C for the all-silver and Invar interconnectors (note that the scales on these two figures are different). The steps in the stress distribution are caused by the finite size of the elements used. The edge of the weld is at 0.32 cm. The curves for molybdenum and Kovar fall between the silver and Invar curves.

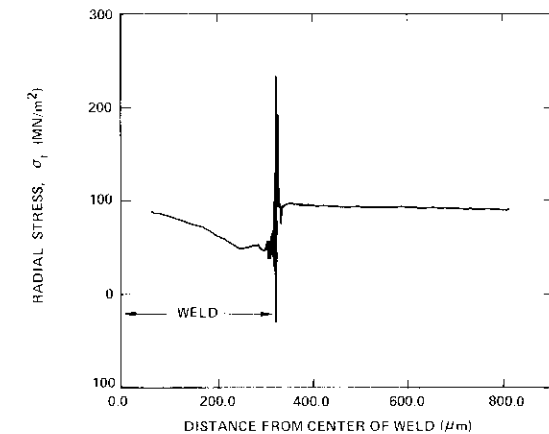


Figure 6. Radial Stress at Lower Surface of Weld for All-Silver Interconnector at -196°C

Table 2 shows the results of the weld joint analysis summarized from the computer plots. The first part of the table lists the maximum stresses in the silicon and the interconnector base material. A comparison of Tables 1 and 2 shows that the minimum ultimate strength of the silicon is exceeded by both pure silver and silver-plated Kovar interconnects. This is a significant result since it indicates the possibility of divoting-type failure within the silicon cell for these materials at low temperatures.

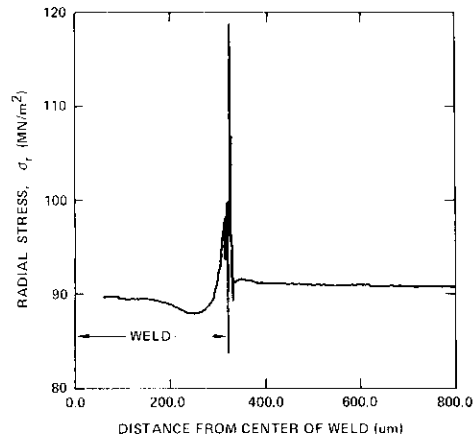


Figure 7. Radial Stress at Lower Surface of Weld for Invar Interconnector at -196°C

TABLE 2. COMPARISON OF MAXIMUM CRITICAL STRESS AND STRAIN VALUES USING WELDED INTERCONNECTORS FOR CYCLING FROM 20°C TO -196°C

Parameter	Interconnector Base Material			
	Silver	Kovar	Molybdenum	Invar
a. Maximum Stresses in Silicon and Interconnector Base Material				
Silicon Stress (MN/m^2)	181	130	87.6	29.1
Base Metal Stress (MN/m^2)	277.0	107	86.9	50.2
b. Maximum Values in the Silver Weld Joint				
Radial Stress, σ_r (MN/m^2)	234.0	177.7	153.4	119.0
Normal Stress, σ_z (MN/m^2)	146.2	97.5	66.4	25.2
Shear Stress, σ_{rz} (MN/m^2)	80.0	60.0	48.7	19.7
Effective Stress, $\bar{\sigma}$ (MN/m^2)	152.0	114.0	100.2	92.8
Radial Plastic Strain, ϵ_{pr} (%)	3.24	1.49	0.95	0.45
Normal Plastic Strain, ϵ_{pz} (%)	3.51	1.76	1.21	0.735
Plastic Shear Strain, ϵ_{prz} (%)	9.81	3.65	1.75	0.39
Effective Plastic Strain, $\bar{\epsilon}_p$ (%)	11.87	4.58	2.39	0.85
Effective Total Strain, $\bar{\epsilon}_t$ (%)	12.20	4.82	2.58	0.98

As seen in the second part of the table, when the α value approaches that of the silicon and the E value decreases, the stresses in the silicon and

the silver decrease. For Invar, all of the stresses are small, although the silver plating is still in yield at -196°C . An assessment of the fatigue in the silver indicates that the silver-plated Invar interconnector has the smallest effective total strain.

The goal of this analysis is the design of an interconnect that will not be overstressed and that has a fatigue life well beyond the length of the mission. Manson [9], [10] has done theoretical and experimental work on the fatigue life of metallic materials in the low cycle range. In this regime, the important parameter is the strain range rather than the stress in the material.

The dotted curve in Figure 8 shows the effective strain range vs cycles to failure from some experiments [10] on silver with high fineness (i.e., 99.995 percent). The effective strain values calculated for the pure silver interconnector and the silver material at the bond joint for the other silver-plated interconnectors are also plotted. As the coefficient of expansion approaches that of silicon and the Young's modulus decreases, the effective strain range in the silver decreases and the fatigue life increases. Consequently, going from pure silver to a silver-plated Invar material significantly increases the predicted fatigue life.

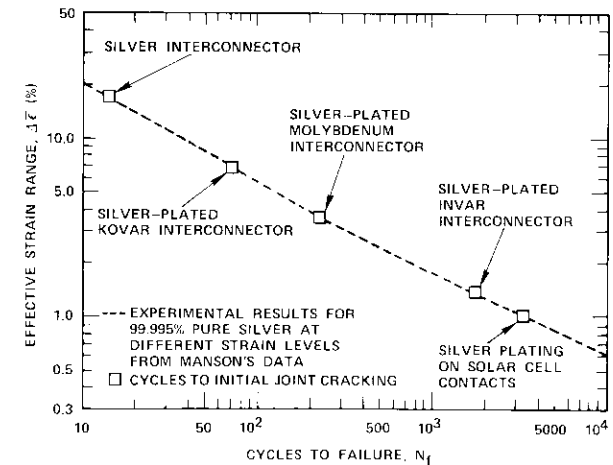


Figure 8. Computed Fatigue Life of Welded Silver Bonds Cycled Over Temperature Range of 100°C to -196°C

These analytical results are conservative since a silver interconnector has been observed to survive more than 14 cycles. An important factor

is that the computed fatigue life does not necessarily indicate when the joint will fail, but only when the weld "crack" begins to grow. When this occurs, the peak stress at the rim of the bond remains the same, but the highly stressed regions push into lower stress areas. Total failure will occur well after the initial cracking. This differs markedly from the usual mechanically loaded low cycle fatigue test. In such materials, once there is a local fatigue failure, the ensuing crack results in a very large increase in the local stress concentration. Soon total failure occurs. Therefore, the significant factor in Figure 8 is not the exact fatigue life, but the relative improvement in fatigue life.

Early application of silver-plated Invar interconnectors

As a result of the analysis described earlier, silver-plated Invar was tested. After initial screening tests, modules were built for extended thermal shock testing.

Table 3 compares two solar cell modules which were tested. Both modules had the same weld schedule and silver-plated Invar interconnector configuration (Figure 9). To minimize external stress on the weld bond, the configuration shown in Figure 9 had good in-plane stress relief and also avoided torsional stresses. The solar cell modules were held in tension by a rigid frame.

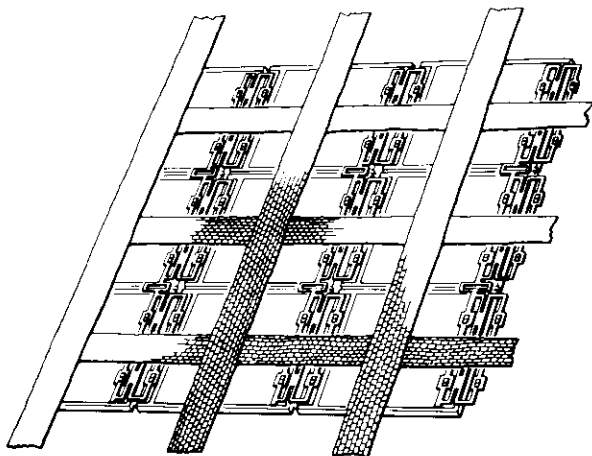


Figure 9. Detail of the Torsion-free Interconnector

TABLE 3. COMPARISON OF COMSAT AND TRW MODULES

Item	COMSAT	TRW
Solar Cells	Unglassed conventional contacts, 250 μm thick with 5 μm of silver	Glassed, wraparound contacts, 205 μm thick
Interconnector	25- μm Invar plated with 10 μm of silver etched to TRW pattern	25- μm Invar plated with 5 μm of silver etched to TRW pattern
Electrode Size	625 \times 625 μm	375 \times 625 μm
Electrode Pressure	1.33 N (3 lb)	1.33 N (3 lb)
Weld Schedule	N: 0.61 V, 200 ms P: 0.66 V, 200 ms	N: 0.61 V, 200 ms P: 0.66 V, 200 ms
Substrate	75- μm Kapton cut to windowpane arrangement	Fiberglass-reinforced Kapton strips (25- μm Kapton, 65- μm fiberglass cloth) in windowpane arrangement
Cell to Substrate Adhesive	RTV 118	RTV 118
Mounting Frame	Fiber epoxy board held by 8 screws	Fiberglass held together by double-sided tape and 16 screws

Both modules were simultaneously thermal shock tested for comparison. The test was conducted for 1,000 cycles from -196°C to $+55^{\circ}\text{C}$ in a nitrogen atmosphere with a 10-minute dwell at each temperature. The low temperature was achieved by dipping the modules in liquid nitrogen and the high temperature by placing the modules close to a quartz iodide lamp. Physical inspection and electrical measurements were made frequently.

No electrical degradation in either module was observed. Each module had one weld failure on the P contact, and the COMSAT module had one interconnector break on the same cell that had the P contact weld failure. The occurrence of both weld failures on the P side may indicate that further P contact weld schedule development is needed. The interconnector break was not associated with a weld failure and was probably caused by some external force, perhaps a twisting of the interconnector during fabrication.

The absence of electrical degradation demonstrates that silver-plated

Invar can be successfully welded to silicon solar cells. Since the same results were achieved on TRW and COMSAT fabricated modules, they are not unique to a particular skilled operator. A properly designed interconnector configuration employing this material can withstand a thermal shock test comparable to conditions experienced by a lightweight, deployed array during 10 years at synchronous altitude.

Conclusions

Welded solar cell modules fabricated with silver-plated Invar withstood 1,000 deep thermal shock cycles in liquid nitrogen without electrical degradation. Silver-plated Invar is an excellent material for a long-life solar cell interconnector system. The calculated fatigue life exceeds that needed for synchronous orbit operational missions.

The calculated cyclic life exceeds that of any of the other candidate materials by an order of magnitude. This result applies to all types of silver-bonded joints formed on Invar using methods such as parallel gap resistance welding, thermal compression bonding, or ultrasonic bonding. Silver-plated Invar may also offer substantial fatigue life advantages with solder joining.

Acknowledgment

The authors wish to thank Mr. Werner Luft and Dr. Abner Kaplan of TRW for their analysis of the welded interconnect system and the development of the advanced interconnect configuration. Dr. Brij Agrawal of COMSAT Labs was helpful in formulating the fatigue analysis plot on soldered bonds, and Mr. Lee Albright performed the thermal analysis of lightweight solar arrays. The early work on developing weld parameters for pure silver and cleaning techniques for the materials was done by Mr. J. Haynos. The efforts of Mr. Paul Stella of Heliotek and Mr. Ed Zimmerman, formerly of Heliotek, in the early analysis and in organizing some of the welding information are also appreciated. The COMSAT Labs module discussed in the applications section was fabricated by Mr. George Bergeman, who also ran the thermal shock tests.

References

- [1] "Evaluation of Space Station Solar Array Technology and Recommended Advanced Development Programs," First Topical Report, LMSC-A981486, Contract NAS9-11039, December 1970.

- [2] "Evaluation of Space Station Solar Array Technology," First Topical Report Update, LMSC-D159124, Contract NAS9-11-39, July 1972.
- [3] F. G. Treble, "Solar Arrays for the Next Generation of Communication Satellites," RAE Technical Memorandum, Space 185, December 1972.
- [4] "Feasibility Study of a 110 Watt Per Kilogram Lightweight Solar Array System," Final Report, GE Document No. 73SD4256, JPL Contract 953387, May 25, 1973.
- [5] G. Barkats, "Development of a Flexible, Foldout Solar Array," in *International Congress, The Sun in the Service of Mankind Proceedings*, Paris, July 1973, pp. 250-259.
- [6] W. Luft and E. E. Maiden, "Temperature Cycling Effects on Solar Panels," *IEEE Transactions on Aerospace and Electronic Systems*, AES-5, No. 6, November 1969, pp. 943-950.
- [7] E. L. Ralph and J. Roger, "Silicon Solar Cell Interconnectors for Low Temperature Applications," *Proceedings of the International Colloquium on Solar Cells*, Toulouse, France: Gordon and Breach, 1970, pp. 503-518.
- [8] A. M. Salama et al., "Thermoelastic Analysis of Solar Cell Arrays and Their Material Properties," NASA/JPL Technical Memorandum 33-626, September 1, 1973.
- [9] S. S. Manson, "Fatigue: A Complex Subject—Some Simple Approximations," *Experimental Mechanics*, 1965.
- [10] S. S. Manson, *Thermal Stress and Low Cycle Fatigue*, New York: McGraw-Hill, 1966.
- [11] H. S. Rauschenbach and P. S. Gaylard, "Prediction of Fatigue Failures in Solar Arrays," *Proceedings of the Seventh Intersociety Energy Conversion Engineering Conference (IECEC)*, San Diego, California, September 1972.
- [12] N. R. Garner and H. S. Rauschenbach, "Statistical Analysis Applied to Solar Cell Fatigue Failure," *Proceedings of the Seventh IECEC*, 1972.
- [13] J. E. Boretz and R. A. Boring, "Solar Array Concept for a Portable Retractable Oriented Power System," *Proceedings of the Fifth IECEC*, Las Vegas, Nevada, September 1970.
- [14] D. R. Clarke, "High-Temperature Annealable Solar Array," *Proceedings of the Seventh IEEE Photovoltaic Specialists Conference*, 1968, pp. 77-82.
- [15] H. Fischer et al., "A Study on Improved Interconnection Techniques for Silicon Solar Cell Arrays," ESRO C-8 ESTEC Contract 459/67AA, 1969.
- [16] K. K. Reinhartz and J. Capart, "Status of Welded Solar Cell Module Technology," *Proceedings of the Eighth IEEE Photovoltaic Specialists Conference*, 1970, pp. 287-292.
- [17] D. W. Mann and M. Jarvis, "A Study of Advanced Solar Array Design," *Proceedings of the International Colloquium on Solar Cells*, 1970, pp. 451-456.
- [18] H. W. Boller et al., "Solar Cells and Generator Technology for the Helios Sun Probe," *Proceedings of the Ninth IEEE Photovoltaic Specialists Conference*, 1972, pp. 226-236.

- [19] T. C. Eakins, "Results of Solar Cell Welded Interconnection Development," *Proceedings of the Seventh IECEC*, 1972, pp. 651-660.
- [20] R. K. Yasui and L. W. Butterworth, "Structural Analysis of Silicon Solar Arrays," JPL Technical Report 32-1528, 1971.
- [21] P. M. Stella and E. F. Zimmerman, "Silicon Solar Cell—Interconnect System Development," Final Report, INTELSAT Contract CSC-SS-273, 1972.
- [22] W. Luft, "Silicon Solar Cell Improvement," Final Report and Appendices, INTELSAT Contract CSC-IS-361, July 1973.
- [23] R. M. Jones and J. G. Grose, "SAAS II—Finite Element Stress Analyses of Axisymmetric Solids," Air Force Report SAMSO-TR-68-455, 1968.



Denis J. Curtin received a B.S. degree in Physics from Iona College in 1961 and an M.S. in Physics from Catholic University, 1963. In 1967 he joined COMSAT Laboratories, where he is now a member of the technical staff of the Electric Power Department.

Mr. Curtin is author or co-author of numerous publications on radiation effects in solar cells and solar array technology. He is a member of the COMSAT Technical Review Editorial Board,

AIAA, Sigma Pi Sigma, Sigma Xi, and the ASTM Committee on Space Radiation Effects, a reviewer for the IEEE Transactions on Electron Devices, and chairman of the IEEE Photovoltaic Specialists Committee.

Wilfred J. Billerbeck was a Project Supervisor and Senior Staff Member in the Space Division of the Applied Physics Laboratory, Johns Hopkins University; Senior Engineer at Litton Industries in Electronic Countermeasures; and Engineer at Flight Refueling, Inc., and Vitro Laboratories before joining COMSAT, in 1966. He is presently manager of the Electric Power Department of COMSAT Labs.



He received a B.A.E. degree from Catholic University, 1951, and did postgraduate work at the University of Maryland, Catholic University, and UCLA. He is an Associate Fellow of AIAA, former member of the AIAA Technical Committee on Electric Power Systems, and past chairman of the Joint NASA/GSFC Aerospace Industry Battery Committee.

Index: waveguide filters, weight control, design, Invar, thermal expansion, metallurgical analysis, beryllium.

Metallurgical evaluation of fabrication technologies for high-precision microwave filters for space application

J. M. SANDOR

(Manuscript received October 16, 1973)

Abstract

This paper describes and evaluates various fabrication technologies that have been utilized in an ongoing effort to develop an elliptic function circular waveguide filter of reduced weight and/or manufacturing complexity. Because the design of such microwave filters requires a high precision in the finished parts, the current practice is to utilize "Invar," a high-density alloy with a low thermal expansion coefficient requiring complex machining and heat-treatment procedures. The alternative approaches described include vapor deposition by ion plating of Invar alloy deposits onto removable mandrels, use of different metallurgical joining techniques to assemble filters from thin-walled Invar tubes and iris inserts, lay-up and hot isostatic pressing of carbon-aluminum and boron-aluminum composite structures, and conventional machining of filter elements from hot-pressed beryllium powder. The latter approach appears to hold the greatest promise despite the higher thermal expansivity of beryllium as compared with Invar.

This paper is based upon work performed at COMSAT Laboratories and Battelle Memorial Institute/Columbus Laboratories, partly under the sponsorship of the International Telecommunications Satellite Organization (INTELSAT). Views expressed in the paper are not necessarily those of INTELSAT.

Introduction

Narrow-bandpass filters for high-quality microwave communications system applications require good frequency selectivity and small in-band insertion loss. Dual, orthogonal mode, circular waveguide cavity filters exhibiting near-optimum amplitude filtering properties have been designed [1], [2] by utilizing general coupling-cavity theory as outlined by Atia and Williams. Such an approach leads to a marked improvement in frequency selectivity, passband loss, and weight reduction as compared with Chebychev filters of the same order. The weight reduction results from the utilization of two electrical cavities in one physical cavity, a distinct advantage in satellite transponder designs.

The fabrication of such an elliptic function filter requires considerably greater mechanical precision and dimensional accuracy than a Chebychev filter, particularly in the location and dimensional tolerances of the thin coupling slots (irises) separating the four physical (eight electrical) cavities. Furthermore, the elliptic function filter is highly sensitive to dimensional changes arising from thermal expansion of the filter material. Currently, such filters are fabricated from "Invar," an iron alloy containing 36 percent by weight of nickel and exhibiting anomalously low thermal expansion up to about 200°C. The thermal expansion coefficient is extremely sensitive to the alloy composition and reaches a minimum value at the Invar composition (36 percent Ni-64 percent Fe).

Apart from its high specific gravity (8.0), the difficulties and complexity of machining and heat treating this alloy to preserve low thermal expansion are considerable. This paper describes certain alternative fabrication technologies that were explored as part of an ongoing effort to develop a filter of reduced weight and/or fabrication complexity for spacecraft applications. These alternative approaches fall into two main classes, one utilizing Invar material for its low thermal expansion coefficient, and the other utilizing much less dense substitute materials with relatively low thermal expansion coefficients.

Disadvantages of conventional technology

Invar (as a class of iron-nickel alloys) is by far the most popular material currently used for microwave filters in spacecraft transponders because of its dimensional stability over broad temperature excursions. The thermal expansion coefficient, α , is nevertheless a varying property of this material. It is very sensitive to heat treatment and cold work during

fabrication, and sometimes changes with time after fabrication. Thus, for a typical Invar alloy, α has been found [3] to vary from $1.66 \times 10^{-6} \text{ }^\circ\text{C}^{-1}$ after forging to $0.64 \times 10^{-6} \text{ }^\circ\text{C}^{-1}$ after quenching from 830°C, $1.02 \times 10^{-6} \text{ }^\circ\text{C}^{-1}$ after quenching and tempering, and $2.01 \times 10^{-6} \text{ }^\circ\text{C}^{-1}$ after slow cooling from 830°C. The expansion is greatest in well-annealed material and least in quenched material.

By means of cold work, it is possible to produce Invar material with zero and sometimes even negative thermal expansion coefficients. Such methods generally produce instability in the material; with time lapse and variation in temperature, these very low coefficients will usually revert to normal values [3]. Hence it is clear that a balance must be found between low initial coefficient values and acceptable lifetimes.

Machining waveguide filter parts from solid forged block imposes considerable cold work on the material, which usually includes trace amounts of selenium for machinability and manganese to avoid the hot-shortness effects of selenium. Both of these elements act to increase the effective expansion coefficient. Because of possible instability and the high precision required of circular filter components, it is necessary to degrease and stress-relieve parts after each machining operation and to give them a final stability anneal. Thus, a filter with both a sufficient lifetime and an acceptable expansion coefficient may be fabricated without distortions appearing during or after fabrication.

Such conventional machining of filter sections of this design carries with it a penalty of increased filter weight, since wall thickness and flange size must be sufficient to avoid distortions and to withstand the stresses involved in mechanically fastening together sections of the silver-plated microwave filter assembly. In contrast, Chebychev filters may be assembled from thin-walled extruded Invar parts by brazing silver-plated sections together; the dimensional accuracy and lineup of sections are generally far less critical than those of the elliptic function design.

It is evident that Invar machining fabrication technology is not ideally suited even to small-scale production of high-precision filters. The individual handcrafting of sections, the complexity of procedures, the dependence on heat-treatment parameters, and even the increase in expansivity caused by the presence of Se and Mn in the free-machining grade material all stand in the way of lower fabrication cost and lighter filters.

Alternative Invar fabrication technologies

Ion plating

Ion plating is a comparatively new process of physical vapor deposition that has been reported [4] to have certain attributes that make it very attractive for applying an Invar alloy deposit to a removable mandrel:

- excellent throwing power,
- excellent coating adherence without careful precleaning,
- high deposition rates,
- the feasibility of maintaining substrates at or near room temperature,
- the feasibility of achieving multicomponent alloy deposits with the desired stoichiometry.

Several substrates were ion plated with Invar alloy to establish the feasibility of forming free-standing integral waveguide filters by using this technique. Initially, flat substrates were thinly coated, and the deposits were analyzed using X-ray diffraction and fluorescence techniques. Results indicated that the diffraction pattern obtained from an ion-plated layer was identical to that obtained from a commercial Invar sample, confirming the presence of the face-centered-cubic (γ) alloy phase exhibiting a low thermal expansion coefficient. Chemical analysis indicated off-stoichiometry in the direction of 2- to 3-percent excess iron composition. The source material, prepared from iron and nickel powders with a minimum purity of 99.99 percent by vacuum casting, was adjusted accordingly to deposit the 36 ± 0.5 -percent nickel composition.

Cylindrical aluminum mandrels were machined to the internal dimensions of a 4-GHz bandpass filter section and assembled with a thin Invar insert having a diameter slightly larger (by 0.5 mm) than the mandrel, as indicated in Figure 1. Experiments were then performed in an attempt to ion plate a 0.75-mm-thick Invar layer onto a rotating mandrel assembly.

Inspection of the resulting coating around the edges of the iris plate revealed a total lack of bridging of the ion-plated deposit across the aluminum-Invar interface. At these interfaces, the coating appeared to have cracked apart (Figure 2), although it was found to be well bonded to both aluminum and Invar surfaces.

The cause of cracking was identified as a high substrate plating temperature combined with the large expansion difference between the mandrel and iris plate. (Because of the rotation necessary to achieve a uniform coating, it is impracticable to water cool the mandrel.) Attempts were

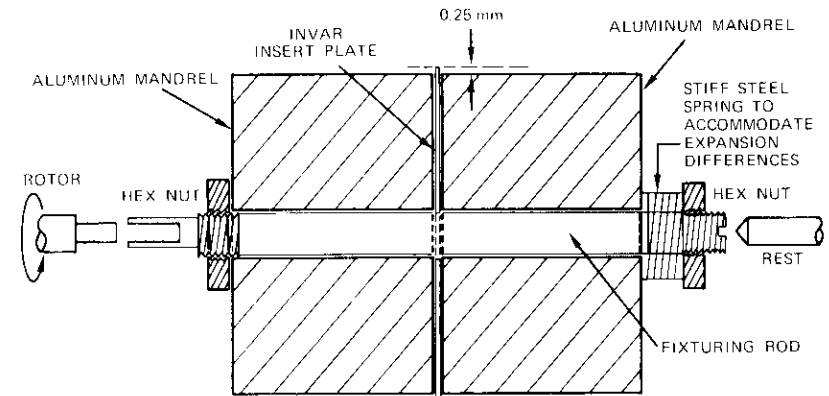


Figure 1. *Fixtured Assembly of Mandrels and Insert Plate for Ion-Plating Experiments*

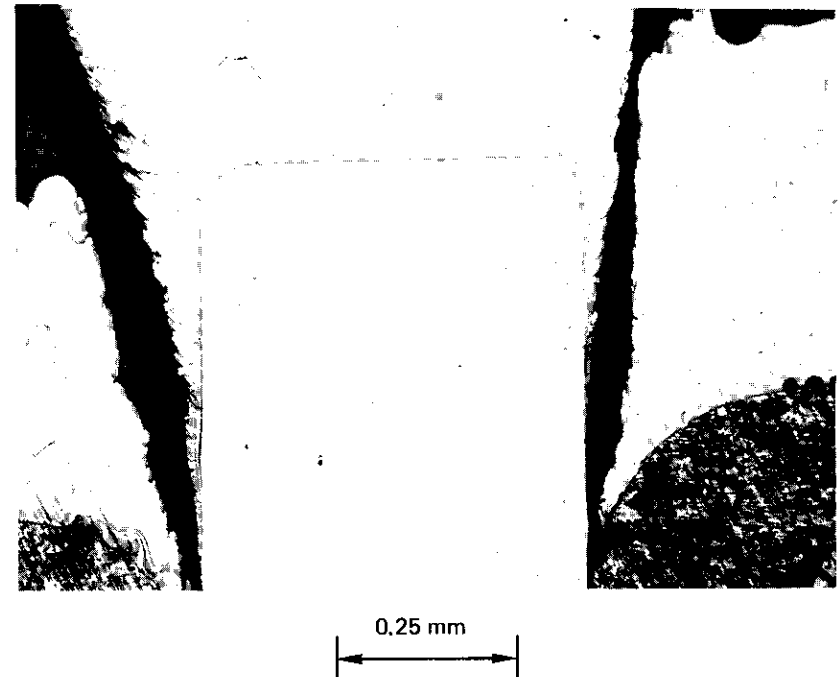


Figure 2. *Crack Formation in Plating Between Invar Insert and Aluminum Mandrels*

made to reduce substrate temperatures during coating by reducing power and ion flux, but deposition rates became too slow for practical application. Finally, graphite mandrels were substituted for the aluminum and ion plated in an effort to reduce expansivity differences (Figure 3). The bridging showed a slight improvement (Figure 4), but after the assembly fasteners were removed, the plated graphite soon detached from one face of the iris plate during normal handling. Obviously, the problem of chemical mandrel removal becomes acute when graphite is utilized, and because of the insufficient improvement in bridging, a solution to this problem was not pursued.

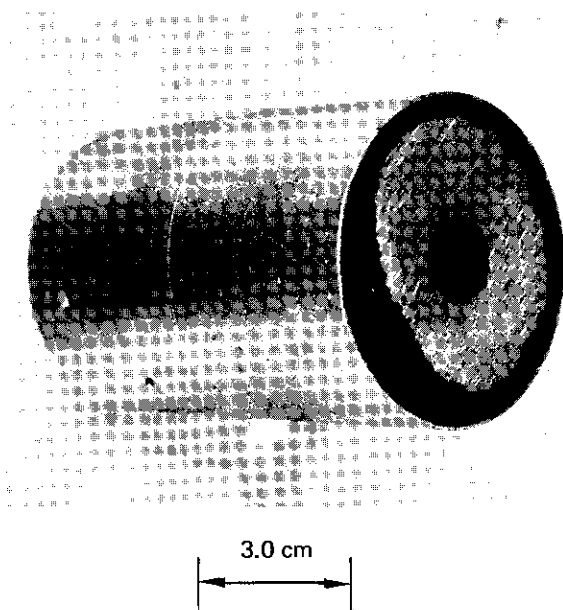


Figure 3. *Invar Ion-Plated Graphite Mandrels without Fixturing and After Partial Removal of Plating on End Faces*

In view of the favorable appearance and acceptable thickness of coating obtained on the graphite mandrel, mechanical strength and thermal expansivity were measured before and after a 30-minute period of annealing at 480°C (900°F) in a forming-gas atmosphere (90 percent N₂—10 percent H₂).

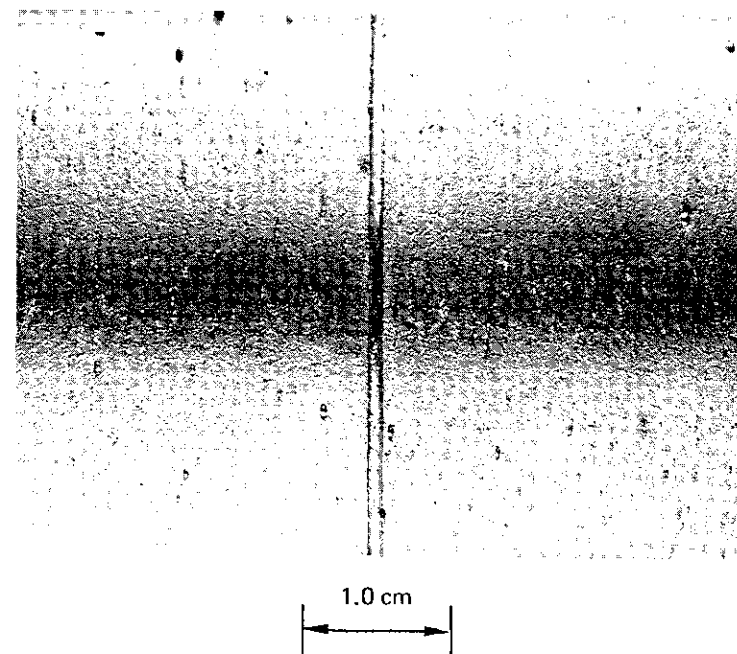
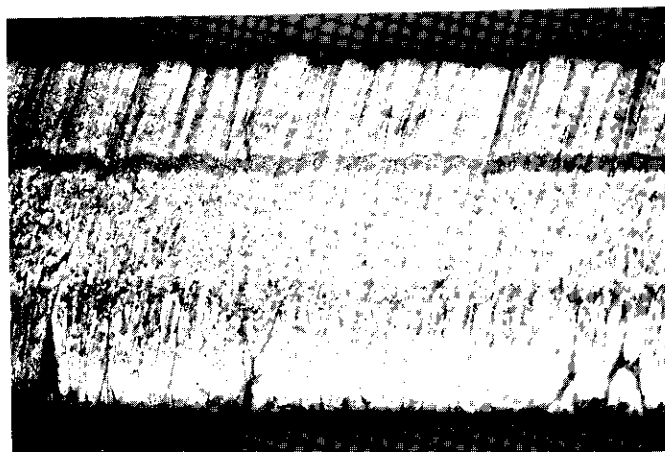


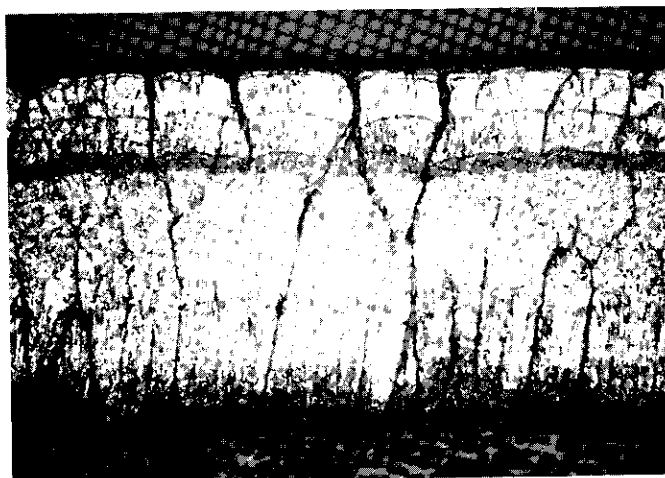
Figure 4. *Partial Bridging of Plating Across Invar Insert*

The average tensile strengths of samples cut parallel to the cylinder axis were extremely low: 3,200 N · cm⁻² for As-plated samples, and 4,250 N · cm⁻² for As-annealed samples (based on three tests each). In view of these data and the distortion found during annealing, it was concluded that high residual tensile stresses were grown into the coating. Figure 5 shows the microstructure of As-plated and As-annealed tensile test samples. Figure 5a indicates the distribution of microcracks grown into the coating, and Figure 5b shows the extensive interfacial network subsequently formed during annealing. It is also evident that the ion-plating process was interrupted during this particular experiment, and that the grain structure became laminar rather than columnar after the resumption of ion plating.

The thermal expansion measurements (by thermal dilatometry) confirmed that the λ-Invar phase was in fact being deposited: $3.0 \times 10^{-6} \text{C}^{-1}$ (As-plated) and $2.3 \times 10^{-6} \text{C}^{-1}$ (As-annealed) over the range of 20°C to 120°C. The relatively high values for Invar and the decrease with annealing both lead to the tentative conclusion that iron and nickel ions were



a. As-Plated



b. As-Annealed (480° for 30 min)

Figure 5. Cross Sections of Ion-Plated Invar

being plated out alternately rather than simultaneously on a microscopic scale. The local alloy composition at any point would then deviate significantly from the average 36-percent Ni-64-percent Fe composition, but such microscopic fluctuations would be "damped out" by iron and nickel atom interdiffusion during annealing.

The findings of these ion-plating experiments may be summarized as follows:

- a. the substrate is subjected to excessive temperatures during the process, resulting in negligible bridging and failure to incorporate the iris plate into the plated layer,
- b. the strength and expansivity properties of ion-plated Invar appear to be deficient.

Joining of thin-walled tubes

Any concept of metallurgically joining thin-walled tubes and iris plates of Invar must ensure extremely close control of mechanical fit-up, and must avoid distortion during the joining process, particularly "oil-canning" (bowing) of the iris plates and end caps of the filter assembly.

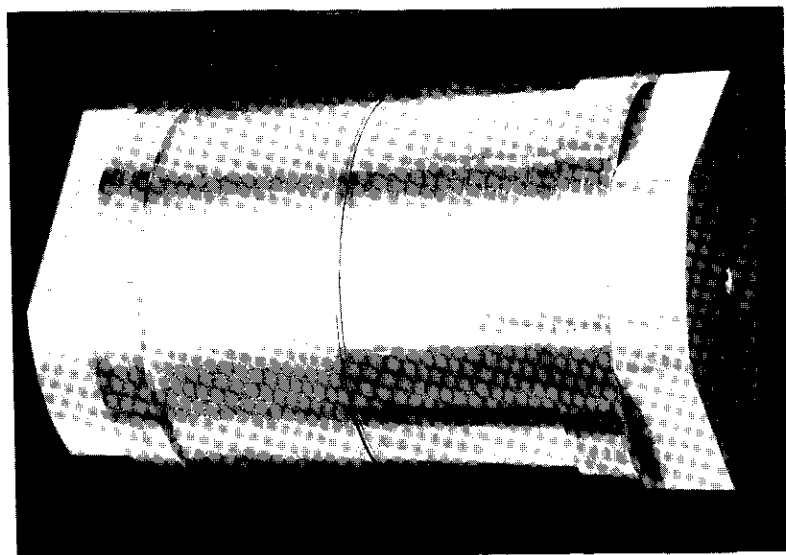
ELECTRON-BEAM WELDING

Electron-beam (EB) welding achieves very narrow welds with low heat input and therefore low distortion, combined with high speed of joint production (see, for example, Reference 5). A vacuum is necessary, and because of the small size of the focused electron beam, the quality of pre-weld joint preparation must be very high. In general, however, no pre- or post-heat-treatment is needed for EB welded assemblies.

Tubing was prepared by cold drawing of low-impurity Invar billets, and machined to the internal filter diameter and 1-mm wall thickness. Special fixtures (Figure 6) enabled two cylindrical parts to be aligned coaxially with a 0.5-mm-thick iris plate and horizontally rotated. A thin dowel pin passing through the iris plate was used to center it between the cylinders.

Flanges of varying size were also machined on cylindrical parts in order to study closure of subassemblies to produce full filters. In addition, a single such fixture was used to support a cylinder and 1-mm-thick end cap with vertical rotation axis.

Several EB welding experiments were performed to optimize the parameters, namely, beam voltage and current, beam deflection amplitude and overfocus distance, and assembly rotation rate. Both silver-plated and nonplated Invar parts were welded.



3.0 cm

Figure 6. Invar Parts Assembled for Electron-Beam Welding Using Special Aligning Fixtures

The successfully welded assemblies were visually examined for distortion effects prior to metallographic examination. In each such assembly, however, the iris plate was found to have "oil-canned" to a greater or lesser extent (a measured bowing of 0.1 to 0.5 mm at the plate center). Distortion was found even in the case in which heat input as a function of EB power level was set at a minimum to achieve a successful weld (i.e., 70 kV at 2.5 mA with side-to-side beam deflection of 0.5 mm, over-focus distance of 10 mm, and 2-rpm rotation rate). Furthermore, it was found that, even at these lowest power settings, the weld fusion zone often penetrated past the cylinder's interior surface and well into the iris plate, as shown in Figure 7. This photomicrograph also shows (on opposite sides of the iris plate) the inside weld fillet associated with a large fusion zone, and the result of machining the fillet to give a corner with a small radius.

Machining the fillet generally altered the internal dimensions of the part, except in the case of a silver-plated weld assembly in which the fillet



0.5 mm

Figure 7. Fusion Zone Created by Electron-Beam Weld of Invar Cylinders to Iris Plate

(silver only) was burnished and negligible Invar material was removed. Figure 8 indicates the success with which the weld fusion zone in this experiment was contained within the outer wall material. However, the iris plate became severely oil-canned during welding, the silver was found to have been melted into an irregular fillet, and the adjacent silver plating was seen to flake off during the burnishing operation.

The conclusion drawn from the EB welding experiments was that the asymmetry of heat input during the process was responsible for the bowing or oil-canning. As the Invar material adjacent to the weld within the iris plate exceeded about 300°C, its thermal expansion reverted to normal nickel-steel values (11 to $15 \times 10^{-6} \text{ } ^\circ\text{C}^{-1}$), and severe thermal stresses could become frozen into the iris plate as the electron beam proceeded around the circumference. These stresses could then be partially relieved by bowing out the iris plate. It is significant that the thicker (1-mm) end caps, welded sideways onto a single cylindrical part (and without a central

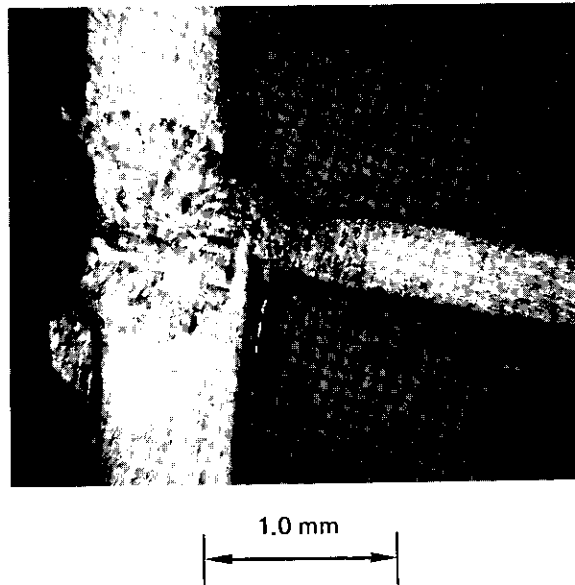


Figure 8. *Electron-Beam Weld of Silver-Plated Invar Parts Showing Well-Contained Fusion Zone, Burnished Fillets, and Severely Bowed Iris Plate*

hole for fixturing purposes), displayed a similar oil-can distortion after welding. In contrast, EB welding of two flanged cylinders without an iris plate was achieved without any measurable distortion.

SOLDERING

The design of the fixtures used for soldering together cylindrical parts and iris plates was identical to that of the fixtures used for EB welding, except that the former were fabricated from Invar to match changes in dimensions during the extended periods of oven heating and cooling.

Initial tensile lap-shear measurements indicated a twofold increase in strength for Invar parts soldered without silver plating as compared with plated parts ($4,100 \text{ N} \cdot \text{cm}^{-2}$ versus $1,600 \text{ N} \cdot \text{cm}^{-2}$). It was therefore decided to silver plate the parts after joining.

Joint interfaces were pretinned with eutectic tin-lead solder after vapor degreasing and flux treatments. The flux was carefully applied with a clean camel's hair brush to only those surfaces requiring wetting (to control the size of solder fillets). The solder was applied by hand iron to give a

bead 0.25 to 0.5 mm wide on each surface to be joined. Beads were closely examined for such features as uniformity and lack of voids and contamination. Flux residues were cleaned off and, with the cylinder axis vertically aligned in the oven, parts were assembled on clean fixtures and positioned symmetrically about this axis.

Reflow of the solder was monitored during oven heating by using a thermocouple adjacent to the joint, and the reflow temperature was maintained for five minutes to allow proper flow and fillet formation. Parts were very slowly heated and cooled to avoid distortions, and great care was taken to avoid jarring the oven and parts prior to completion of bonding. A typical soldered assembly (Figure 9a) vibrated to INTELSAT IV satellite qualification levels showed no resultant damage. Although solder fillets were visually uniform in appearance, it became evident after applying plating (nickel, silver, and gold) that solder reflow had left pores and voids in the joints, and allowed trapped plating solutions to subsequently leach out after corroding material under the plating (see Figure 9b). Furthermore, careful dimensional checks of several assemblies proved that the fixturing was ineffective in preventing significant misalignment of the two cylinder axes, both radially and longitudinally, as a result of the collapse of the solder beads during reflow.

Alternative fabrication technologies using lightweight materials

Fiber-reinforced composite materials

As replacements for Invar, fiber-reinforced composite materials meet many of the stringent requirements for microwave filter applications, notably low thermal expansion and extremely light weight. However, they must also exhibit dimensional stability in vacuo and survive satellite launch conditions.

A composite made up of an aluminum matrix reinforced with very thin graphite "multifibers" was initially chosen for study [6] as a replacement for Invar because of its vacuum stability and platability with silver. Aluminum-plated multifibers were consolidated by hot isostatic pressing (HIP) into cross-ply lay-ups, and the lay-up properties were examined. Although extremely low expansion values were measured for the cross-ply material, its strength was found to be unacceptably low for satellite use (a tensile strength of less than $10,000 \text{ N} \cdot \text{cm}^{-2}$ as compared with a strand strength of $150,000 \text{ N} \cdot \text{cm}^{-2}$ and higher).

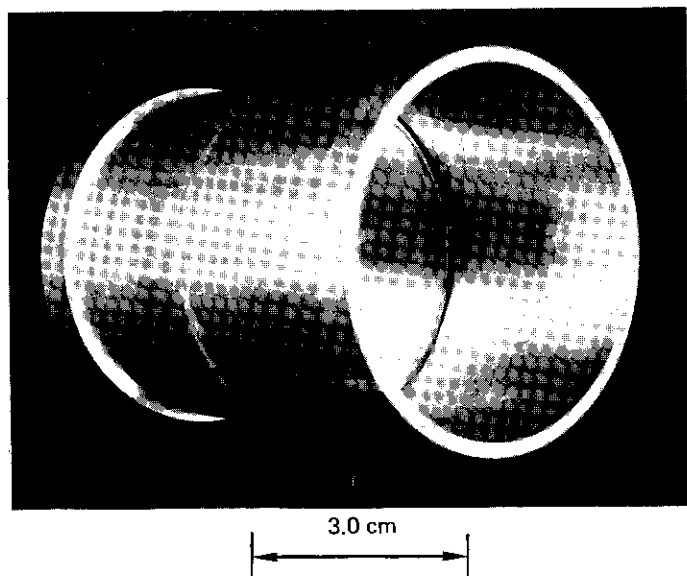


Figure 9a. *Invar Assembly Soldered with Tin-Lead Solder and Used for Vibration Testing*

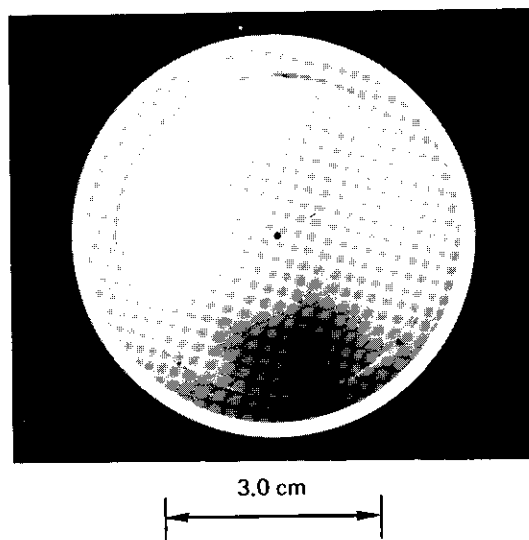


Figure 9b. *As-Plated Interior of Assembly Showing Voids in Solder Joint*

After many experiments, it was concluded that applied stresses were not being transferred to all fibers simultaneously because of poor internal bonding, and that considerable damage was being sustained by the crossed fibers as a result of the high pressures required for the HIP lay-up. However, a filter element (section) was fabricated by HIP from an aluminum matrix composite reinforced with 0.1-mm-diameter boron "monofilament" fibers (as compared with the 0.006-mm-thick graphite multifiber). The cylinder and flanges were bonded together independently of the iris plate, which was then internally soldered into place on a ledge machined out of the internal cylinder surface (an aluminum skin).

Figure 10 shows the part after being plated with silver; some silver flaking and lack of coverage of the iris joint can be detected. The different boron fiber orientations in a test cylinder section and iris plate can be compared in Figure 11a, which shows a cross section of a solder joint. Figure 11b, which shows a lay-up using cross-plyed graphite multifibers, is included for further comparison.

It was found that the properties of the boron-aluminum composite were borderline for satellite use. Although the tensile strength was around $35,000 \text{ N} \cdot \text{cm}^{-2}$ and the vacuum weight loss was less than 0.05 percent, the expansion coefficient was found to approach $1 \times 10^{-5} \text{ }^{\circ}\text{C}^{-1}$ for the pseudoisotropic lay-up. This value is twice that reported [7] for cross-plyed lay-ups of boron fibers in an epoxy rather than an aluminum matrix. More significantly, the dimensions of the composite filter element failed to meet drawing requirements for iris location, cylinder size, and flange hole dimensions. Further development of a composite filter now awaits advances in coating and HIP lay-up of graphite multifibers, which in turn could produce structures having the lowest expansion together with acceptable strength and structural integrity.* Advances in HIP processing of boron-aluminum lay-ups would make it possible to achieve accurate dimensions and reduce thermal expansion by modifying lay-up ply orientations and improving internal bonding.

Beryllium

Given the acceptability of a thermal expansion coefficient around $1 \times 10^{-5} \text{ }^{\circ}\text{C}^{-1}$, a viable alternative to the boron-aluminum composite is hot-pressed beryllium powder. A specific gravity of 1.85, coupled with

* It has been reported [8] that a recently developed process for liquid-phase infiltration of graphite multifibers achieves excellent coating of the fiber surfaces by the matrix, with consequent strength gains.

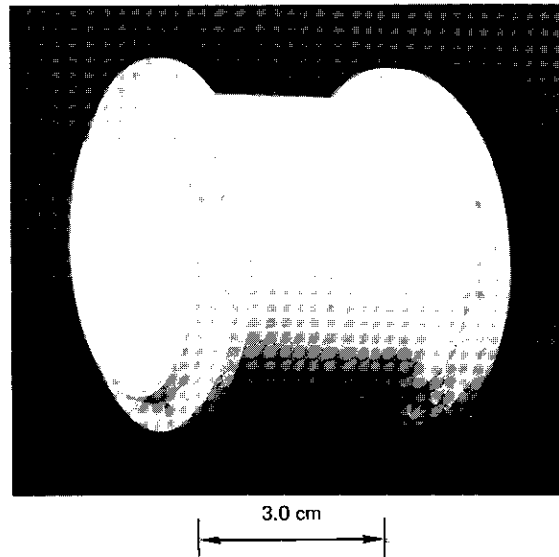
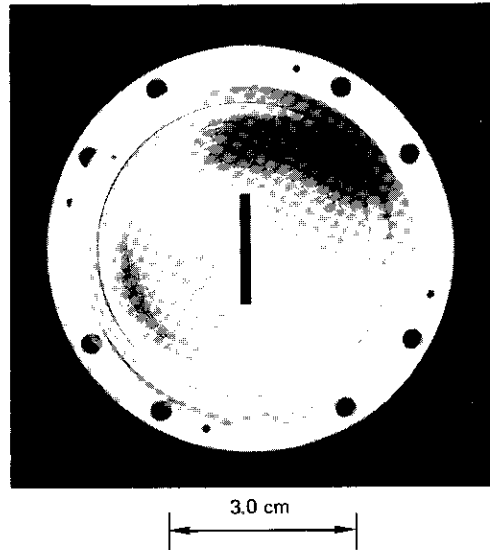


Figure 10. Boron-Aluminum Composite Filter Element Fabricated by Hot Isostatic Pressing

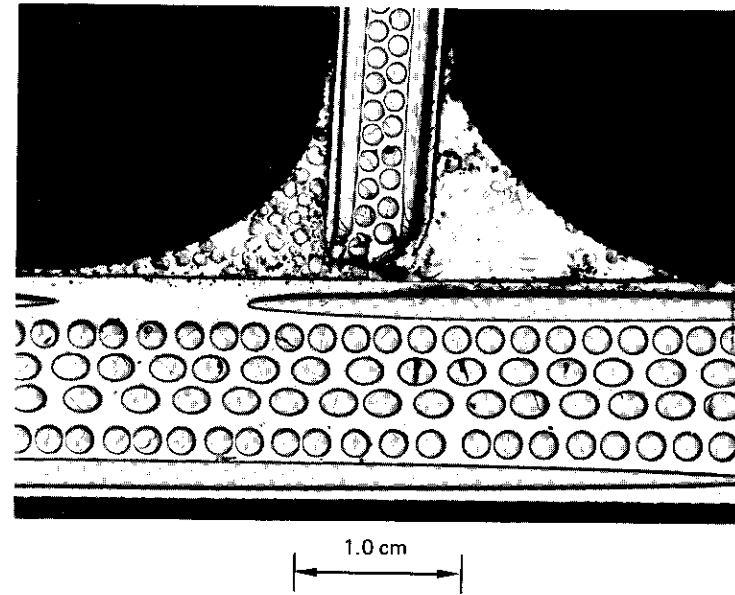


Figure 11a. Cross Section of a 6-Ply Boron-Aluminum Cylinder Soldered to a 4-Ply Iris Plate with Eutectic Tin-Lead

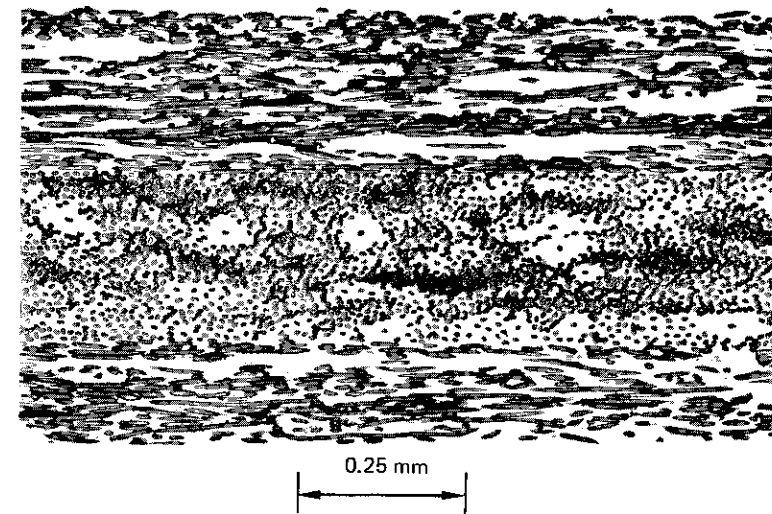


Figure 11b. Section Through 3-Ply Graphite-Multifiber/Aluminum Lay-Up Showing Voids and Nonuniform Fiber Distribution

an elastic modulus of $28 \times 10^6 \text{ N} \cdot \text{cm}^{-2}$, makes beryllium (with $\alpha = 1.16 \times 10^{-6} \text{ } ^\circ\text{C}^{-1}$) an attractive alternative to Invar. However, the spacecraft environment must be controlled sufficiently that thermal expansions of a beryllium filter lie within acceptable limits. With this provision in mind, it was decided to explore the feasibility of fabricating and silver plating a filter element of beryllium.

Because of the poor quality of welded beryllium joints and the property losses caused by grain growth and recrystallization of brazed joints, a filter element was conventionally machined by a qualified machining house from hot-pressed beryllium block (containing only 1.75 weight-percent of oxide) exactly to the Invar filter drawing tolerances. A simple annealing treatment at 890°C relieved residual machining stresses without any resulting distortion. It was determined that the part had a sufficiently high surface quality (absence of microcracking) and finish so that no chemical etching was indicated, thereby achieving the tight tolerances required.

The thin but tenacious beryllium oxide film present on the metal was successfully removed by a zincate coating, and the part was then silver plated by using a conventional sequence of operations.

Electrical testing indicated that the beryllium part was fully interchangeable with the equivalent Invar part at ordinary temperatures despite the somewhat rougher surface of the beryllium (250 to 300 rms μm versus 75 to 100 rms μm). The beryllium and Invar filter parts are shown side by side in Figure 12. It was found that the beryllium filter achieved a weight savings of 66 percent over the Invar filter.

Conclusion

Several fabrication technologies have been explored as alternatives to the production of circular microwave filters from machined Invar block. Deposition of a free-standing structure of Invar material by using the ion-plating technique was found to result in serious deficiencies in physical properties. Joining of Invar tubes and iris plates by both electron-beam welding and soldering was achieved only with a degradation in assembly dimensional tolerances.

Hot isostatic pressing (HIP) of graphite-aluminum was found to yield a very lightweight material with low thermal expansion, but one which nevertheless had unacceptably low mechanical properties. On the other hand, HIP-bonded boron-aluminum was utilized with some success to fabricate a filter element. However, the mechanical dimensions of the

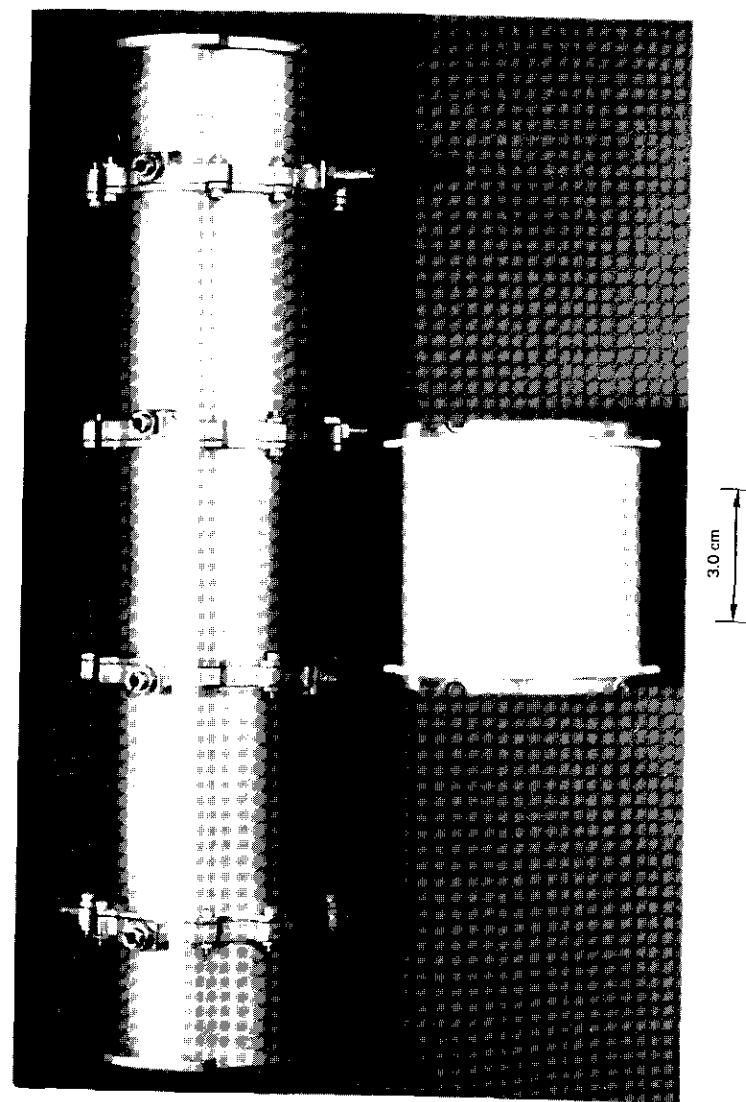


Figure 12. Conventional Invar Filter Assembly Plated with Silver and Gold
Together with Beryllium Filter Element Plated with Silver Only

part were unacceptable and the thermal expansion coefficient was found to have an unexpectedly high value when compared with values for boron-epoxy.

It was judged that a possible substitute material for Invar could be realized by utilizing beryllium metal to fabricate filter assemblies given a spacecraft temperature stabilized within $\pm 15^\circ\text{C}$. A consequent weight savings of 65 percent or more could then be realized.

Acknowledgments

The author wishes to express his thanks to L. Sparrow and W. Cox for their collaboration in the experimental work, to P. Schrantz and A. Williams for performing vibration and electrical tests, to A. Berman and L. Pollack for introducing him to the problem, and to P. Váradi for valuable suggestions and encouragement during the course of this work.

INTELSAT-sponsored work included fabrication of composite materials by J. Fleck and K. Meiners of Battelle/Columbus Laboratories. COMSAT-sponsored work included ion-plating experiments carried out by W. Stowell, also of Battelle; electron-beam welding experiments performed by arrangement with Kin-Therm, Inc. (East Windsor, Connecticut); and machining of the beryllium filter element by Hardric Laboratories (Waltham, Massachusetts). Their cooperation is gratefully acknowledged.

References

- [1] A. E. Atia and A. E. Williams, "Narrow Bandpass Waveguide Filters," *IEEE Transactions on Microwave Theory and Techniques*, MTT-20, No. 4, April 1972, pp. 258-265.
- [2] A. E. Williams, "A Four-Cavity Elliptic Waveguide Filter," *IEEE Transactions on Microwave Theory and Techniques*, MTT-18, December 1970, pp. 1109-1114.
- [3] M. A. Hunter, "Low Expansion Alloys," *Metals Handbook*, 8th edition, Vol. 1, American Society for Metals, pp. 816-817.
- [4] D. L. Chambers, D. C. Carmichael, and C. T. Wan, "Deposition of Metal and Alloy Coatings by Electron-Beam Ion Plating," *Sputtering and Ion Plating*, NASA Publication SP-5111, pp. 89-114.
- [5] J. D. Russell, K. W. Brown, and M. J. Adams, "Electron-Beam Welding Thick-Walled Pressure Vessels," *Metal Construction and British Welding Journal*, November 1972, pp. 399-407.
- [6] Contract development work, Battelle Memorial Institute, Columbus, Ohio, under INTELSAT sponsorship.

- [7] S. A. Bortz, *Development of Engineering Data on the Mechanical and Physical Properties of Advanced Composite Materials*, AFML-JR-72-205, Part I, September 1, 1972.
- [8] E. G. Kendall, Aerospace Corporation, personal communication.



J. Matthew Sandor was born in England and received his B.A. in the natural sciences with honors from Cambridge University. He received his M.S.E. in metallurgical engineering from the University of Michigan in 1966, and his Ph.D. in metallurgy and materials science from M.I.T. in 1970. In 1971 Dr. Sandor came to COMSAT Laboratories, where he is a member of the Device Physics Department responsible for the metallurgy laboratory and hybrid circuit bonding facility. He is currently engaged in research on interconnection bonding and microwave integrated circuit technology.

Dr. Sandor is a member of ASM, AAAS, and the Electrochemical Society.

Index: transponders, Intelsat IV, communications satellites, earth stations, spacecraft antennas, modulation.

Domestic and/or regional services through Intelsat IV satellites

J. L. DICKS

(Manuscript received October 2, 1973)

Abstract

The introduction into service of high-power satellites with multitransponder capability, such as those of the INTELSAT IV series, makes possible the application of satellite technology to communications services other than the present international telephony and television. These international services, initiated at a time when satellites were limited in their power capability, required earth stations with large antennas and low-noise, cryogenically cooled receivers to obtain overall satisfactory system performance. Although the system has changed from a power-limited mode to a bandwidth-limited mode, antennas and receivers of this design are still required to maximize the overall available satellite capacity.

This paper examines the technical feasibility of various potential services obtainable with smaller antennas and simpler earth stations. System performance is calculated as a function of the earth station gain-to-noise temperature ratio, G/T , and the capacity of INTELSAT IV transponders is presented as a function of earth station G/T , modulation techniques, and TV performance characteristics.

This paper is based upon work performed at COMSAT under the sponsorship of the International Telecommunications Satellite Organization (INTELSAT.) Views expressed in this paper are not necessarily those of INTELSAT.

Introduction

The introduction of operational and spare INTELSAT IV satellites into all ocean regions is now well underway. The availability of these satellites has led to studies concerning the use of smaller and simpler earth stations for special applications that involve relatively low communications capacity requirements. Systems or networks can be designed and optimized to provide both telephony and television services as functions of traffic distribution and requirements. Instead of being directly connected to the regular INTELSAT network, these networks are expected to be self-contained. Access to the international system would be provided through the normal international gateway stations for the country or regions of interest. This self-containment feature would provide the opportunity to individually optimize each system in terms of system parameters, such as space-segment requirements, earth station size and configuration, facilities, and modulation techniques to minimize costs.

The use of smaller earth stations can be expected to increase as telecommunications services via satellite expand with the introduction of new satellite systems. Since it is expected that only the largest users can afford to actually implement separate satellite systems, smaller users are most likely to lease space-segment capacity. Detailed trade-off analyses, as described in this paper, will ensure that maximum utilization can be obtained and maintained over the lifetime of the system.

System considerations

To provide specialized services through an INTELSAT IV satellite, the basic parameters of this satellite, which was developed primarily to satisfy the requirements of the INTELSAT global network, must be taken into account [1]. In addition, and consistent with present policy, space-segment costs for any specialized service are directly related to satellite capacity utilization. Therefore, tradeoffs will be performed to determine the modulation techniques leading to the optimum development of the earth-segment configuration and the maximum efficiency from the space segment.

While the primary objective is to develop the most satisfactory network capable of meeting stated system requirements at the lowest cost, some compromises may be necessary because of technical constraints. For instance, earth stations with small apertures may have to be equipped with some additional facility for repositioning the antenna or tracking

the satellite, since normal INTELSAT requirements may allow a considerable drift or inclination buildup on a particular satellite.

Transponder capacities for telephone service

Earth station G/T ratios, satellite e.i.r.p., and the traffic handling capability of satellite transponders are interdependent. For a given satellite e.i.r.p., larger transponder channel capacities are achieved as earth station G/T ratios are increased. Also, the capacity achieved with any specified satellite e.i.r.p. and earth station G/T ratio is dependent on the type of modulation, multiplexing, and multiple access utilized. The techniques to be considered are modified time-domain multiple access (TDMA), frequency-division multiplex/frequency modulation (FDM/FM), and a modified form of the single-channel-per-carrier demand-assignment system [2]. In these cases the modifications consist primarily of simplifications in the control systems and facilities provided to adapt their use to low-capacity systems and consequently reduce their cost.

The channel capacities of transponders operating in the global- and spot-beam modes are shown in Figures 1 and 2, respectively, as functions of the receive earth station G/T and modulation method. The channel capacity shown is a selected composite curve based on the use of the most appropriate gain step* in the up-link, as the system is optimized for varying ranges of earth station receive G/T.

This change in gain step is important to the optimization process, since it maintains a balance between the relative noise contributions of the up- and down-links as the receive earth station G/T varies. Gain step changes are also necessary when switching from the global- to the spot-beam mode of operation, since in this case, the increased down-link e.i.r.p. available requires more up-link power. Hence, the reduction of satellite gain achieved by changing the gain steps prevents saturation of the transponder when increased earth station power is provided.

When FDMA is used, the transponder intermodulation contribution must also be considered. The optimum operating point will then be a function of the earth station G/T, and will differ for global- and spot-beam operation.

* Transponder gain is varied by adjusting the 4- or 8-position switch attenuator provided at the input to each transponder. Each attenuator setting changes the transponder gain by approximately 3.5 dB.

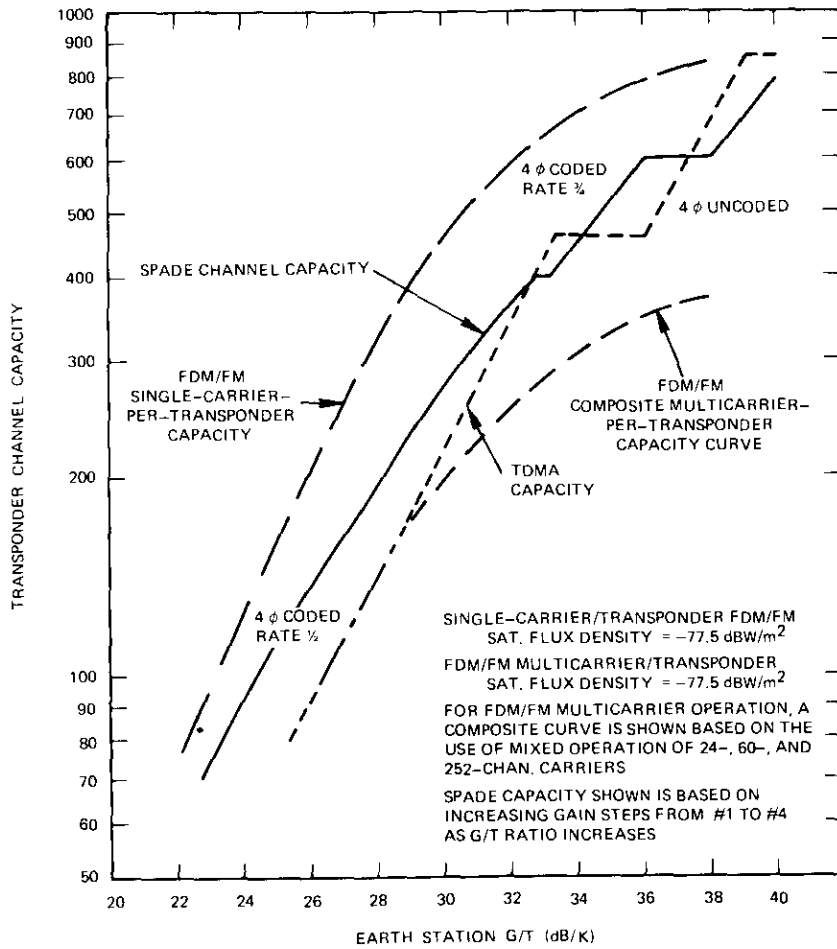


Figure 1. Global-Beam Transponder Channel Capacity as a Function of Earth Station G/T

Transponder television capability

Figures 3 and 4 show television performance for spot- and global-beam operation as a function of the receive earth station G/T ratio for both FM and digital modulation.

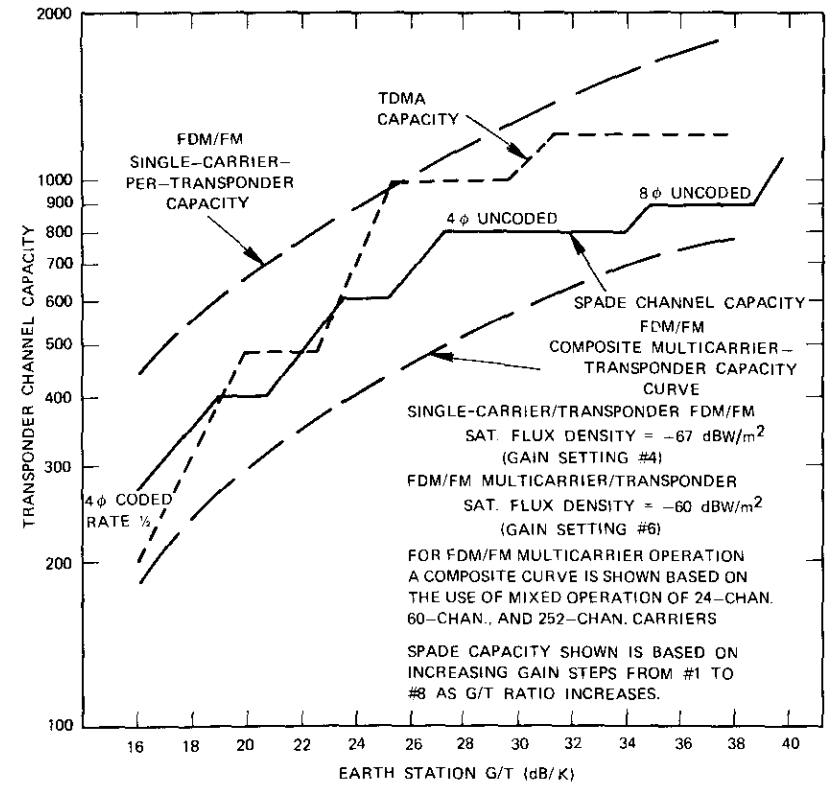


Figure 2. Spot-Beam Transponder Channel Capacity as a Function of Earth Station G/T

Global-beam operation

For FM, the curve in Figure 3 shows the variation of the TV signal-to-noise ratios as a function of the receive earth station G/T. Since this case is equivalent to single-carrier-per-transponder operation, the selection of gain step no. 1 was considered the best compromise.

Signal-to-noise ratios were calculated by assuming that full power and bandwidth were available for use on the video carrier, and that the associated audio channels would be submultiplexed onto this carrier. It should be noted that overdeviation (up to a maximum of 3 dB) was used to obtain the required S/N ratio at the lower G/T values.

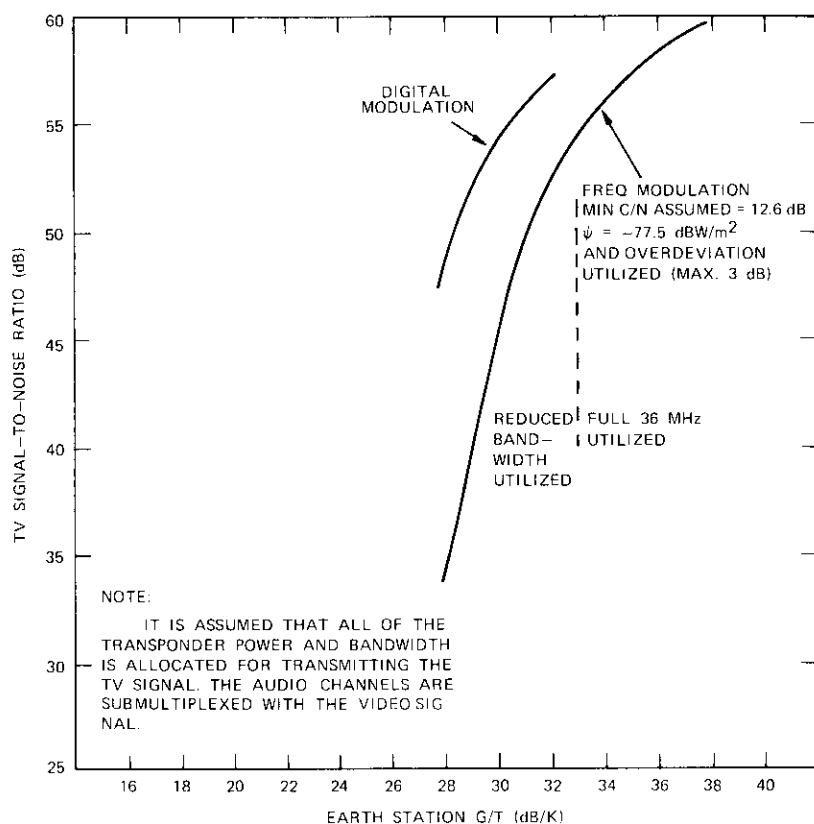


Figure 3. Global-Beam Transponder Television S/N as a Function of Earth Station G/T

As shown in Figure 3, for receive G/T s greater than 33 dB/K, the full bandwidth can be utilized without allowing the C/N ratio to drop below the assumed 12.6-dB minimum. Below this G/T value, a reduced bandwidth must be utilized to maintain the C/N ratio above threshold. Figure 3 also shows the variation of signal-to-noise ratio as a function of the receive earth station G/T for digital modulation.

Spot-beam operation

Figure 4 shows the TV capability of a spot-beam transponder when transmitting either one or two FM TV channels. Curve A shows the

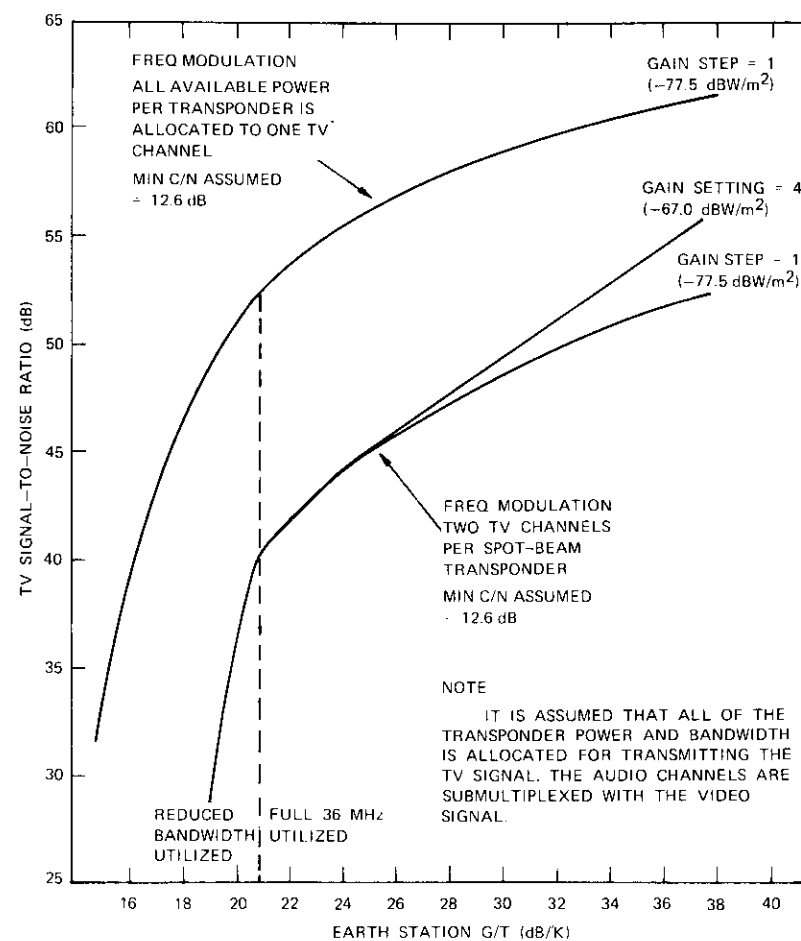


Figure 4. Spot-Beam Transponder Television S/N as a Function of Earth Station G/T

variation of the signal-to-noise ratio as a function of the receive station G/T when the full power and bandwidth can be utilized for one TV channel. Curve B shows the same variation, although in this case, the transponder is assumed to be simultaneously transmitting two TV channels.

Space-segment versus earth station cost tradeoffs

For both telephony and television services, cost tradeoff analyses were performed to determine the optimum earth station G/T ratios for particular service applications and selected modulation techniques. Separate networks or subsystems within the INTELSAT system with no connection to the global INTELSAT system were assumed.

Study approach

As shown previously, the earth station G/T, the satellite e.i.r.p., and the traffic capability of the system are interdependent. However, the earth station antenna size and system noise temperature selected both have an important economic effect on the system, particularly when a large number of stations is being considered.

Optimum earth station G/T ratios were obtained from system tradeoff analyses involving comparative earth station and space-segment costs. For a given service application, in terms of traffic level and distribution, as the earth station G/T is reduced (generally resulting in lower station costs), a corresponding increase in satellite power is necessary (generally resulting in higher space-segment costs) to maintain the desired transmission performance. The optimum earth station G/T ratio is defined as that point at which the system (earth station and space-segment) costs are the lowest for a specific traffic level. Earth station cost estimates are based on information drawn from manufacturers and in-house sources.

Unit costs for the space segment are calculated by dividing the voice channel capacity of an INTELSAT IV transponder, derived as a function of the earth station G/T, satellite e.i.r.p., and modulation technique utilized, into selected annual transponder revenue requirements. Since future space-segment lease rates for earth station owners were not available, a range of annual transponder revenue requirements was selected to bracket possible future rates.

System configuration

The desired system configuration must provide domestic, regional/international, or other special services through INTELSAT IV global- and spot-beam transponders. Traffic requirements, ranging from a few to several hundred telephony channels per earth station, and TV distribution requirements must also be satisfied. Typical systems synthesized from the basic elements of this study include 4-100 earth stations.

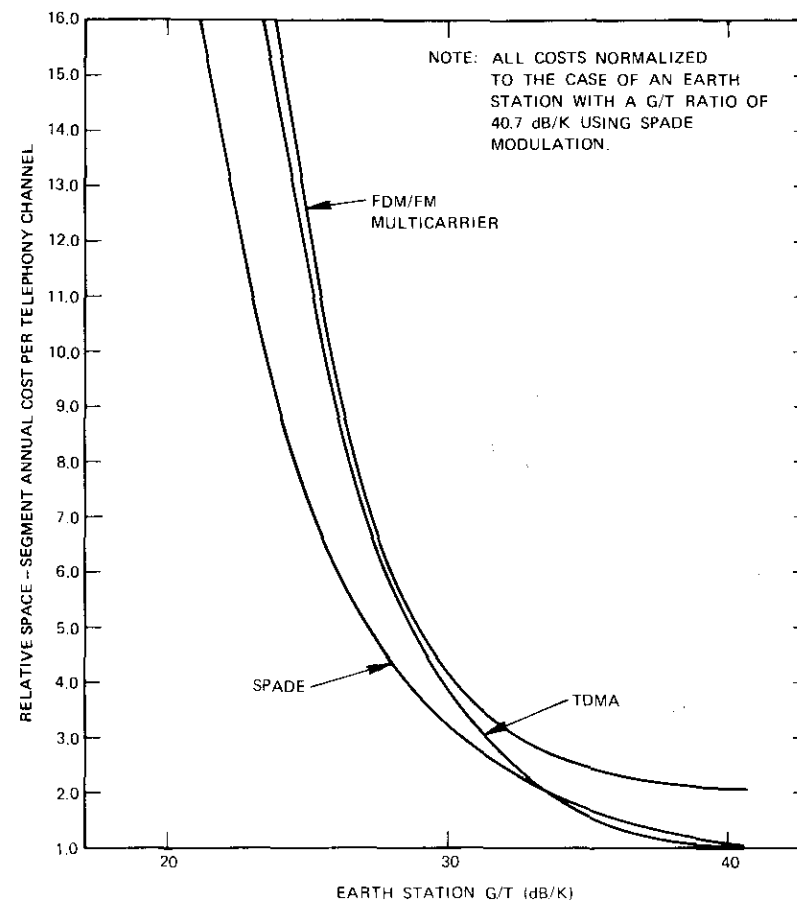


Figure 5. Relative Space-Segment Cost, Global-Beam Transponder

Relative space-segment costs

For an entire global-beam transponder accessed by earth stations employing the same modulation technique, the relative space-segment unit costs of various modulation techniques are given in Figure 5. This figure shows that the use of SPADE generally results in the lowest space-segment unit costs. When spot-beam transponder operation is assumed (Figure 6), the lowest costs are achieved by using TDMA modulation. The SPADE

cost curve lies between the TDMA and multicarrier FDM/FM curves. However, SPADE or FM would probably be selected for either spot- or global-beam operation since the TDMA system is still in the developmental stage.

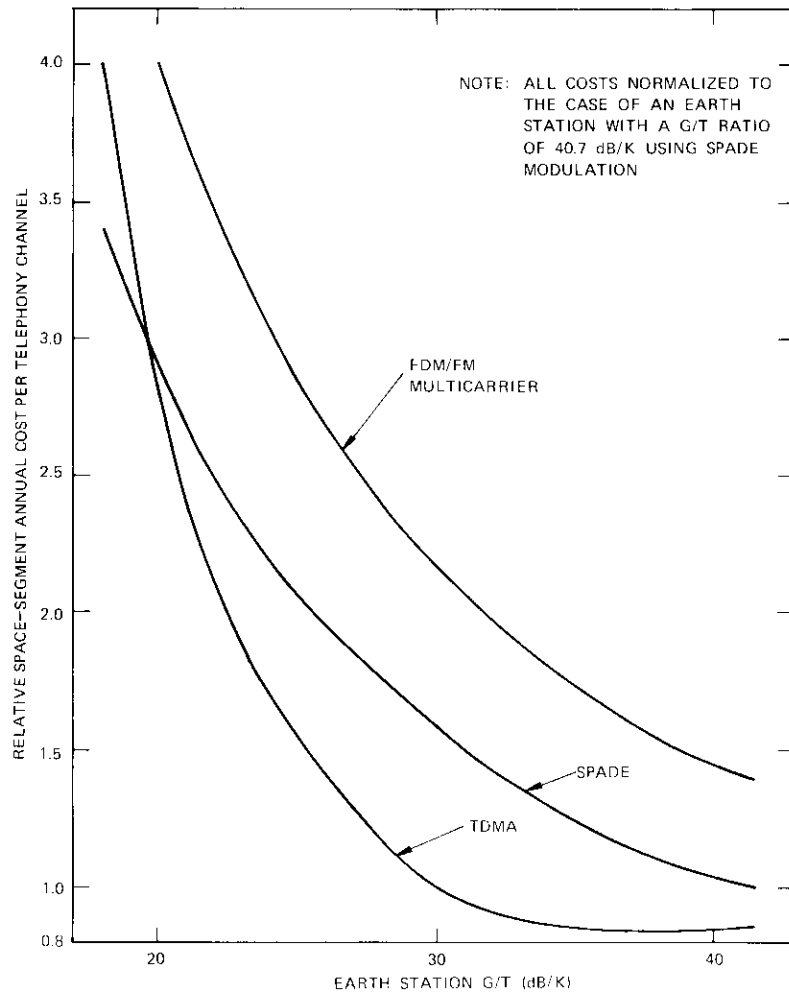


Figure 6. *Relative Space-Segment Cost, Spot-Beam Transponder*

Relative earth station costs

Figure 7 shows relative annual earth station costs as a function of earth station G/T. In this figure, it was attempted to provide earth station costs

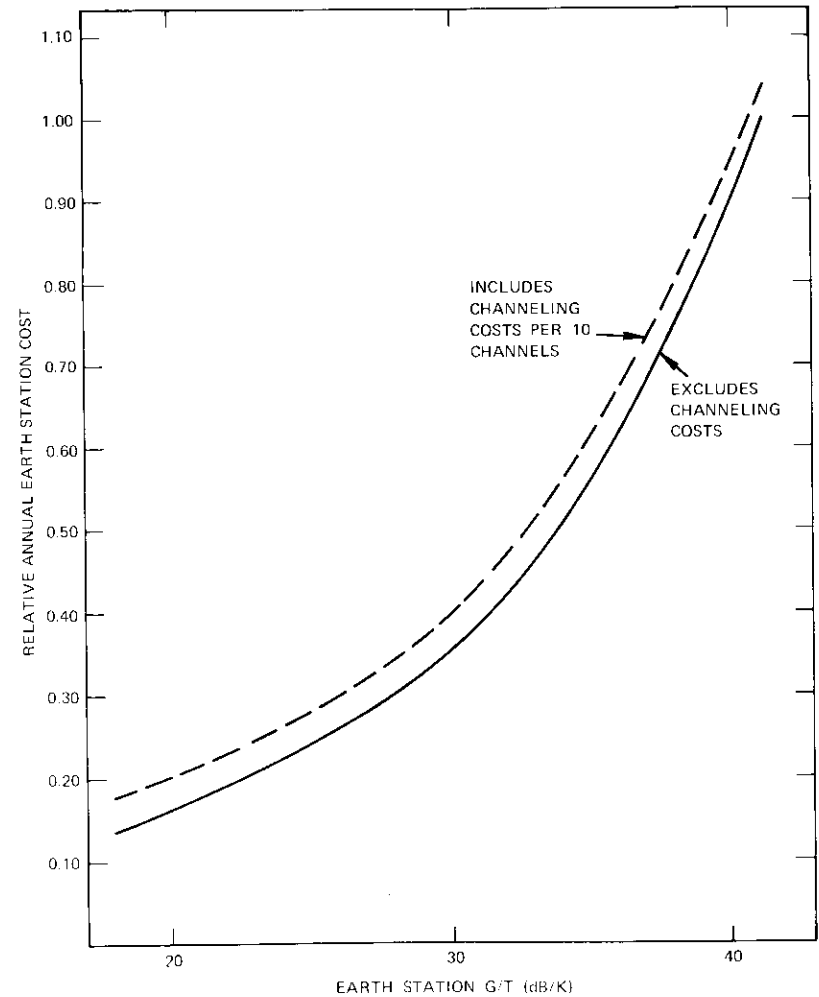


Figure 7. *Relative Earth Stations Cost Using SPADE*

applicable to several earth station sizes. Certain assumptions were used to arrive at consistent, comparable costs for various sizes. (For example, it was assumed that limited antenna tracking would be required, and that all stations would be procured in lots of 10.) The solid curve in Figure 7 represents basic station costs which do not vary as a function of the number of telephone channels handled. The broken line includes the incremental cost of adding 10 SPADE access channelizing units, and is shown for comparison purposes only.

Earth station G/T

In this section, the results of combining the previously discussed space-segment and earth station costs are analyzed. Figure 8 pertains to an entire global-beam transponder providing telephony service with SPADE access. Given a realizable transponder annual requirement, each curve represents the total cost allocation per earth station for a specified number of channels. All costs are normalized for an earth station which has a G/T of 40.7 dB/K and handles 40 channels. It can be seen that, as the average number of telephony channels per station decreases, the optimum G/T ratio also decreases. Figure 9, which pertains to spot-beam transponder operation, shows that the optimum G/T ratios are shifted to a significantly lower level.

Figures 8 and 9 also indicate the minimum G/T ratio necessary for adequate TV reception. The next section will discuss some of the implications of TV requirements on optimum G/T selection.

Other considerations in optimum G/T selection

The exact earth station G/T ratio is primarily determined by the type of service to be provided, i.e., telephony only, or telephony and television. As shown previously, the provision of telephony channels does not have a decisive effect on the optimum G/T ratio, whereas the provision of TV-quality channels will place a lower limit on the earth station G/T ratio.

Television quality

One of the most important parameters of a television channel is the signal-to-random-noise ratio. In a communications satellite link, the carrier power received from the satellite influences the ultimate TV signal-to-noise ratio which can be obtained. Since this received power is a

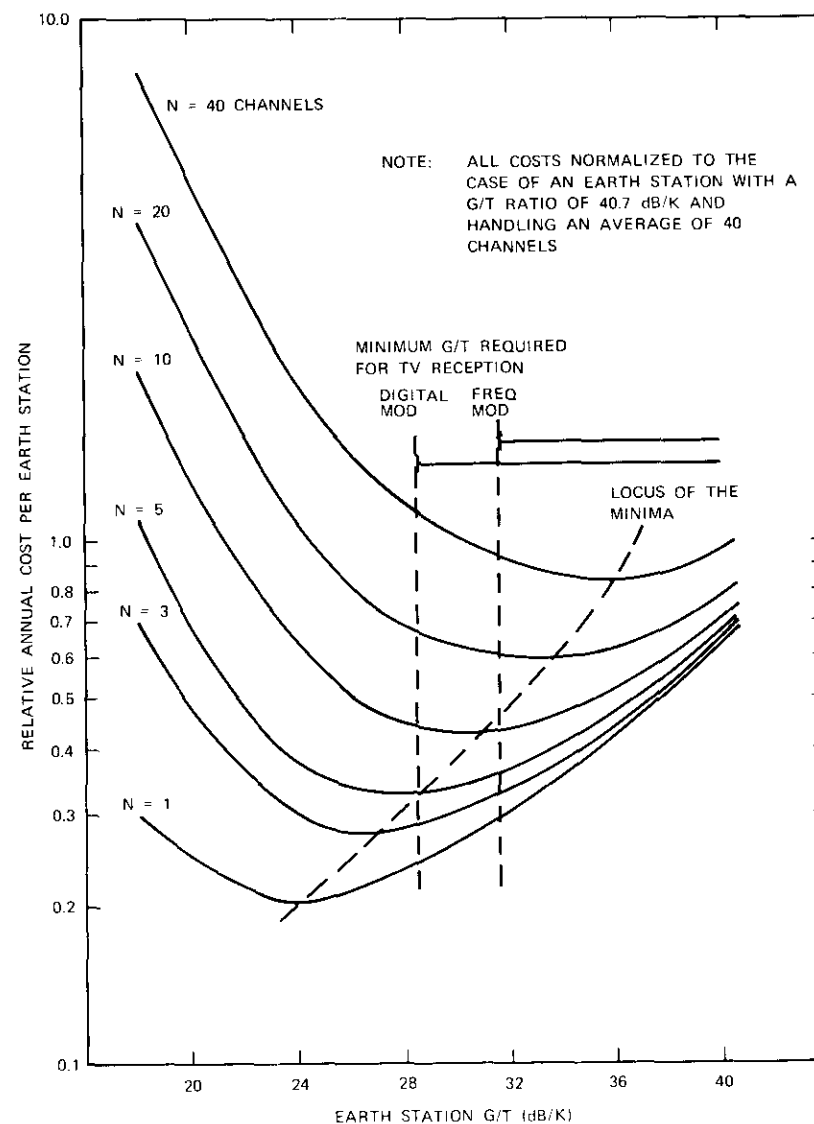


Figure 8. Global-Beam Transponder, SPADE Access

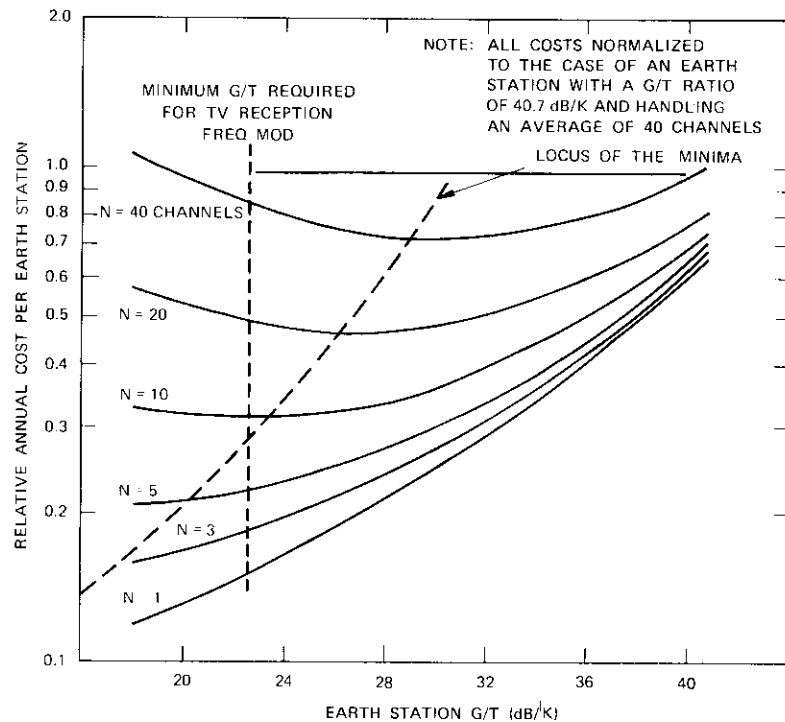


Figure 9. Spot-Beam Transponder, SPADE Access

function of the power radiated from the satellite, the receive earth station's antenna gain (size and efficiency), and the noise temperature, the total system cost is related to the signal-to-random-noise requirement. It is therefore essential to stipulate the signal-to-random-noise objective of the television channel in terms of the overall end-to-end user requirements.

The subjective effect of additive random noise on television picture quality has been well documented. In general, the television picture quality is less affected by high-frequency noise than by low-frequency noise. Although this statement is essentially true for both color and monochrome pictures, it must be modified somewhat for color because the color information is transmitted toward the upper end of the television spectrum. Since the random noise which is picked up on various types of transmission systems, e.g., coaxial cables, radio links, and broadcast receivers, does not have the same spectral distribution, it is necessary to normalize the noise spectra so that their subjective effects on picture quality can be

readily compared. This normalization or weighting of the various noise spectra varies with the television system and the type of signals (monochrome or color) being transmitted.

Work by Barstow and Christopher [3] suggests that weighted* additive random noise is "just perceptible" to the "median observer" at a level of -50 dB, as defined previously. Other subjective tests [4] that have been conducted in a comparable manner indicate that a picture having this same level of noise would have been given an "excellent" quality rating by about 90 percent of the observers. Comparable results have also been demonstrated in other tests [5]-[7]. A close examination of the results of these latter two tests indicates that the -50 -dB weighted random noise level is at or near the visual threshold of most observers.

In any television distribution system that may include a communications satellite link, there are a number of other sources of noise that significantly affect the ultimate picture quality. These are evaluated in Table 1.

TABLE 1. NOISE SOURCES IN A TELEVISION DISTRIBUTION LINK

	Noise Below Reference Level (dB)
Radio-Relay System (<1,609.3 km or <1,000 mi. long with one intermediate demodulation/modulation point)	≈ 57
Local Video Cable Links ($\leq 16,093$ m or ≤ 10 mi. long)	≈ 57
Public Broadcast Transmitter	≈ 54
Broadcast-Quality Videotape Recorders	≈ 51

Since the sources of noise listed in Table 1 will be encountered on most national television distribution systems, a reasonable requirement for a communications satellite link forming the backbone might be a signal-to-noise ratio of 50 dB. Such a requirement would ensure a satisfactory quality of service to most viewers.

Selection of specific G/T ratios

In this study, to perform system tradeoffs, it has been assumed that the earth station G/T is a continuous function. In reality, however, this ratio

* See C.C.I.R. rec. 421-2 [8] for typical weighting characteristics.

is in the form of a step function; i.e., any antenna size may be associated with either a "cooled" or "uncooled" low-noise receiver (LNR). In addition, antennas are normally produced in incremental step sizes, i.e., with diameters of 2.4, 4.9, 9.7, 12.8, or 18.3 m (8, 16, 32, 42, or 60 ft). Thus, the actual G/T values as functions of cost will fall about the assumed continuous line function.

A further consideration is that the same antenna is used for both transmitting and receiving. Therefore, while a specific G/T selected for use with a given antenna size may be quite acceptable for receiving, the transmit gain may be too low, resulting in an inordinately large HPA requirement. Increasing the antenna diameter will, of course, benefit both the transmit and receive capability, but the cost will rise rapidly as the diameter is increased. In addition, the antenna beamwidth becomes narrower with increasing diameter, thus introducing more stringent tracking requirements.

As noted in the previous paragraphs, the total costs of telephony transmission are not very sensitive to variations in G/T. Hence, it can be concluded that TV quality considerations and earth station design factors will determine the choice of G/T. Further, from the preceding discussion it has been shown that a TV quality corresponding to a signal-to-noise ratio of approximately 50 dB (peak-to-peak luminance to weighted rms noise) represents a good tradeoff between quality and cost.

A TV signal corresponding to $S/N \approx 50$ dB can be obtained through a global-beam transponder by using regular FM transmission with a G/T of approximately 31.7 dB/K. In addition, this G/T value is satisfactory for other applications, as shown in Table 2.

Transmission through a spot-beam transponder provides this same TV quality with a G/T of approximately 20.7 dB/K. However, it has been assumed that such small earth stations may also wish to transmit one or more telephony channels and, to limit the HPA power requirements, a somewhat larger antenna is desirable. For this reason, a G/T of 22.7 dB/K has been selected for the smaller antenna size. This value is also satisfactory for other transmissions, as shown in Table 2.

Earth station design considerations

The two G/T values selected in the preceding paragraphs and the transmitted power are the principal parameters which determine earth station configurations. The relative values of these parameters will now be examined in terms of antenna tracking, low-noise receiver, and power

TABLE 2. TRANSMISSION CAPABILITIES WITH SELECTED G/T RATIOS

a. TV Transmission				
Transmission	Earth Station G/T			
	31.7 dB/K		22.7 dB/K	
	Number of TV Channels	S/N (dB)	Number of TV Channels	S/N (dB)
FM TV				
Global-Beam INTELSAT IV Transponder	1	≈ 50	—	—
Spot-Beam INTELSAT IV Transponder	2	≈ 50	1	≈ 52
Compressed Digital TV				
Global-Beam INTELSAT IV Transponder	1	≈ 56	—	—
Spot-Beam INTELSAT IV Transponder	2	≈ 56	1	≈ 56
b. Telephony Transmission				
Transmission	Earth Station G/T			
	31.7 dB/K		22.7 dB/K	
	Channels/Transponder			
SPADE, 4-Phase PCM/PSK, Optimum Coding				
Global-Beam INTELSAT IV Transponder	400		80	
Spot-Beam INTELSAT IV Transponder	800		400	
FDM/FM				
Single Carrier				
Global-Beam INTELSAT IV Transponder	540		72	
Spot-Beam INTELSAT IV Transponder	1,400		800	
Multicarrier				
Global-Beam INTELSAT IV Transponder	240		48	
Spot-Beam INTELSAT IV Transponder	600		360	
TDMA, 4-Phase PCM/PSK, Optimum Coding				
Global-Beam INTELSAT IV Transponder	300		—	
Spot-Beam INTELSAT IV Transponder	1,400		480	

amplifier requirements. The choice of these three major items is assumed to be similar for all other subsystems.

Earth station G/T

For a receive-only station, the only parameter to be considered is G/T. If, however, telephony transmission is to be provided, the earth station e.i.r.p. must be specified. Since this parameter is related to antenna gain, the three parameters (G, T, and transmit power, P) must be apportioned to achieve a minimum cost. Other factors such as reliability objectives, ease of installation, and maintenance costs, particularly in remote areas, are not analyzed here.

There are two basic choices of system noise temperature for a station with a G/T of 31.7 dB/K; a temperature of 73K may be obtained with a 20K cryogenically cooled LNR, and a temperature of 130K may be obtained with an uncooled LNR. For these LNRs, the antenna sizes required to achieve a G/T of 31.7 dB/K are approximately 9.7 and 12.8 m (32 and 42 ft), respectively. If cost is the only determining factor, the 9.7-m (32-ft) cooled combination would be chosen. If, however, improved reliability, reduced maintenance, and a smaller HPA are desired, the 12.8-m uncooled LNR is still a prime contender.

Table 3 lists the parameters required to produce G/T values spanning the range of interest for three antenna sizes with cooled and uncooled receivers. For all three antennas, beam steering is assumed to accommodate a satellite stationkeeping uncertainty of $\pm 1^\circ$ with a communications penalty of no more than 0.5 dB. It should be possible to reduce this uncertainty and eliminate beam steering, particularly for the 4.9-m antenna, through increased experience with INTELSAT IV. In general it is expected that an uncooled receiver will be used for the 22.7-dB/K station, while a cooled receiver with a 9.7-m-diameter antenna will be used for the 31.7-dB/K station.

Earth station HPA

Channel capacity calculations show that the earth terminal e.i.r.p. must be at least 57 and 68.5 dBW/channel for systems having G/T ratios of 31.7 and 22.7 dB/K, respectively. The latter e.i.r.p., which is required for a satellite on gain step 1, reflects the gain limitations of the satellite rather than the need for balanced up- and down-links. Consequently, a large earth terminal power penalty is necessary to compensate for this satellite gain deficiency, and a disproportionately large HPA is required unless the number of channels is restricted to a low value, e.g.,

TABLE 3. COOLED AND UNCOOLED LNR SYSTEMS

a. Antenna and Cooled LNR

Parameter	Antenna Diameter (m)		
	4.9	9.7	12.8
Antenna Gain at 70% Efficiency at 3.95 GHz (dB)	44	50.5	53
Antenna 3-dB Beamwidth (deg)	1.15	0.54	0.42
Antenna Steering Accuracy for 0.5-dB Down-Link Loss (deg)	0.42	0.22	0.17
$T_{\text{feed}} + T_{\text{antenna}}$ (K)	56	53	50
T_{LNR} (K)	20	20	20
T_{system} (K)	76	73	70
(dB)	18.8	18.6	18.4
Cooled G/T (dB/K)	25.2	31.9	34.6

b. Antenna and Uncooled LNR

Parameter	Antenna Diameter (m)		
	4.9	9.7	12.8
T_{LNR} (K)	80	80	80
T_{system} (K)	136	133	130
(dB)	21.3	21.2	21.1
Uncooled G/T (dB/K)	22.7	29.3	31.9

five or less. It is assumed that an HPA output backoff of 3 dB will be sufficient to meet the reduced up-link intermodulation requirements.

Earth station tracking considerations

As the antenna diameter decreases, the antenna beamwidth increases. Hence, it is desirable to determine the earth station size for which fixed antennas without tracking or steering capability can be employed. To permit fixed antenna pointing, it is necessary to ensure that satellites are maintained within the earth station antenna beamwidths and that the direction remains stable with time.

The INTELSAT IV satellite requirements state that the satellite must be capable of being maintained in an orbital position of $\pm 0.5^\circ$ in longitude

and latitude for a period in excess of seven years. A 9.7-m antenna has a half-power beamwidth of 0.36° at 6 GHz. With proper design, earth station antenna pointing errors caused by wind and ice loading and diameter variations are not expected to exceed 0.07° . Hence, an INTELSAT IV satellite will have to be controlled to within $\pm 0.1^\circ$ to employ fixed antenna pointing. Also, a power margin will have to be reserved for pointing errors.

To provide specialized communications services through INTELSAT satellites, it may become necessary over a period of time to change from one satellite position to another for operational or other reasons. Therefore, small antennas planned at this time must be provided with some steering capability. However, after some initial experience with several INTELSAT IV satellites, it may be possible to employ fixed antennas. Even then, it will be necessary to provide for the readjustment of earth station antenna pointing directions in case of service transition to a different satellite or intentional repositioning of the operating satellite.

It is expected that most earth stations will have to be planned for at least limited tracking, in the form of feed or antenna steering, with either a simple autotracking system or a simple program tracking scheme. In addition, it will be necessary to provide for a change in pointing direction to a different satellite.

Possible system configuration

The following is a general description of a possible system configuration [9]. Although actual systems will probably differ in specific details, the concept will undoubtedly be similar.

Figure 10 is a "baseline" configuration for a system using a global-beam transponder for telephony and television services. This arrangement would permit an international service earth station which is already accessing an INTELSAT IV satellite to function also as the major terminal of a domestic or regional system. This scheme would not interfere with the station's international service operation and would result in substantial benefits through the consolidation of facilities. A number of earth stations with smaller diameters and G/T values commensurate with the services to be provided would be utilized at the other sites of the network. If the existing INTELSAT earth station could not be utilized for this service, a separate station would have to be provided.

This basic configuration would provide one television channel from the central terminal to all stations, and a number of duplex telecommunications channels between all stations in the network. (The latter number

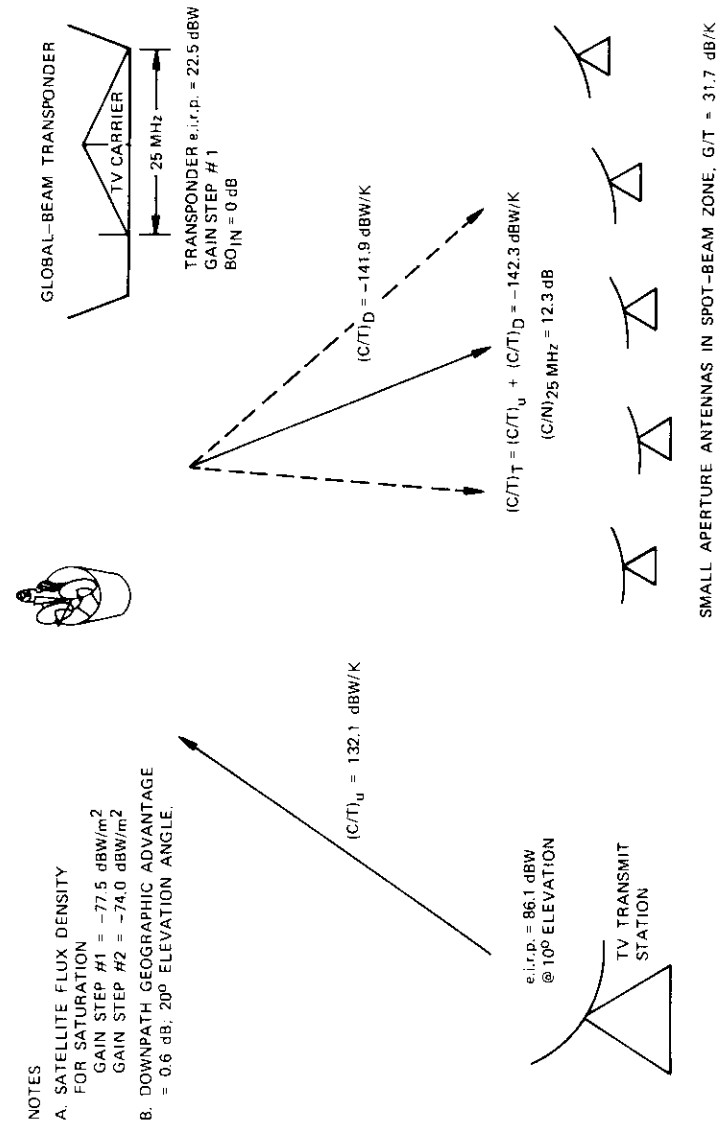


Figure 10. Global-Beam Operation

would depend on traffic requirements.) It is assumed that TV would be transmitted from the large earth station and that only TV receive capability would be provided at the smaller stations, which could nevertheless be provided with telephony transmit and receive equipment. However, the use of permanent or mobile facilities would permit television transmit capability to be provided at any of the other earth station terminals.

This baseline configuration could be expanded by adding earth stations as new service areas are brought into the system. The individual earth stations could be configured so that their circuit capacity could be expanded to fulfill increased traffic demands with minimum dislocation of service. TV capability could also be expanded as required.

Telephony transmission in the system could be provided in two modes. On major paths between designated primary centers, full-time preassigned channels could be provided. In addition, a system of demand-assigned channels could be provided. Since all stations would have access to these channels, full interconnection among all stations would be possible. This type of operation would allow for optimum utilization of the space segment. Full flexibility could also be provided so that channels could be rearranged between stations and between preassignment and demand-assignment modes according to traffic demands.

A possible spot-beam configuration is shown in Figure 11. It could provide the same services as the global-beam configuration. In addition, the use of the full power of the spot-beam transponder would permit an earth station with a G/T of 22.7 dB/K to receive a TV signal and provide telephony service. Alternatively, if a 31.7-dB/K earth station were utilized, only half the power and bandwidth of a transponder would be required for TV service.

Earth station configuration

To date, a number of small earth stations have been utilized successfully for satellite communications purposes, usually to perform specific task assignments. In the following paragraphs, the concept of a simplified earth station system that could be implemented in the near future will be presented. This system has been specifically designed to meet the requirements of a domestic or regional system. Figure 12 is a block diagram showing the principal subsystems of this configuration.

For a domestic or regional system, there is no need for hemispheric coverage or even for autotrack in the sense of using the received signal for steering. Instead, an adequate antenna configuration will use a fixed re-

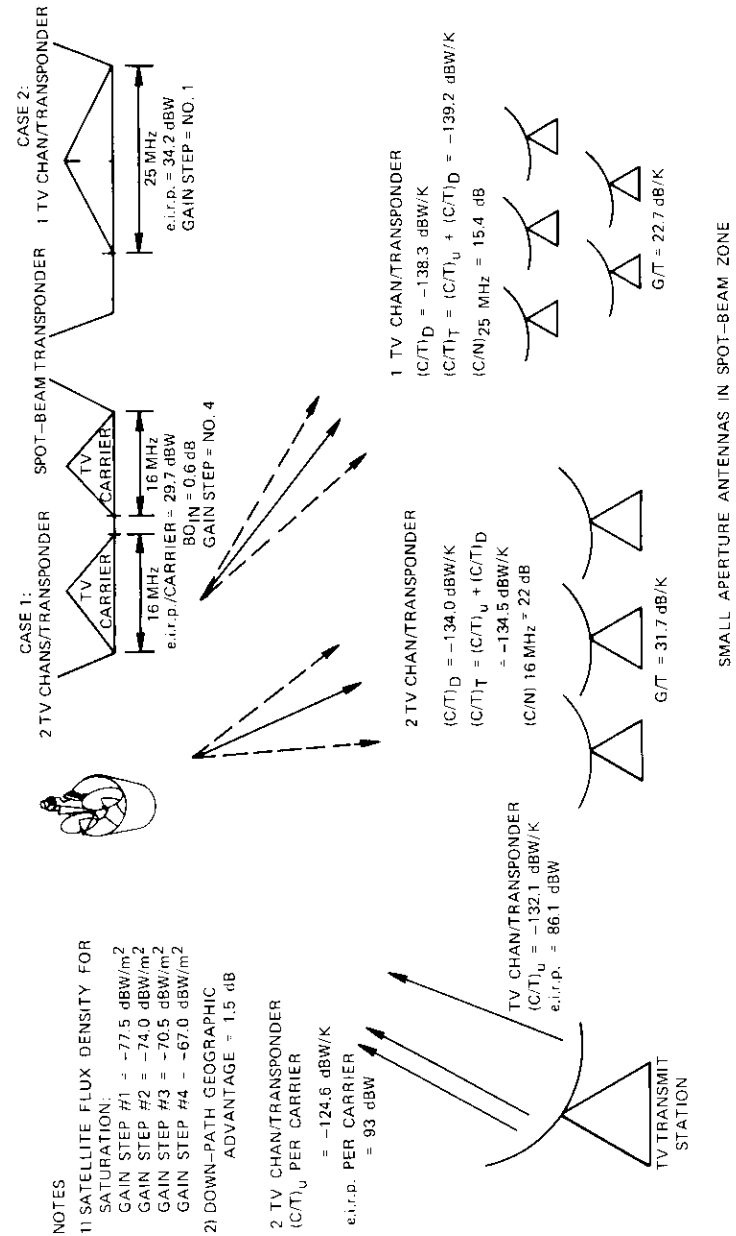


Figure 11. Spot-Beam Operation

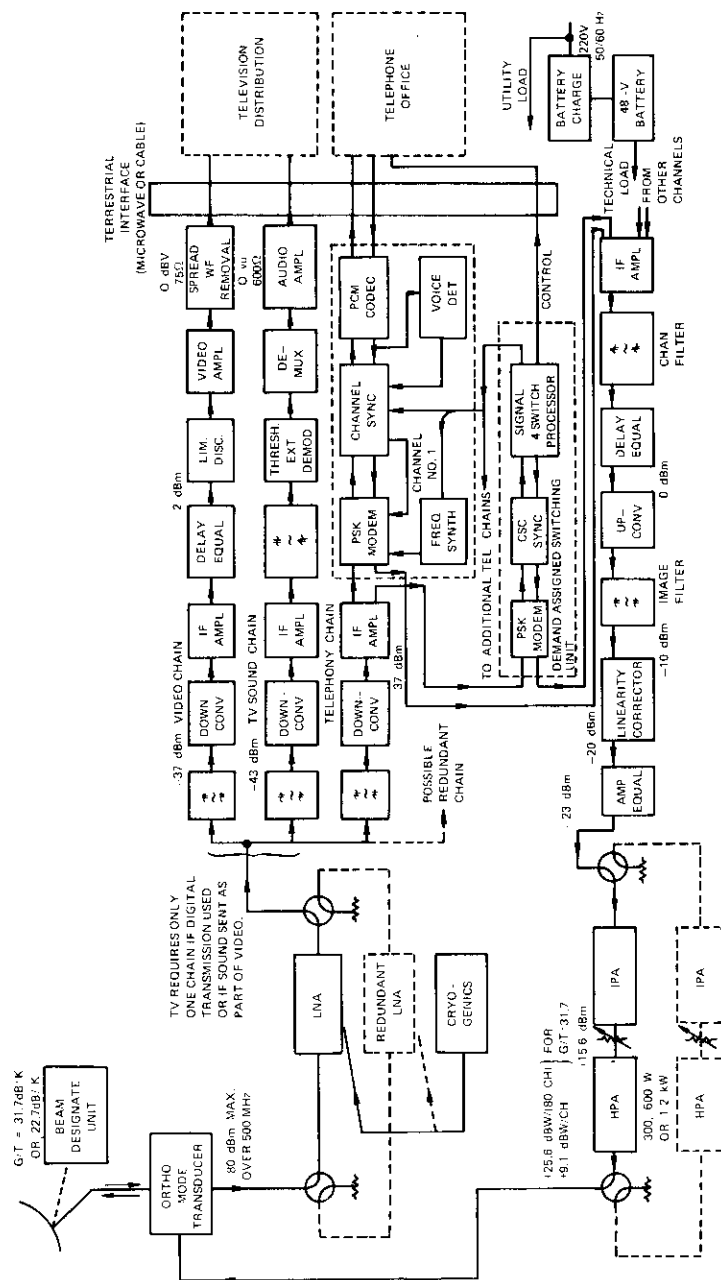


Figure 12. Typical Earth Station Block Diagram

flector and a steerable feed. The reflector can be either a regular parabolic reflector or a parabolic torus with one dimension dictated by the maximum angular limits if two or more satellites are to be viewed. The feed motion will be sufficient to follow the satellite with no more than 0.5-dB pointing loss, and a second feed will be provided if switching to an alternate satellite is required.

Antenna size and its effect on the HPA and LNA have been discussed previously. This discussion indicated that, for stations having a G/T of 31.7 dB/K, the two most probable antenna sizes are 9.7 m for use with the cooled LNA and 12.8 m for use with the uncooled LNA. The degree of cooling or the noise temperature achieved with uncooled parametric amplifiers will determine whether intermediate antenna diameters can be used. For applications in which one antenna will be required to work with two or more satellites, a multiple-feed torus antenna can be advantageous (subject to satellite stationkeeping constraints).

For the 22.7-dB/K G/T requirement, a 4.9-m antenna used in connection with an uncooled parametric amplifier is considered to be a good solution. For low-noise receiver parametric amplifiers with 500 MHz of bandwidth, the following noise temperatures can be achieved:

- gaseous helium amplifier: $\sim 20K$
- uncooled parametric amplifier: $\sim 80K$

HPA requirements vary both as a function of transmit antenna gain and as a function of service requirements. For the proposed types of service, commercial TWTs, which are now available in sizes of 200 W, 300 W, 600 W, and 1.2 kW, are considered to be most suitable. All tubes are completely air cooled. A modified SPADE system and regular FDM/FM multiplexing equipment are considered to be most satisfactory for this type of service.

Monitor and test equipment is provided as required. For unattended stations it is desirable to provide automatic transmission of telemetry data concerning equipment operation so that a central monitor station can be alerted of any equipment failures. A moderate building shelter will be provided and, although the system is assumed to operate on commercially available power, backup power facilities will also be included.

Conclusions

The INTELSAT IV satellites provide highly reliable, high-performance, and economic service to small earth stations. Systems can be designed to provide both telephony and television services, depending on traffic distributions and requirements. Those factors that affect the selection of an optimum configuration in terms of performance and cost have been detailed, and representative values given.

The introduction of small earth stations can be expected to increase as telecommunications services via satellite expand with the introduction of new satellite systems. Since it is expected that only the largest users can afford to actually implement separate systems, smaller users are most likely to lease space-segment capacity. Detailed tradeoff analyses, as described in this paper, will ensure that the maximum utilization can be maintained over the lifetime of the system.

References

- [1] "The INTELSAT IV Communications System," edited by P. L. Bargellini, *COMSAT Technical Review*, Vol. 2, No. 2, Fall 1972, pp. 437-573.
- [2] E. R. Cacciamani, "The SPADE System as Applied to Data Communications and Small Earth Station Operation," *COMSAT Technical Review*, Vol. 1, No. 1, Fall 1971, pp. 171-182.
- [3] J. M. Barstow and H. N. Christopher, "The Measurement of Random Video Interference to Monochrome and Color Television Pictures," *AIEE Transactions*, Vol. 81, Pt. 1, No. 63, November 1962, pp. 313-320.
- [4] Television Allocations Study Organization (TASO), "Engineering Aspects of Television Allocations," TASO Report to the FCC, March 16, 1969.
- [5] W. K. E. Geddes, "The Relative Impairment Produced by Random Noise in 405-line and 625-line TV Pictures," *EBU Review, Part A-Technical*, Vol. XIV, No. 78, April 1963.
- [6] P. Mertz, "Data on Random Noise Requirements for Theatre TV," *Journal of the SMPTE*, Vol. 60, No. 8, August 1951.
- [7] "Transmission Systems for Communications," Bell Telephone Laboratories.
- [8] International Radio Consultative Committee (C.C.I.R.), "Requirements for the Transmission of Telephone Signals Over Long Distances (System I excepted)," Recommendation 421-22, *XIIth Plenary Assembly, New Delhi*, 1970, Vol. V, Pt. 2, pp. 173-193, Geneva: International Telecommunication Union, 1970.
- [9] B. I. Edelson, "Satellite Access: Small Earth Terminals," *AIAA 9th Annual Meeting and Technical Display*, Washington, D.C., January 8-10, 1973.

Jack L. Dicks received his B.S. degree in Mathematics and Engineering Physics from Sir George Williams College in Montreal, Canada. Before joining COMSAT, he was on the engineering staff of the Canadian Overseas Telecommunications Corporation, where he was involved in planning, installation, and testing of equipment associated with the CANTAT and COMPAC submarine telephone cables and the Mill Village earth station. Since he joined COMSAT in 1968, he has been primarily involved in transmission planning for the INTELSAT IV satellite system. He is presently Manager of the Systems Development Department in the International Systems Division.



Index: communications satellites, Intelsat IV, ship antennas, pulse communications.

An experimental ship-shore satellite communications demonstration

J. KAISER

(Manuscript received October 2, 1973)

Abstract

In the spring of 1972, the Communications Satellite Corporation and Cunard Lines Ltd. jointly sponsored an experiment in satellite communications between the Cunard ship *RMS Queen Elizabeth 2* and a small earth station at COMSAT Laboratories in Clarksburg, Maryland, via the INTELSAT IV F-3 satellite over the Atlantic Ocean.

The ship carried an 8-ft (2.4-m) parabolic antenna, while the small earth station had a 15-ft (4.5-m) antenna. Both locations used DICOM (digital communications) units providing one 28-kbps delta modulated encoded voice channel. The shipboard antenna was gyro-stabilized against ship motions by using a simple open-loop system without satellite tracking signals.

Introduction

This paper describes the results of a program which used an INTELSAT IV spacecraft and a fairly simple shipboard terminal to demonstrate the feasibility of establishing a good-quality voice link between a U.S. earth terminal and a commercial ship operating on Atlantic routes. This project was suggested by Col. J. D. Parker, Secretary General of the Comité International Radio-Maritime (CIRM), to explore the feasibility of ship-shore communications via satellite.

The experiment showed that it is feasible to place an antenna with fairly high gain on board a ship in commercial service and to point it toward a geostationary satellite by using a simple open-loop pointing system with gyro stabilization. Acquisition of the satellite and subsequent manual repositioning of the antenna were easily accomplished by the operators. The need for antenna repointing at intervals of one-half to one and one-half hours was acceptable for the experiment.

All test participants judged that the quality of the link between ship and shore was very good. The communications tests were significant because they demonstrated that a link, including all of the necessary echo suppressors, could be established between the ship's normal telephone system (2-wire service) and the U.S. and U.K. terrestrial networks via an INTELSAT satellite. The demonstration included a variety of acoustically coupled communications devices: facsimile, teletype, biomedical data unit, and computer access. All of these modes of communication were demonstrated with good results.

There was no interference from the satellite terminal to any of the ship's electronic equipment, but there was some interference from the ship's 1,500-W high-frequency transmitter to the satellite received signal when the high-frequency transmitter was tuned to 12.459 MHz. Other frequencies caused no appreciable interference.

Whereas the roll and pitch of the *Queen Elizabeth 2* (QE 2) may not have been representative of the motion of smaller ships, the winds and weather encountered during the tests were quite significant.

A number of earlier experiments for ship-shore communications were conducted via ATS satellites. However, these experiments used low-gain broad-beam antennas [1].

A successful experiment at C-band (4-6 GHz) would indicate a possible implementation in the less stringent pointing environment of the L-band frequencies (1.5 GHz) recently established for maritime satellite communications [2].

Spacecraft configuration

The experiment utilized the INTELSAT IV F-3 satellite over the Atlantic Ocean. Two transponders in that spacecraft were used for the tests: a global-beam transponder (#12) for the link from COMSAT Laboratories to the ship, and a spot-beam transponder (#3) for the link from the ship to the Laboratories.

Two transponders were used to conserve transmitter power on the ship

terminal. That is, the link to the ship required a transponder in the global-beam configuration to cover the expected geographic range of the ship during the experiment. The same global-beam transponder could have been used for the link to the Laboratories terminal; however, the required RF transmitter power at the ship (approximately 120 W at the antenna feed) could be obtained only by using a transmitter with a 250- to 300-W rating. It was deemed desirable to keep the ship transmitter power low to reduce the possibility of interference and of hazards to personnel. Thus, for the experiment, transponder #3 in the spot-beam configuration was used for the ship-to-Laboratories link. This permitted a ship station transmitted power requirement of about 8 W. If the fixed station had been a standard earth terminal with a G/T of 40.7 dB/K, then a single transponder, connected to the global beam, could have been used for both links.

Shipboard terminal

The ship terminal consisted of the following major elements:

- a. an 8-ft (2.4-m) parabolic dish antenna with servo-controlled pedestal and low-noise receiver (for the antenna control system, see Figure 1);
- b. an antenna drive bay;
- c. a DICOM terminal RF transmitter bay [3], [4];
- d. an 8- × 12-ft (2.4- × 3.7-m) equipment enclosure with air conditioner on the sports deck (covered, but not normally heated or cooled);
- e. test equipment;
- f. peripheral equipment.

Figures 1 and 2 are block diagrams of the shipboard terminal system. (The installation of the terminal on the QE 2 will be shown in Figure 8.)

Comsat Laboratories terminal

The terminal at COMSAT Laboratories in Clarksburg, Maryland, included the following major equipment:

- a. a 15-ft (4.5-m) parabolic dish antenna with low-noise receiver (hand-operated pointing);
- b. DICOM channel equipment;
- c. a transmitter bay;
- d. peripheral equipment.

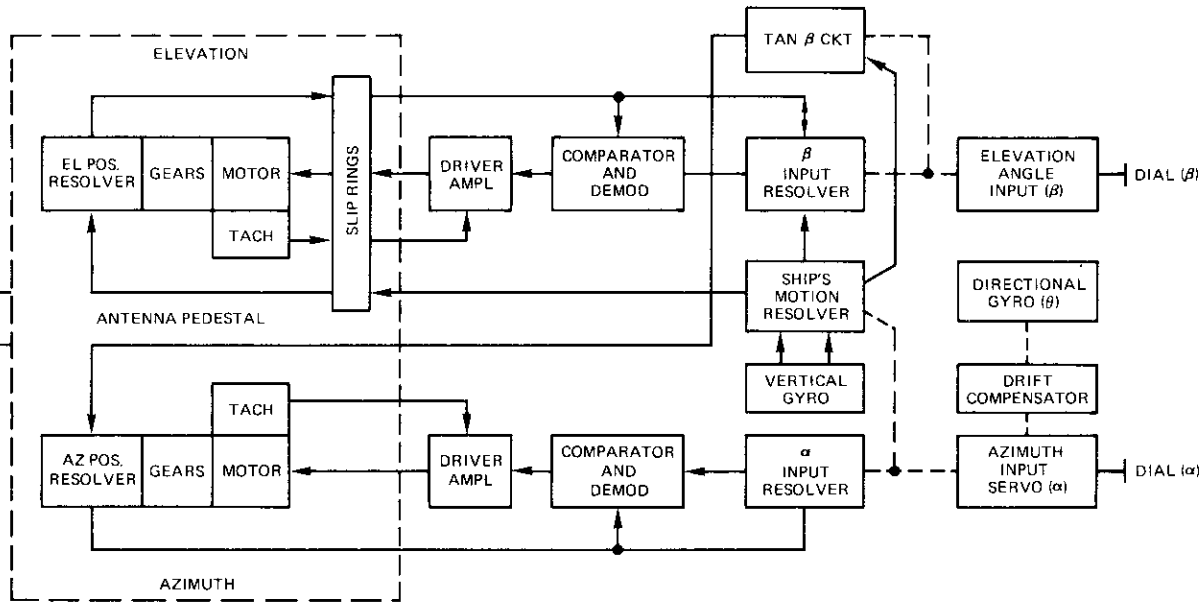


Figure 1. Shipboard Antenna Control and Stabilization

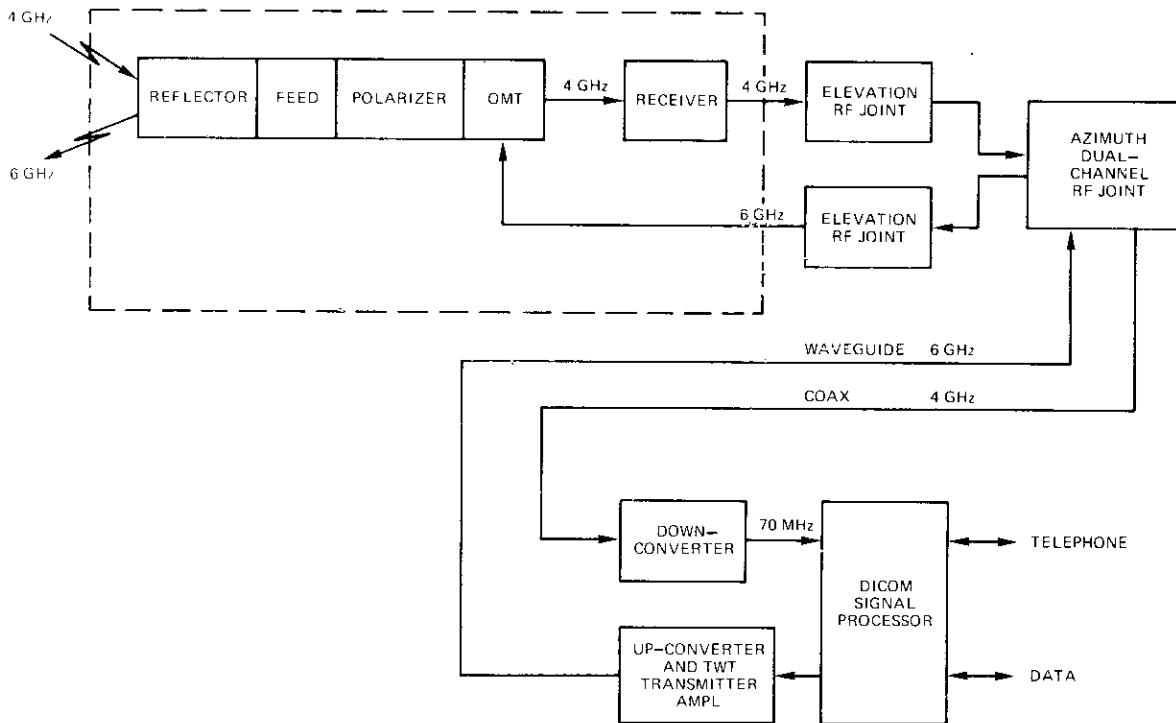


Figure 2. Shipboard Terminal Communications and RF Equipment

Terminal performance

Performance characteristics of the terminal at COMSAT Laboratories and the terminal onboard the QE 2 are listed in Table 1.

Link budget calculations

The link budget calculations are summarized in Table 2. Both terminals were limited in transmitted power, resulting in small margins for each end of the link. The margins used for the calculations in Table 2 include the expected pointing errors of the ship station, i.e., the nominal value of the ship station antenna beam at the 3-dB point.

Communications equipment

For the shipboard experiment, the communications equipment consisted of digital transmission equipment using PSK modulation, delta modulation, and convolutional encoding [3], [4]. The 2-phase modulated carrier occupied 80 kHz of RF bandwidth. Carrier-to-noise values of 4.8 dB were required for a bit-error probability of 10^{-4} . The performance of the DICOM channel units, described in References 3 and 4, had been verified prior to the experiment by using a satellite link (INTELSAT IV F-2). Error rate measurements taken during the experiment agreed with these earlier results. A more detailed description of the communications equipment is given in Reference 5.

System test schedule

The antenna and electronics were placed onboard the QE 2 by helicopter while the ship was debarking passengers at Norfolk, Virginia, on 9 March 1972. During the test (10 March 1972 to 15 May 1972), the QE 2 made four trips between New York and the Caribbean, a transatlantic crossing, a Mediterranean cruise, and finally another transatlantic crossing from Southampton to New York. During this period the ship encountered three storms, including one of the worst storms in the Atlantic for many years (16-19 April 1972). Weather conditions varied from a snowstorm on 11 March while departing from New York to 90°F temperatures while anchored off La Guaira. Thus, the system was exposed to a wide variety of geographic locations and weather conditions.

Figures 3 and 4 show the routes taken by the QE 2 in the Caribbean, the Atlantic, and the Mediterranean. The elevation angle of the antenna referenced to earth coordinates ranged from 53° to 19° during the voyages.

TABLE 1. TERMINAL PERFORMANCE CHARACTERISTICS

a. Shipboard Terminal	
Transmit	
Frequency	6,040.0 MHz
Transmit Power at Feed, 8 W	9.0 dBW
Transmit Gain (peak of beam)	40.0 dB
Peak e.i.r.p.	49.0 dBW
Pointing Error Allowance*	3.0 dB ($\pm 0.75^\circ$)
Nominal e.i.r.p.	46.0 dBW
Receive	
Frequency	4,189.6 MHz
System Noise Temperature	300 K
Receive Gain	37.0 dB
Peak G/T	12.2 dBW/K
Pointing Error Allowance	2.0 dB ($\pm 0.75^\circ$)
Nominal G/T	10.2 dB/K
b. COMSAT Labs Terminal	
Transmit	
Frequency	6,414.5 MHz
Transmit Power at Feed, 250 W	24.0 dBW
Transmit Gain	46.0 dB
e.i.r.p.	70.0 dBW
Receive	
Frequency	3,815.0 MHz
System Noise Temperature	141 K
Receive Gain	43.0 dB
G/T	21.5 dB/K

*The pointing error allowance was derived from the antenna pattern and the expected servo pointing accuracies which will be discussed in the next section.

The antenna pointing angle with respect to the ship's bow varied as a function of the ship's heading and traversed all values.

Antenna repositioning

The pointing system is formed by establishing a stable platform comprising the antenna reflector and feed system, which is then manually pointed in the direction of the satellite. Theoretically, the ship's motions (roll, yaw, and pitch) do not affect the stabilized antenna, which will

TABLE 2. LINK BUDGET CALCULATIONS

Channel Transmission Characteristics	
Modulation and Coding	28-kbps Delta modulated voice, rate 1/2 convolutional coding, 2-phase CPSK
C/N at $P_{BE} = 1 \times 10^{-4}$	4.8 dB
C/T Required for $P_{BE} = 1 \times 10^{-4}$	-174.0 dBW/K
Satellite Parameters	
G/T	-16.0 dB/K
e.i.r.p.	
Global Beam	23.2 dBW
Spot Beam	35.0 dBW
W_s (gain step 1)	-77.2 dBW/m ²
Labs-to-Ship Parameters	
C/T Required	-174.0 dBW/K
Path Loss	196.0 dB
	22.0 dBW/K
Ship Terminal G/T (nominal)	10.2 dB
Satellite e.i.r.p. Required	11.8 dBW
Labs Station e.i.r.p. Required	69.0 dBW
Labs Station e.i.r.p. Available	70.0 dBW
Margin	1.0 dB
Ship-to-Labs Link Parameters	
C/T Required	-174.0 dBW/K
Path Loss	196.7 dB
	22.7 dBW/K
Labs Station G/T	21.2 dBW/K
Satellite e.i.r.p. Required	1.5 dBW
Ship Station e.i.r.p. Required	45.4 dBW
Ship Station e.i.r.p. Available (nominal)	46.0 dBW
Margin	0.6 dB

remain pointed toward the satellite despite the ship's angular motions. The ship's translational motions, i.e., its normal travels from one place to another, require changes in the line of sight to the satellite, and hence a manual adjustment of the antenna pointing angles. The pointing system is an open-loop system since no signals received from the satellite are used for automatic antenna pointing.

Antenna stabilization was accomplished by using two gyros, one vertical

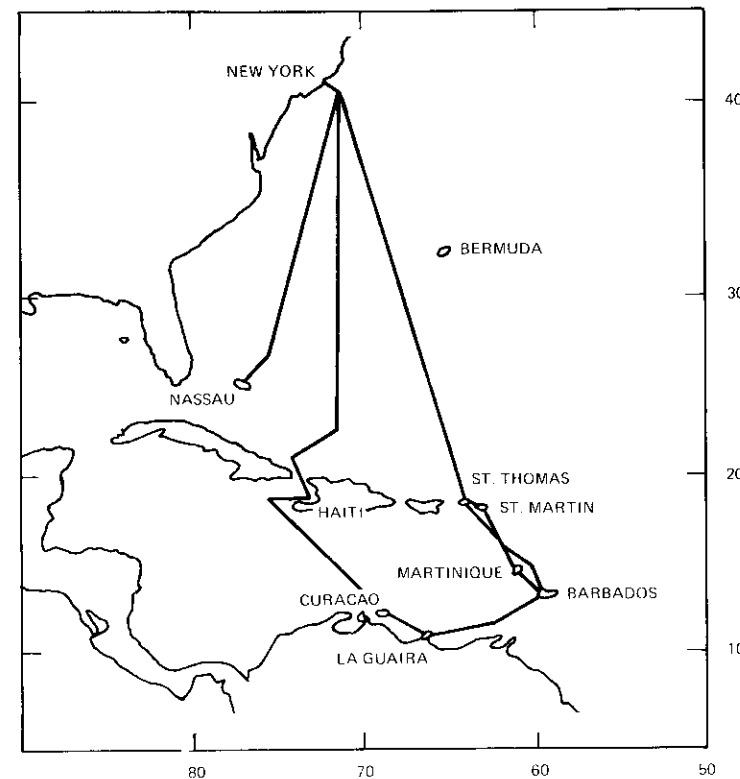


Figure 3. QE 2 Caribbean Cruises, 11 March-16 April 1972

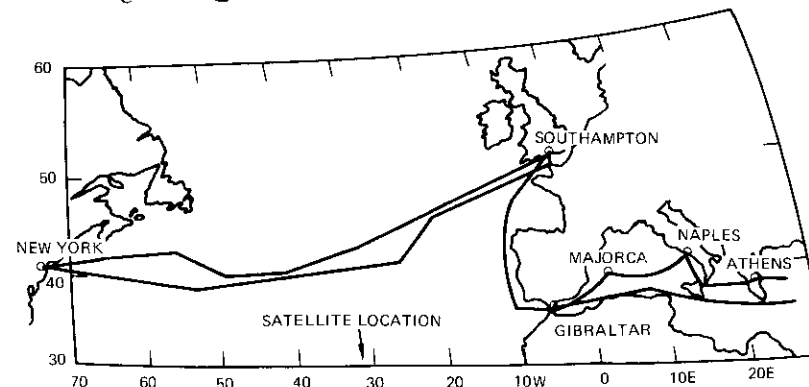


Figure 4. QE 2 Transatlantic and Mediterranean Cruises, 16 April-15 May 1972

gyro measuring pitch and roll, and one directional gyro measuring the ship's yaw or heading deviations. The gyro differs from the ship's gyro-compass in that it does not measure azimuth directly. The vertical gyro is essentially free of drift, while the directional gyro has two components of drift. One is a random drift term of about $2^\circ/\text{hr}$; the other is a drift related to the rotation of the earth given by $15^\circ/\text{hr} \times \sin L$, where L is the geographic latitude of the current ship's position. Both of these terms contributed to the gyro drift problems encountered during the experiment so that fairly frequent manual antenna repointing was required.

To be used in driving the antenna servos, the measured gyro reference angles must be resolved into the appropriate antenna pedestal angles (elevation over azimuth). This was accomplished by means of electrical resolvers (400 Hz) mounted on instrument servo-driven antenna control axes. These servos were, in turn, controlled by means of the azimuth and elevation control dials.

For this experiment, the gyro angles were resolved into the antenna coordinates by using simplifications which caused some errors when the ship's angular motions became large. The complete control equations for an elevation over azimuth antenna mount are found in Reference 6. These equations were simplified by using small angle approximations for the pitch and roll excursions. The resulting control equations are

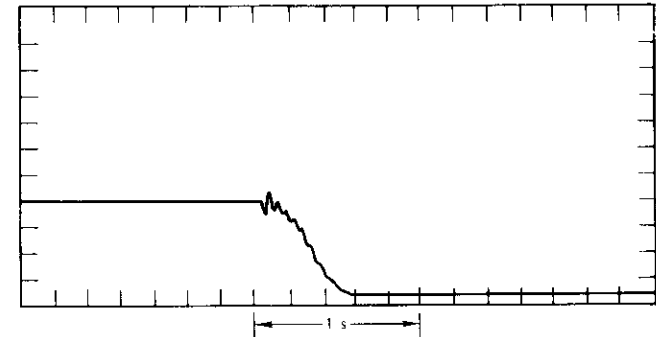
$$\begin{aligned}\alpha &= \alpha'' + \theta \\ \alpha' &= \alpha + \tan(b) [R \cos(a) + P \sin(a)] \\ \beta' &= \beta + [-R \sin(a) + P \cos(a)]\end{aligned}$$

where

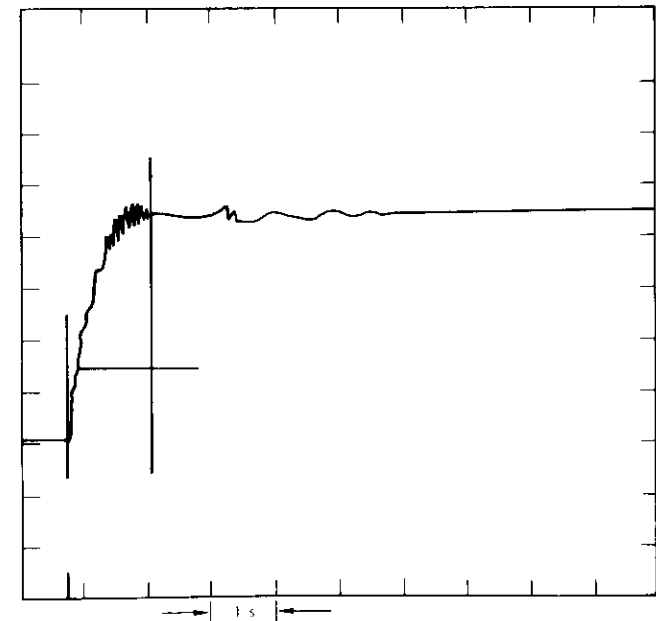
- α = antenna azimuth angle setting relative to the ship
- α' = antenna azimuth axis angle in deck coordinates
- α'' = azimuth angle to the satellite
- β = antenna elevation angle to the satellite
- β' = antenna elevation axis angle
- R = roll gyro output
- P = pitch gyro output
- θ = directional gyro output.

These relationships are accurate only for small excursions of the roll and pitch motions, i.e., roll, R , less than $\pm 10^\circ$ and pitch, P , less than $\pm 5^\circ$. An analysis made prior to the experiment showed that simplification of the resolution would result in dynamic mispointing of no more than $\pm 0.25^\circ$ for the expected pitch and roll conditions. The implementation of these equations has been shown in Figure 1.

The major source of dynamic antenna mispointing in this system is a function of the antenna servo dynamic response. The servo response curves shown in Figure 5 indicate that during large ship motions the servos will have a maximum dynamic lag of about 0.5° .



a. ELEVATION SERVO RESPONSE
2° STEP, 25mm/s



b. AZIMUTH SERVO RESPONSE
2° STEP, 5mm/s

Figure 5. Ship Antenna Servo Responses

Since the antenna was not originally designed for this type of application, the servos driving the axes had to be modified. The result was a compromise between speed of response and system stability. The step responses of the servos, shown in Figure 5, indicate that the maximum rate capability of the elevation servo, which had a time constant of about 0.5 s, was $>6^\circ/\text{s}$. The azimuth servo had a maximum rate of about $3^\circ/\text{s}$, and a time constant of about 1 s. The static accuracy of the antenna drive system was about $\pm 0.125^\circ$ in each axis.

Another source of both static and dynamic mispointing was the alignment error between the antenna pedestal and the vertical gyro. Prior to the experiment there had been some apprehension about the operation of the vertical gyro high on the ship and to one side. This proved to be no problem. Aligning the antenna pedestal with the gyro reference, and the gyro output with respect to the vertical during pitch and roll motions required careful and painstaking measurements. The pointing error from this source was held to about 0.1° and did not seriously affect the overall pointing error.

All of these errors were taken into account to arrive at nominal system pointing errors of about $\pm 0.75^\circ$. The effect of these errors on the communications link can be seen by referring to the ship antenna beam contour curves of Figures 6 and 7, which show the loss in power as a function of the angle off axis. The nominal values of the shipboard station performance (Table 1) were derived from these curves and the nominal pointing errors.

RF interference and obstruction

Figure 8 shows the location of the antenna on the QE 2 and the obstruction of the antenna beam by the stack and mast of the ship. The smoke stack and the mast do not obstruct the antenna beam at elevation angles greater than 25° and 30° respectively. At smaller elevation angles, obstruction exists only when the antenna is pointing to within $\pm 2^\circ$ of the stack and $\pm 1^\circ$ of the mast. Thus, obstruction should be and was a rare occurrence.

The ship terminal did not interfere with the normal operation of any of the ship's communications or navigation equipment. On the other hand, when it was operating at 12.459 MHz, the ship's 1500-W high-frequency transmitter did cause interference to the receive end of the satellite link; i.e., bursts of noise were superimposed on the voice channel. Other frequencies of the same transmitter (8 and 16 MHz) did not cause any interference. Reasons for this could not be determined.

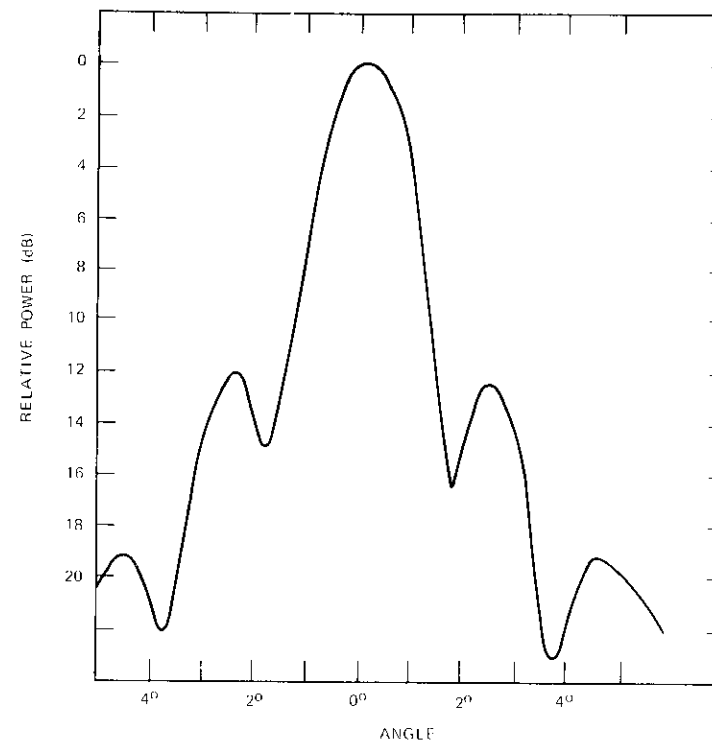


Figure 6. Ship Antenna Beam Pattern (6-GHz transmit)

Conclusions

Tests of the experimental satellite communications system onboard the QE 2 showed that it is feasible to install a highly directional antenna onboard a ship that is in commercial service, and to manually point and track a geostationary satellite by using a simple open-loop, gyrostabilized, antenna pointing system. The experimental system required frequent operator assistance. Any C-band system that is a candidate for operational use will require an improved automatic pointing or tracking system; however, at L-band, the antenna beamwidths would be wide enough to allow such a simple pointing system.

Carrier-to-noise ratios varied at each end of the link in fairly good agreement with the predicted pointing errors and the antenna beam contours. The ship environment produced only relatively minor interference

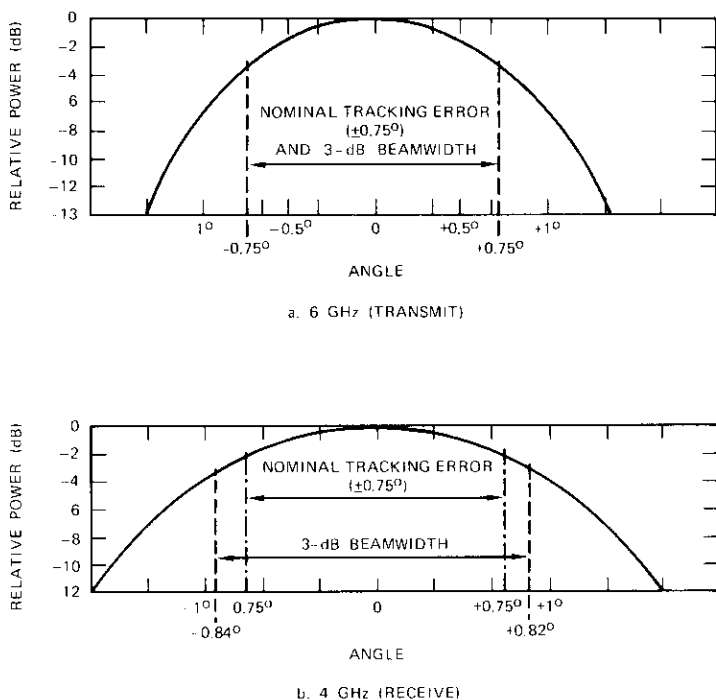


Figure 7. Detailed Ship Antenna Main Beam Contours

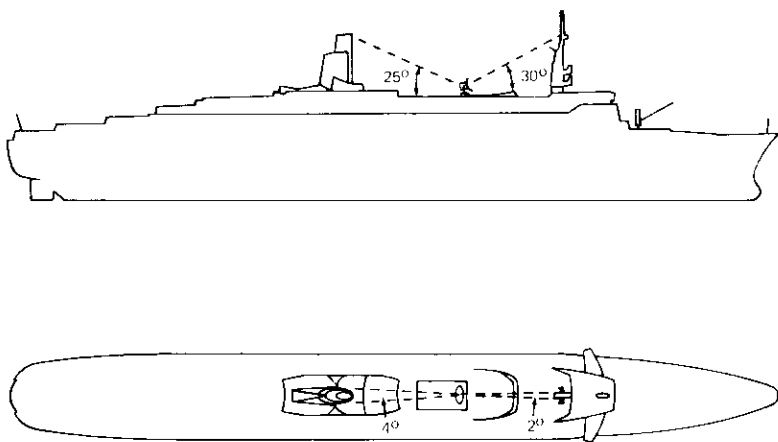


Figure 8. Antenna Installation on QE 2

to the satellite receive link, and obstruction by the ship's superstructure was rare. Because obstruction is obviously a strong function of the particular ship and permissible antenna location, no general conclusion can be drawn.

Appendix A includes some of the data obtained from the experiment and describes the manner in which conclusions on pointing accuracy and interference were drawn.

Acknowledgments

The author is indebted to John McClanahan for his efforts in the design and construction of the equipment and his untiring help in operating the system onboard the QE 2. Dr. E. Cacciamani and his coworkers provided the DICOM channel units and operated the Labs station. Particular thanks go to Commodore W. E. Warwick, Chief Officer Douglas Ridley, and the crew of the QE 2 for their assistance in the project. Thanks also go to the British Post Office for its considerable effort in obtaining frequency clearances for operating the ship terminal.

References

- [1] "Experimente mit dem Satelliten ATS-3 in Hinblick auf spätere Nutzung eines Navigationsatelliten in der Schifffahrt," *Deutsche Forschungs Versuchsanstalt für Luft und Raumfahrt*, June 1969 (in German).
- [2] "Investigation of L-Band Shipboard Antennas for Maritime Applications," Automated Marine International, Report NASW-2165, 2 February 1972.
- [3] E. R. Cacciamani, Jr., "A Channel Unit for Digital Communications in the SPADE System," IEEE 1971 International Conference on Communications, Montreal, Canada, June 1971, *Proceedings*, pp. 42-15-42-19.
- [4] E. R. Cacciamani, Jr., "The SPADE System as Applied to Data Communication and Small Earth Station Operation," *COMSAT Technical Review*, Vol. 1, No. 1, Fall 1971, pp. 171-182.
- [5] J. Kaiser and E. R. Cacciamani, "A Shipboard Satellite Communication Experiment," *Proceedings of the International Conference on Satellite Systems for Mobile Communications and Surveillance*, London, England, 13-15 March 1973.
- [6] "Radar Scanners and Radomes," M.I.T. Radiation Laboratory Series No. 26, Boston Technical Publishers, 1964, Appendix 1.

Appendix A. Presentation and analysis of recorded data

General

During the tests, data were recorded on stripchart recorders on the ship and at the Laboratories terminal. Only C/N data were recorded at the Laboratories. The shipboard data included received signal strength measurements (C/N), actually recorded in the form of $(C + N)/N^*$; ship motion (roll, pitch, and yaw) obtained from the terminal's two gyro outputs; and antenna motion rates obtained from rate gyros mounted on the antenna. The C/N data in Figures A-1 and A-2 were recorded at the Labs; all other data presented here were recorded on the ship.

Link performance

The link performance $[(C + N)/N]$ was recorded from the output of a signal strength meter. The resulting output had a nonlinear (logarithmic) scale on the chart recorder.

The received signal was simultaneously recorded at both ends of the link. Two examples are shown. In the first (Figure A-1), the chart speeds at both ends are the same, but the recording levels make it difficult to obtain quantitative measurements. For the second set of simultaneous signal strength recordings (Figure A-2), the chart speed at the Laboratories is equal to 25 mm/min, while that at the ship terminal is equal to 5 mm/min. Analysis of these and similar data furnished information on antenna pointing error performance and overall link performance.

Nominal antenna pointing error

The nominal antenna pointing error, i.e., the average amount of ship antenna mispointing, is ascertained by measuring the maximum received signal (assumed to occur when the antenna is pointed correctly) and estimating the average received signal in the vicinity of the maximum on the recording. Then the beam contours of the shipboard antenna can be used to obtain the pointing error in degrees. For measurements at the ship, the receive beam contour must be used, while at the Laboratories the transmit beam contour must be used. These contours are different because of the difference in frequencies; hence, different amounts of signal fade (dips in the curve) are observed. The dips in Figure A-2 correlate well with the beam contours. It is concluded that the antenna had a pointing error of about 0.5° , which increased momentarily to about 1.0° , causing a fade of about 4.5 dB at the Laboratories and 2.8 dB at the ship. An examination of many such recordings indicates that, under normal conditions, i.e., when the

*Carrier plus noise versus noise.

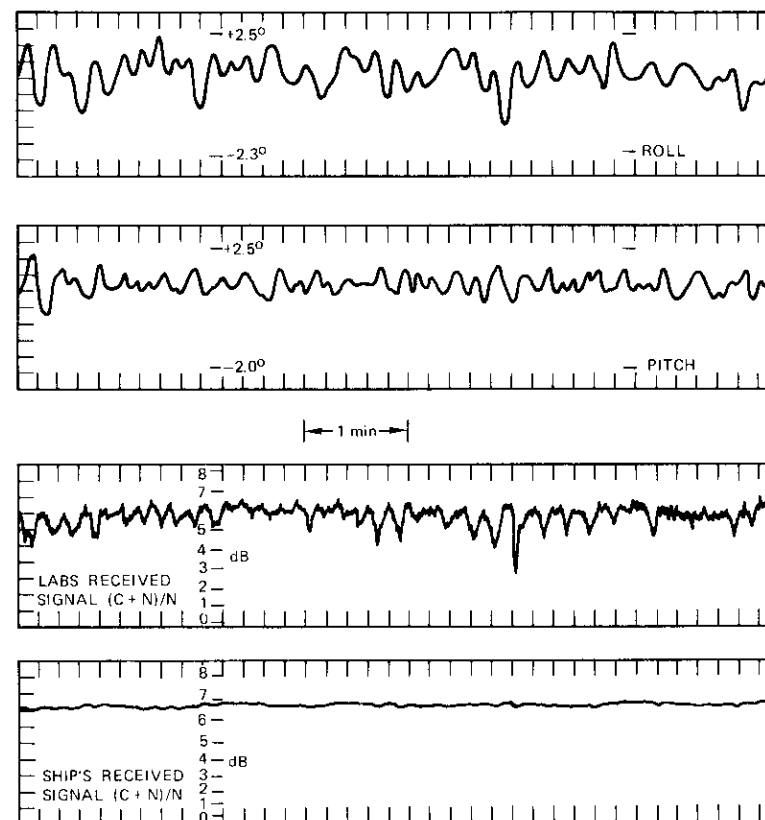


Figure A-1. Comparison of Received Signal at Labs and Ship Stations

link performed well, the nominal tracking error was about $\pm 0.75^\circ$. An example of these conditions is shown in Figure A-3.

Received signal strength measurements

Two factors made it difficult to record the received signal strength onboard the ship. First, the receiver gain varied nearly 1 dB as a function of the heating cycle. (The low-noise amplifier receiver was temperature controlled by an internal heater with a cycling time slightly over one minute). Second, the dual-channel, azimuth axis, RF rotating joint in the antenna (see Figure 2) contributed about 2 dB of gain variation as a function of the antenna azimuth pointing angle. This gain variation occurred only in the joint's 4-GHz receive channel, which used the "outside" channel of the joint. The inside channel, which is essentially a

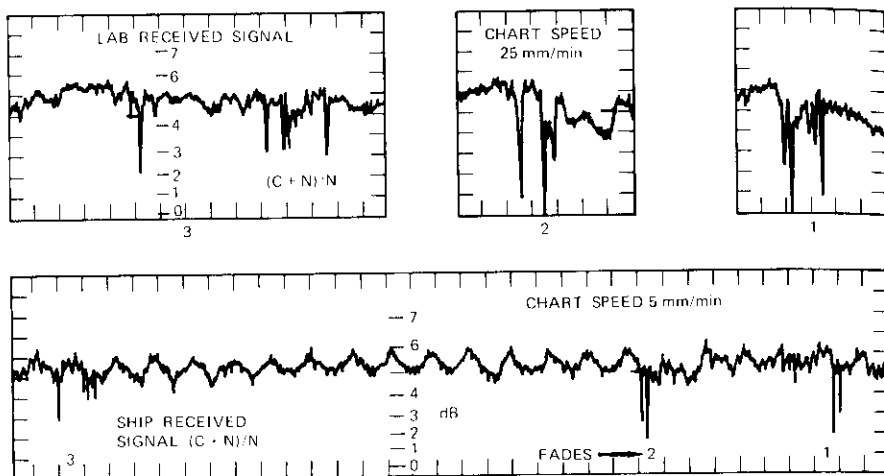


Figure A-2. Comparison of Received Signal at Labs and Ship Stations with Deep Fades

straight-through connection, was used for the 6-GHz transmit run, and did not have this problem.

The gain variations which occurred after the first 40 dB of signal amplification did not contribute significantly to the noise in the link, but simply shifted the output of the recording meter and hence the location of the trace on the strip recorder. The $(C + N)/N$ ratio was not altered. However, to read the received signal strength values, it is necessary to measure the location of the base line (N). When time permitted, frequent instantaneous $(C + N)/N$ measurements were performed by turning off the Labs carrier momentarily, recording the result at a high chart speed, and comparing the readings with the visual indication on the meter. Figure A-3 illustrates this instantaneous signal measurement calibration procedure.

Past experience indicates that C/N measurements on a satellite link such as the one used in the experiment, but with fixed terminals, generally yield values which are accurate to within 0.5 dB. Therefore, it should not be assumed that the records of the experiment are accurate to within less than 0.5 dB.

Interference and obstruction

The interference from the ship's 1500-W high-frequency transmitter to the satellite communications system pervaded virtually everything in the system, including all of the test equipment and the recorder channel, whose input was grounded. The ship's CW transmissions could even be heard as background noise in the ship's intercom system, which piped music and news to all of the cabins. It was impossible to ascertain where the interference entered the system,

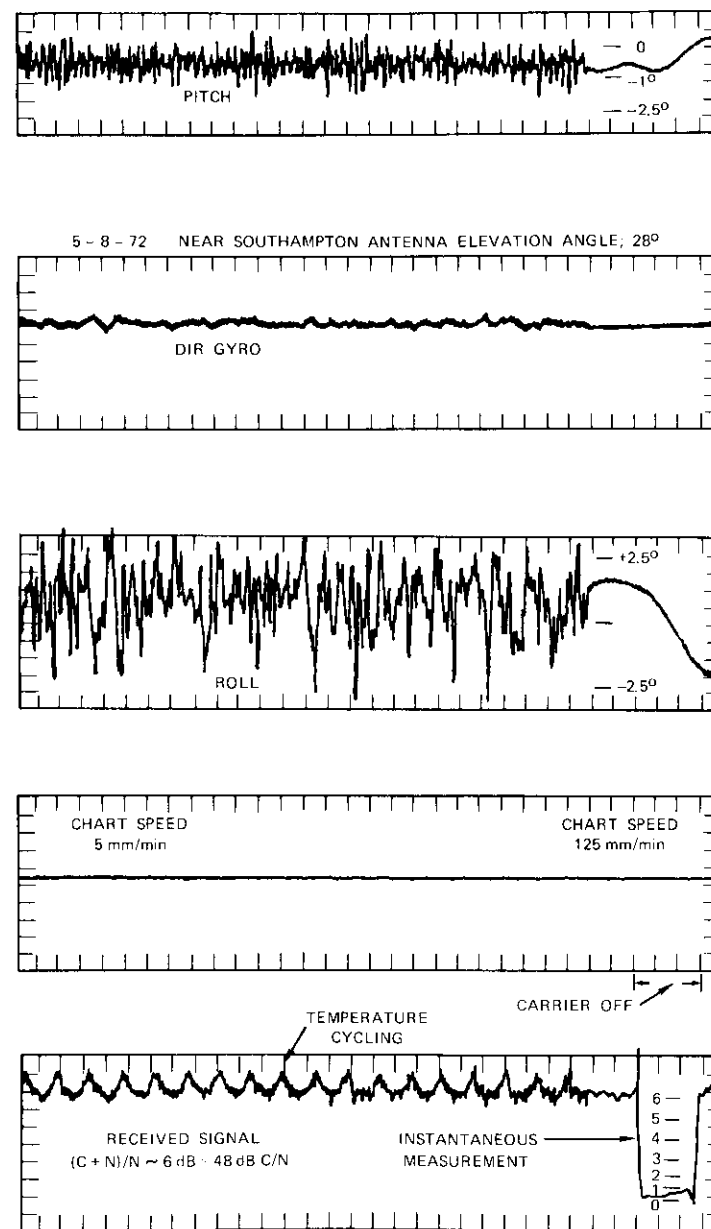


Figure A-3. Instantaneous Measurement of Received Signal

since no test equipment was free of the signal. Interestingly, the other frequencies (8 and 16 MHz) used by the same transmitter did not cause discernible interference.

Signal obstruction by the mast is illustrated in Figure A-4, in which the drop in C/N is clear. Obviously the system did not perform properly during the signal obstruction.

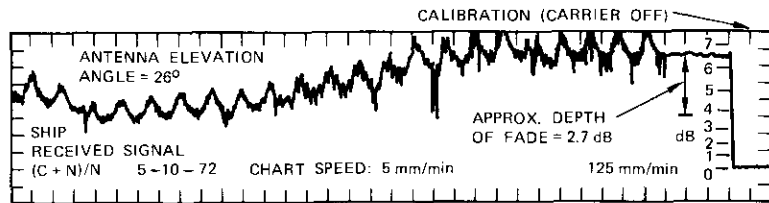


Figure A-4. Signal Obstruction by Ship's Mast



Joachim Kaiser received his B.A. and M.A. degrees in Mathematics in 1943 and 1948, respectively. He did additional graduate work in Communications Theory at the University of Michigan in 1967 and 1968. Prior to 1968 when he joined COMSAT Laboratories, where he is presently a senior staff scientist, he was employed at the Bendix Research Laboratory and the Institute for Defense Analyses. He is a senior member of the IEEE.

Index: multiple-beam satellites, carrier frequencies, power measurement.

Method for computing the optimum power balance in multibeam satellites

H. J. MEYERHOFF

(Manuscript received October 18, 1973)

Abstract

Multibeam satellites exploit the spectrum allocated for space communications by reusing the frequencies on adjacent beams. Aein has suggested that the transmitted carrier power levels to and from the various beams should be selected to equalize the interference-to-carrier power ratios on all beams. This paper proposes an iterative procedure for determining this unique set of carrier power levels, with one level predetermined. This procedure is rapidly convergent and less cumbersome to implement than other potential methods. The paper also demonstrates that equalizing these ratios is equivalent to minimizing the maximum interference-to-carrier power ratio on all beams, and that including thermal noise does not complicate or alter the stability of the iterative procedure.

Introduction

Future satellites will be equipped with spot-beam antennas that concentrate the satellite's transmitted power over small separate areas of the earth's surface. The angular separations between these spot beams at the

This paper is based upon work performed in COMSAT Laboratories under the sponsorship of the International Telecommunications Satellite Organization (INTELSAT.) Views expressed in this paper are not necessarily those of INTELSAT.

satellite provide sufficient discrimination in both reception and transmission to enable frequency reuse on adjacent beams [1]. Hence, heavy traffic links for point-to-point coverage can be implemented within the limited frequency bands allocated for space communications. Global and regional coverage antennas associated with most present-day satellites are more suited to broadcast and low-density multidestination traffic schemes in which frequency reuse is employed to a limited extent if at all.

Frequency reuse implies cochannel interference received at and transmitted from the satellite. It is possible to calculate the interference-to-carrier power ratio on each spot beam from a knowledge of the received and transmitted carrier power levels and a matrix description of the spot-beam antenna gains in the direction of their adjacent spot beams. Aein [2] has suggested that these interference-to-carrier power ratios should be equalized since system customers are usually interested in a standard of performance irrespective of the particular transmission path. Using a theorem of Frobenius, he has shown that, in most cases, there is a physically realizable solution for these carrier power levels which is unique and which corresponds to the eigenvector associated with the largest positive eigenvalue of the antenna beam matrix.

This paper shows that equalizing the interference-to-carrier power ratios actually corresponds to minimizing the maximum interference-to-carrier power ratio on all satellite beams. Furthermore, according to Perron [3], for a positive matrix such as that of the antenna patterns, in all cases there is a unique positive characteristic root having the largest absolute value; the eigenvector corresponding to this unique root is all positive. Computation of this eigenvector by using an iterative procedure [4], [5] yields the solution for the carrier power levels that minimize the maximum interference-to-carrier power ratio on all satellite beams. The method is unconditionally stable, capable of rapid convergence, and simpler to implement than a variety of other techniques. Thermal noise can readily be added to the interference power in the iterative program.

Selection criteria for normalized carrier power levels

The cochannel interference power received in one satellite spot beam may be obtained by summing the carrier power aimed at the remaining spot beams, weighted in accordance with the overall spot-beam antenna pattern, since the signals on each beam are assumed to be statistically independent. Then, from Aein,

$$(I/C)_i = \sum_{j=1}^n x_{ij} \frac{p_j}{p_i}, \quad i = 1, n \quad (1)$$

where $(I/C)_i$ = interference-to-carrier power ratio on the i beam

x_{ij} = antenna-beam matrix element ($x_{ii} = 0$)

p_j = carrier power received on the j beam

n = number of carriers.

It is evident from equation (1) that the carrier power levels may be normalized; one form is $p_1 = 1$. Appendix A shows that minimizing the maximum $(I/C)_j$, $j = 1, n$, is equivalent to equalizing these ratios on all beams. That is,

$$(I/C)_j = r_1, \quad j = 1, n \quad (2)$$

where r_1 , the unique eigenvalue of matrix x which yields as its corresponding eigenvector a realizable solution for carrier power p_i ($i = 2, n$), is real, positive, and the largest eigenvalue for a positive matrix x [3].

Iterative solution for carrier power levels

One method of determining the carrier power levels according to Aein's formulation would require a multidimensional search over all positive real values for p_i , $i = 2, n$, to find that set which equalizes $(C/I)_i$, $i = 1, n$. This method is cumbersome. Another method, indicated by an example in Aein's paper, is to find the eigenvalues of matrix x from its characteristic equation and then determine the eigenvector corresponding to the largest eigenvalue, presumably by matrix inversion. An iterative procedure suggested here always converges to the physically realizable unique solution associated with the largest eigenvalue [4], [5] of the antenna beam matrix. Within the iterative cycle of the computer program,

$$R_i(L) = \sum_{j=1}^n x_{ij} p_j(L-1), \quad i = 1, n \quad (3)$$

$$p_i(L) = \frac{R_i(L)}{R_1(L)}, \quad i = 1, n \quad (4)$$

where R_i is the interference power on the i beam and L is the iterative index. Under steady-state conditions,

$$\begin{aligned} \frac{R_i(L)}{p_i(L)} &= (I/C)_i \\ &= r_i, \quad i = 1, n \end{aligned} \quad (5)$$

Proof of convergence is given by

$$\begin{aligned} p(L) &= \frac{[x]}{R_1(L)} [p(L-1)] \\ &= \frac{[x]^L}{\prod_{j=1}^L R_1(j)} [p(0)] \end{aligned} \quad (6)$$

The initial values for the carrier power levels $[p(0)]$ may be written in terms of the eigenvectors $[E_m]$, $m = 1, n$, of matrix x suitably normalized; i.e.,

$$[p(0)] = [E_1] + U_2[E_2] + \dots + U_n[E_n] \quad (7)$$

where $|r_1| > |r_2| > |r_n|$ (8)

are the corresponding eigenvalues and U_m are constants. Then,

$$\begin{aligned} [p(L)] &= \frac{r_1^L}{\prod_{j=1}^L R_1(j)} \left\{ [E_1] + U_2[E_2] \left(\frac{r_2}{r_1}\right)^L + \dots + U_n[E_n] \left(\frac{r_n}{r_1}\right)^L \right\} \\ &\approx \frac{r_1^L}{\prod_{j=1}^L R_1(j)} [E_1] \end{aligned} \quad (9)$$

Under steady-state conditions, $L \gg 1$,

$$\begin{aligned} p(L) &\approx [p(L-1)] \\ &\approx [E_1] \end{aligned} \quad (10)$$

and

$$\begin{aligned} R_1(L) &\approx R_1(L-1) \\ &\approx r_1 \end{aligned} \quad (11)$$

The effect of thermal noise

For cochannel interference over equal bandwidths, it may be assumed that the thermal noise power is equal on all beams. It is of course statistically independent of all signal components. The noise-to-carrier power ratio is given by [2]

$$[(N+I)/C]_i = \sum_{j=1}^n W_{ij} \frac{p_j}{p_i}, \quad i = 1, n \quad (12)$$

where

$$\begin{aligned} W_{ij} &= x_{ij}, \quad j \neq 1 \\ W_{i1} &= N_0 + x_{i1} \end{aligned}$$

and N_0 is the thermal noise power normalized to carrier power p_1 .

As shown for the case without thermal noise in Appendix A, equalizing the noise-to-carrier power ratios in equation (12) is equivalent to minimizing the maximum ratio on all beams. Furthermore, since matrix W is positive, the iterative procedure for determining the unique set of carrier power levels continues to hold for the case of thermal noise.

Conclusion

Power balancing in multibeam satellites may be achieved by determining the carrier power levels that yield equal interference-to-carrier power ratios on all beams. Evaluation of these levels involves the solution of a set of simultaneous nonlinear equations by using an iterative procedure which can be shown to converge rapidly. Hence, this method is computationally more efficient than alternative schemes that require multidimensional searches or evaluation of the Perron eigenvalue of a matrix and subsequent inversion of a related matrix.

The ability to determine these carrier power levels will become important in the design of new satellite systems that incorporate frequency reuse on multiple antenna beams to provide the required communications capacity.

Acknowledgment

The author wishes to thank Dr. K. Chitre and Dr. O. Shimbo for useful discussions and encouragement.

References

- [1] R. W. Kreutel, "Antenna Design for Frequency Reuse Satellite Communications System," *1973 National Telecommunications Conference*, Atlanta, Georgia, November 26-28, 1973.
- [2] J. Aein, "Power Balancing in Systems Employing Frequency Reuse," *COMSAT Technical Review*, Vol. 3, No. 2, Fall 1973, pp. 277-301.
- [3] R. Bellman, "On an Iterative Procedure for Obtaining the Perron Root of a Positive Matrix," *Transactions of the American Mathematical Society*, 1955, pp. 719-725.
- [4] L. A. Pipes and S. A. Hovanessian, *Matrix Computer Methods in Engineering*, New York: J. Wiley and Sons, 1969.
- [5] D. K. Faddeev and V. N. Faddeeva, *Computational Methods of Linear Algebra*, San Francisco: W. H. Freeman, 1963.

Appendix A. Selection criterion equivalence

To demonstrate that minimizing the maximum interference-to-carrier power ratio is the same as equating these ratios to the Perron eigenvalue, r_1 , consider the simplest 3-carrier system, in which

$$R_1 = x_{12}p_2 + x_{13}p_3 \tag{A1a}$$

$$R_2 = \frac{x_{21} + x_{23}p_3}{p_2} \tag{A1b}$$

$$R_3 = \frac{x_{31} + x_{32}p_2}{p_3} \tag{A1c}$$

If

$$R_1 = R_2 = R_3 = r_1 > 0 \tag{A2}$$

then, from equation (2),

$$p_{20} = \frac{r_1 x_{21} + x_{23} x_{31}}{r_1^2 - x_{23} x_{32}} > 0 \tag{A3a}$$

$$p_{30} = \frac{r_1 x_{31} + x_{32} x_{21}}{r_1^2 - x_{23} x_{32}} > 0 \tag{A3b}$$

With small perturbations on p_2 and p_3 about p_{20} and p_{30} , respectively, all possible outcomes indicate that at least one of the resulting values for R_1 , R_2 , and R_3 will be larger than r_1 . Thus for perturbations $\Delta_2, \Delta_3 > 0$, substituting into equation (A1) yields

$$p_2 = p_{20} + \Delta_2, \quad p_3 = p_{30} + \Delta_3; \quad R_1 > r_1 \tag{A4}$$

$$p_2 = p_{20} + \Delta_2, \quad p_3 = p_{30} - \Delta_3; \quad R_3 > r_1 \tag{A5}$$

$$p_2 = p_{20} - \Delta_2, \quad p_3 = p_{30} + \Delta_3; \quad R_2 > r_1 \tag{A6}$$

$$p_2 = p_{20} - \Delta_2, \quad p_3 = p_{30} - \Delta_3 \tag{A7}$$

Then

$$p_2 = \frac{x_{21} + x_{23}(p_{30} - \Delta_3)}{p_{20} - \Delta_2} \tag{A8}$$

$$\approx r_1 + \frac{\Delta_2 r_1}{p_{20}} - \frac{x_{23} \Delta_3}{p_{20}}$$

For $R_2 \leq r_1$,

$$\frac{\Delta_3}{\Delta_2} \geq \frac{r_1}{x_{23}} \tag{A9}$$

Similarly,

$$R_3 = \frac{x_{31} + x_{32}(p_{20} - \Delta_2)}{p_{30} - \Delta_3} \tag{A10}$$

$$\approx r_1 + \frac{\Delta_3 r_1}{p_{30}} - \frac{x_{32} \Delta_2}{p_{30}}$$

For $R_3 \leq r_1$,

$$\frac{\Delta_3}{\Delta_2} \leq \frac{x_{32}}{r_1} \tag{A11}$$

but from equation (A3),

$$r_1^2 > x_{23} x_{32} \tag{A12}$$

Hence r_1 is the minimum value for the maximum of R_1 , R_2 , and R_3 . Similar reasoning may be applied to systems with more than three carriers.



Henry J. Meyerhoff graduated from Edinburgh University with a B.Sc. with Honors in Electrical Engineering in 1956. He spent three years with Marconi's W. T. Co. Ltd., then, with the aid of a D.S.I.R. fellowship, received a Ph.D. in Automatic Control from Cambridge University in 1963. He is a member of IEEE and a former member of S.E.G. Since joining COMSAT Laboratories in 1968, he has worked on systems and propagation studies related to new satellite systems. He also has taught

postgraduate courses at Waterloo University, Ontario, and Rice University, Houston.

Index: Intelsat IV, earth stations, radio frequency interference transponders.

Review of Intelsat earth station RF out-of-band emission criteria

M. P. BROWN, JR.

(Manuscript received October 1, 1973)

Abstract

The earth station RF out-of-band emission criteria employed in the INTELSAT system are reviewed. The review shows that, when INTELSAT IV satellites reach their maximum traffic carrying capacity, it will become increasingly difficult to limit RF out-of-band emission to the budgeted level of 500 pWp through up-link power adjustments at appropriate earth stations. In addition, the review shows that carrier frequency assignments for stations with heavy traffic must be selected so that intermodulation products fall where the resulting interference does not cause the system objectives to be exceeded.

The possible impact of out-of-band emission on a fully loaded satellite is analyzed in terms of a 1975 Atlantic region frequency plan. Detailed calculations are presented in this paper to illustrate the method of analysis utilized for various transponder configurations, such as spot-beam multicarrier FDM-FM-FDMA operation.

Introduction

The RF out-of-band emission criteria used for the INTELSAT IV satellite system were developed in 1969, two years before the launch of the first

This paper is based upon work performed in COMSAT Laboratories under the sponsorship of the International Telecommunications Satellite Organization (INTELSAT). Views expressed in this paper are not necessarily those of INTELSAT.

INTELSAT IV spacecraft. It was felt that a review of the original criteria was necessary in light of relatively new system concepts which might have influenced the outcome of earlier decisions. The two concepts probably having the greatest effect on these decisions were the introduction of carriers which placed a greater demand on available satellite power, and the implementation of a "2-satellite program" in the Atlantic Ocean region, a primary satellite for small carriers and a major path satellite for large carriers.

During the early studies, RF out-of-band emission was the subject of a great deal of debate because of the tradeoff between the transmitter output backoff and the per-channel system noise budget. It was observed that operation of a transmitter close to saturation would, of course, produce more output power; however, it was also noted that this would generate more out-of-band emission.

For the unfamiliar reader, the phrase "RF out-of-band emission" may require clarification. In this paper, it refers to the unwanted radiation generated by the intermodulation of carriers within an earth station's wideband high-power amplifier (HPA). When transmitted, these intermodulation products may fall within the satellite frequency band or outside of the satellite band. RF out-of-band emission is therefore meant to indicate RF emission which is out of the wanted carrier's band.

As a compromise, an emission level of 26 dBW/4 kHz* (representing an approximate output backoff of 7 dB for most transmitters) was chosen. This decision was based on the realization that a level of 26 dBW/4 kHz could add from 1,000 to 4,000 pWp of noise to the up-link of some carriers (much more than the 500 pWp already allotted for out-of-band emission in the system noise budget). However, it was felt that system performance objectives could still be met, since the power levels of various carriers could be reoptimized, thereby reducing the effective emission noise to 500 pWp in all cases. Hence, a reasonable transmitter output backoff could be employed and, at the same time, a 500-pWp noise level could be maintained in the system noise budget. Because of the introduc-

* A level of 26 dBW/4 kHz was considered to be the maximum allowable emission level from an earth station with an elevation angle of 10°. For other elevation angles the criterion was adjusted by using the empirical equation

$$26 - 0.06(\alpha - 10) \text{ dBW/4 kHz}$$

where α = elevation angle [1].

tion of new system concepts, the application of this philosophy to a fully loaded satellite will require careful engineering and operational management in order to keep within the constraint of 26 dBW/4 kHz.

Evaluation of RF out-of-band emission criteria

Comparison of 1969 and 1975 frequency plans

To evaluate the total RF out-of-band emission confronting an INTELSAT IV satellite in 1975, the intermodulation power spectral density produced by each of the 17 countries operating in the frequency plan shown at the top of Figure 1 was computed. A composite of all earth station emission was then prepared so that it could be compared directly with the analysis made in 1969 as shown in Figure 2. The observations drawn from this comparison will be discussed in the following paragraphs.

As shown in Figure 1, the intermodulation spectral density from the heavy-traffic earth station designated ET appears to have the most significant contribution to the total emission environment in the special case in which this earth station is called upon to transmit a contingency carrier for restoration of service in the event of submarine cable failure. Although these products are significant, they are still below the prescribed limit of 26 dBW/4 kHz.

Actual INTELSAT IV performance was better than specified; thus, it was possible to expand the channel capacity of selected carriers. Because of the utilization of such expanded carrier sizes, the transponders in the 1975 frequency plan will be saturated. The use of carriers with heavier baseband loading had not been envisioned in 1969; as a result, the power levels of the affected carriers in the 1975 frequency plan cannot be further increased to overcome out-of-band emission noise greater than 500 pWp. If the power levels are increased, either transponder loading must be decreased (carriers taken out), a degradation in channel performance must be accepted (total noise greater than 500 pWp), or still other steps be taken. For the carriers shown in Figure 1, the impact of the emission products falling under transponders 1 and 3 are shown in Table 1. (Alternatives to this situation will be discussed later.)

As a result of the factors described in the preceding paragraph, the present situation is one in which the emission products are within the original guidelines prescribed in 1969, but because of increased utilization of transponder loading, the system cannot be operated as originally planned without some modifications.

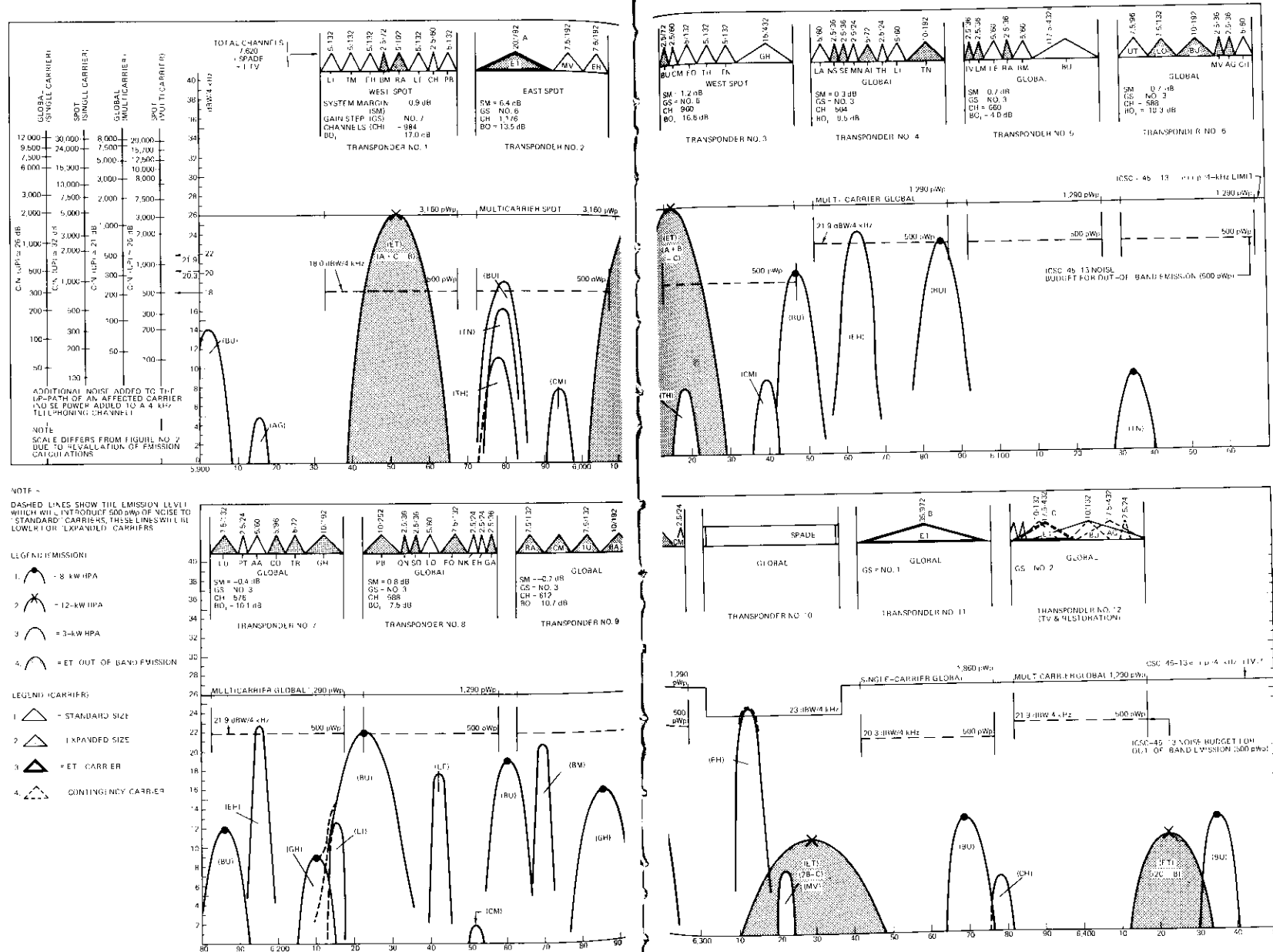


Figure 1. Carrier Arrangement and Earth Station Out-of-Band Emission

as Seen by the Satellite, Primary Atlantic (1975 frequency plan)

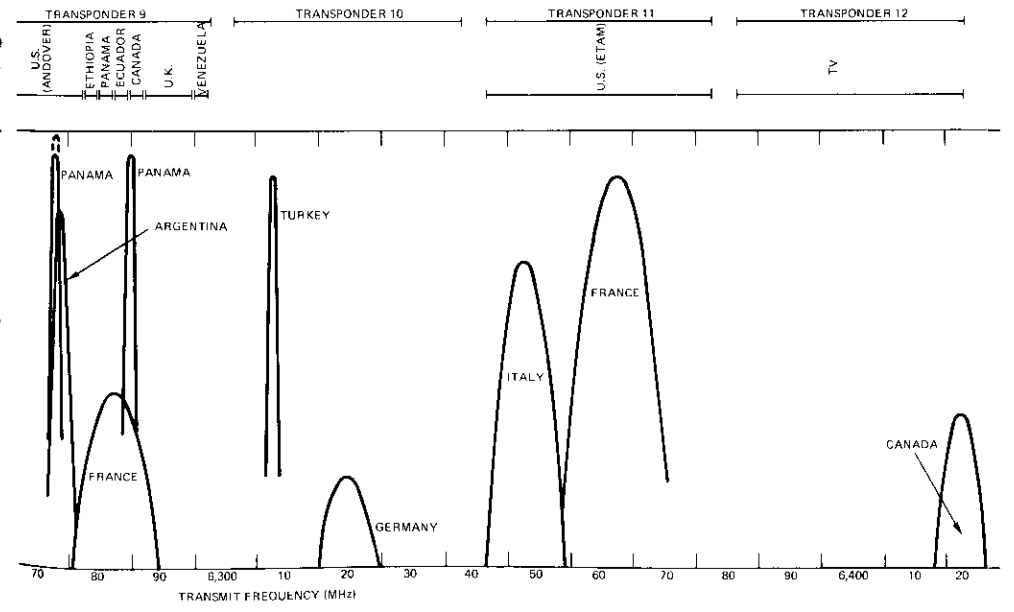
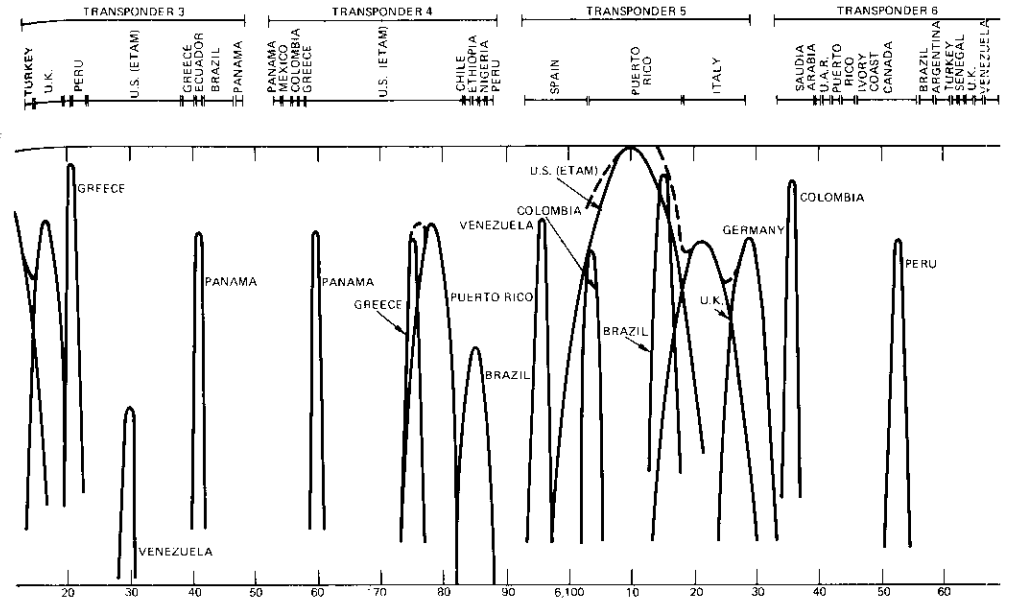
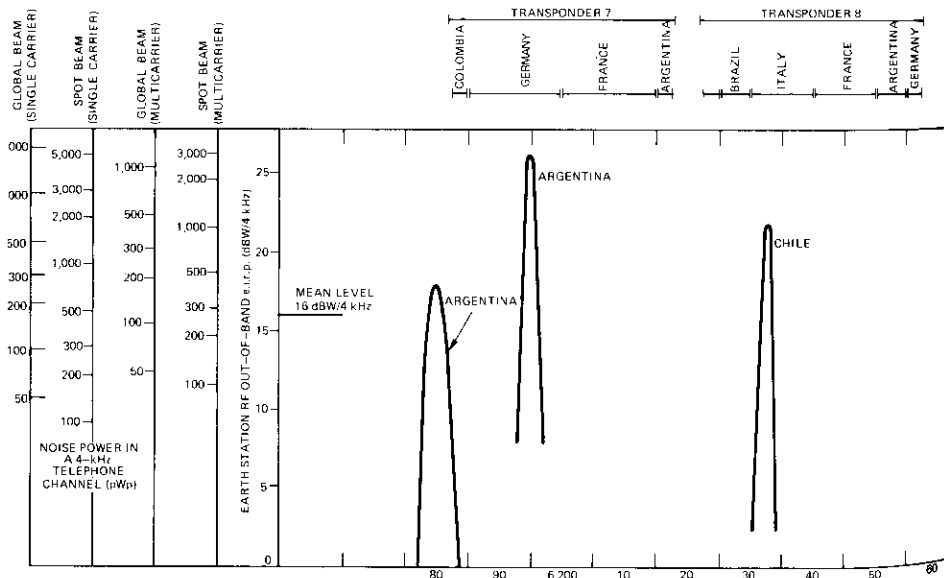
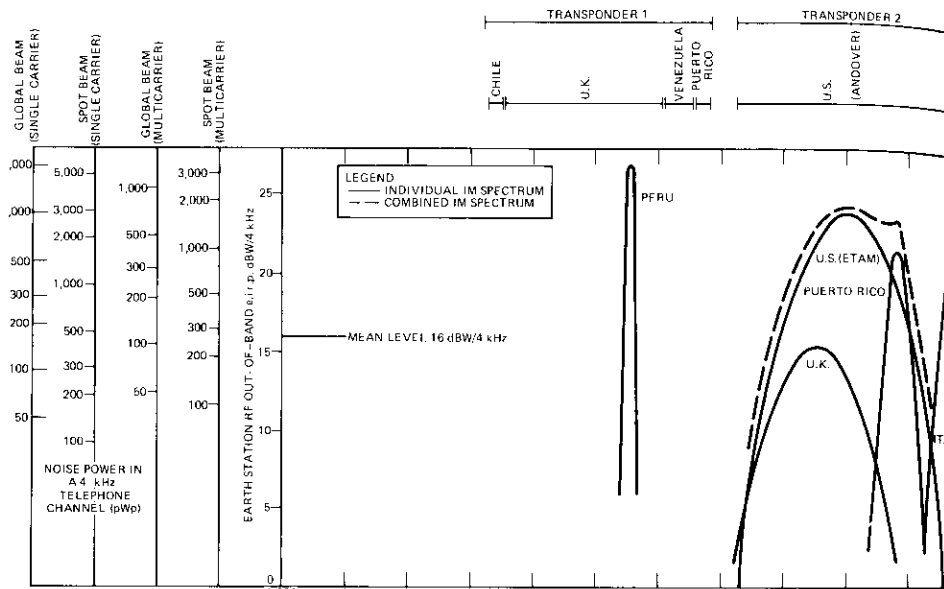


Figure 2. Carrier Arrangement and Earth Station Out-of-Band Emission as Seen by the Satellite (1969 frequency plan)

TABLE 1. IMPACT OF LARGE 3RD-ORDER PRODUCTS ON AFFECTED CARRIERS BEFORE CORRECTIVE ACTION ^a
(pWp of additional noise to up-link)

Transponder	Carrier Affected ^c	Noise Added to Up-Link of Affected Carrier ^b (pWp)
1	EH	1,500
	BM	2,800
	RA	2,800
	LE	1,200
3	BU	3,000
	CM	3,000
	FO	2,000

^a See $A + B - C$ and $A + C - B$ products in Figure 1.

^b For contingency carrier transmission prior to corrective action. 500 pWp is normally budgeted.

^c Abbreviations correspond to carrier designations of Figure 1.

When the heavy-traffic station is not transmitting a contingency or TV carrier, the peak RF out-of-band emission for the entire satellite system falls to approximately 23 dBW/4 kHz, well within the allowable limit of 26 dBW/4 kHz.

The contribution of several products falling in the same frequency range is indicated by the dotted lines in Figures 1 and 2. In most cases the net impairment is not significant. However, depending upon the particular frequency arrangement involved, there might be a special case in which the sum of several products would cause a serious total noise level.

The RF out-of-band emission environment shown in Figures 1 and 2 has been presented at the beginning of this paper to provide the reader with an overview of the total problem. This section, together with the next section, which describes the assumptions used to produce these mosaics, should form the basis for an understanding of the calculations which resulted in the scales at the left of these figures.

Assumptions employed for the preparation of the RF out-of-band emission environment in 1969 and in 1975

Table 2 compares the assumptions made in 1969 with those employed for the evaluation of the 1975 frequency plan. It can be seen that the 1969 frequency plan was indeed a worst-case plan in terms of the number of earth stations employing TWTs (and transmitting two or more carriers).

It is assumed that earth stations with multiplexed klystrons, one for each of several carriers, do not emit intermodulation products. A more extensive comparison of the two evaluations is provided in the following paragraphs.

In 1969, it was assumed that 19 earth stations would operate their transmitters at an output backoff of 7 dB. The introduction of a 2-satellite concept in the Atlantic has eliminated this possibility since carriers are now split between separate earth stations. On the basis of this concept, the 1975 frequency plan would have only four stations operating near an output backoff of 7 dB.

Although a total of 39 earth stations are projected to be within the 1975 frequency plan, only 17 of these stations would transmit two or more carriers and utilize wideband TWTs. There are other stations which radiate two or more carriers, but these stations are currently equipped with multiplexed klystrons and they will not create out-of-band emission.

TABLE 2. COMPARISON OF ASSUMPTIONS FOR 1969 AND 1975 FREQUENCY PLANS

Criterion	1969 Plan	1975 Plan
Number of earth stations with two or more carriers and wideband TWT transmitters	19	17
Number of earth stations operating at or near 7 dB output backoff	19	4
Net earth station transmit antenna gain at 6 GHz ^a (dB)	60	60
Type of intermodulation product considered ^b	3rd order	3rd order
Carrier sizes used in frequency plan	standard	standard and expanded
Same TWT transfer curve employed for all HPAs considered?	yes	yes
Method used to calculate transmit power levels for optimum transponder performance	manual	system model

^a Except ET whose 12-kW HPA is located in the upstairs portion of the antenna pedestal near the feed. The antenna gain in this case has been assumed to be 62 dB.

^b It is assumed that harmonics (e.g., 2A and 2B) are eliminated by harmonic filtering normally found in HPA equipment. It is further assumed that 5th- and higher-order products do not contribute significantly to total emission levels.

Only 3rd-order products have been considered in both the 1969 and 1975 frequency plans. Harmonics which fall well outside the satellite band (e.g., 2A and 2B) are normally removed by the filtering inherent in HPA equipment. It is felt that 5th- and higher-order products do not contribute significantly to total emission levels.

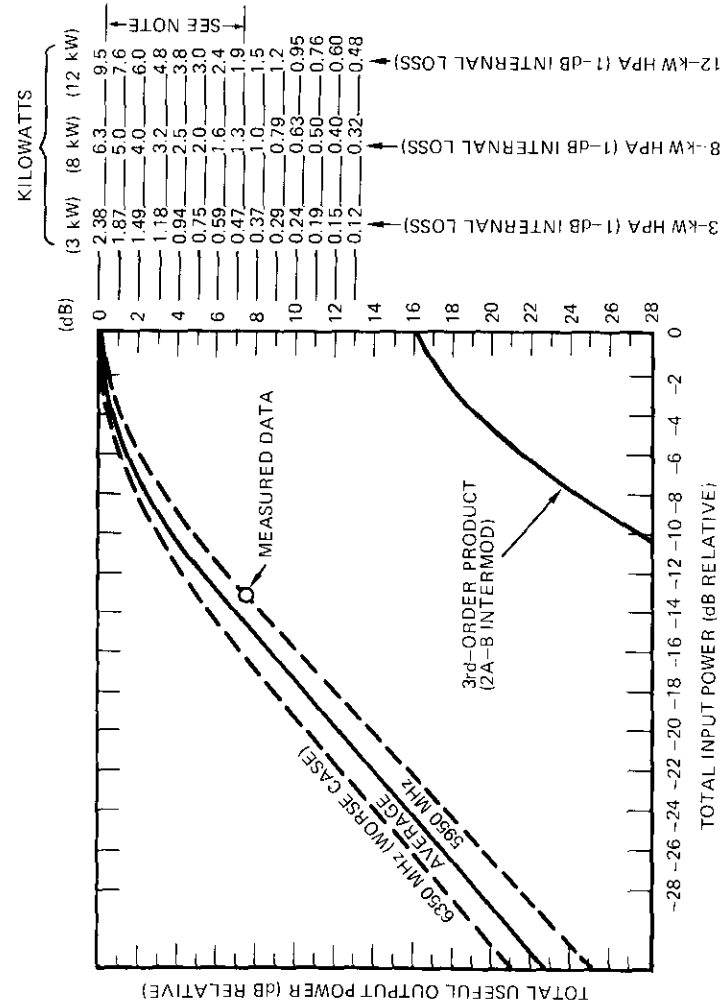
In both the 1969 and 1975 frequency plans, the same TWT transfer curve was employed for all earth station TWT transmitters. That is, one TWT curve was assumed to be typical of all HPAs. The curve employed for the 1975 plan (Figure 3) represents the amplitude transfer characteristic of an 8-kW Varian 6660A2 TWT. Note that the exact output backoff is frequency dependent and that an average curve has been assumed to lie between the upper and lower frequency bounds. Actual HPA output backoffs could then vary ± 1 dB from the average chosen for this study.

A computer program developed by COMSAT Laboratories was used to calculate the intermodulation products shown in Figure 1. The program also includes the simultaneous treatment of distortion caused by amplitude compression and AM to PM conversion, and provides an improved capability for computing products generated by TV and SPADE* carriers [2], [3].

The backbone of an RF out-of-band emission analysis is an accurate assessment of the earth station transmit power requirements of each carrier. Carrier power requirements depend upon earth station location and carrier placement within the satellite transponder. An optimum transponder operating point which is related to the carrier power levels and the varying intermodulation pattern produced by the adjustment of each carrier can be found. Changes in the relative power levels affect the intermodulation structure and the backoff of the transponder. For the 1969 analysis, a manual optimization process was used. For the 1975 analysis, a computerized INTELSAT IV system model was employed, which could perform the many iterations necessary to calculate the best carrier power levels.

To simplify the calculations in both studies, it was assumed that earth stations had a net antenna gain of 60 dB from the output of the HPA flange up to and including the antenna. There was one exception to this general rule. It was known that the ET earth station had just undergone a modification during which its 8-kW HPA was replaced by a 12-kW HPA.

* SPADE is an acronym for Single-channel-per-carrier, Pulse-code-modulation, multiple-Access, Demand-assignment Equipment.



NOTE: AN OUTPUT BACKOFF OF 7 dB IS THE NOMINAL MAXIMUM FOR 26 dB BW/4 kHz. AN OUTPUT BACKOFF IN THE REGION 0 dB TO 7 dB IS NOT RECOMMENDED WITHOUT CLOSE EXAMINATION OF A PARTICULAR HPA'S CHARACTERISTIC.

Figure 3. Amplitude Transfer Characteristic, 8-kW HPA, VA-6660A2

In addition, the HPA was removed from its original position in the downstairs portion of the antenna pedestal and relocated close to the antenna feed. It was assumed that this modification, along with the measured antenna gain, provided a net gain of 62 dB.

It was assumed that all HPAs had a 1-dB internal loss between the TWT and the HPA output flange. Hence, a TWT rated at 8 kW would have an effective HPA rating of 6.3 kW.

With these assumptions as a baseline, the emission products generated from each earth station were pieced together into a final mosaic representing the total system. Once the mosaic was completed, calculations were performed to assess the impact of the products on system operation.

RF out-of-band emission criteria calculations

The philosophy used to derive the emission level of 26 dBW/4 kHz was based on the premise that a given amount of emission noise introduced into the system will affect carrier types differently according to their link noise budget and respective up-link C/N ratios (see Table 3). For example, a spot-beam carrier with an up-link C/N of 26 dB will notice a degraded noise level before a global-beam carrier with an up-link C/N of 21 dB.

TABLE 3. EFFECT OF OUT-OF-BAND EMISSION ON VARIOUS CARRIER TYPES

Type of Carrier Affected	Up-Link C/N (dB)	Additional Noise Added to the Up-Link at 26 dBW/4 kHz (pWp)
Global Beam (single carrier)	25.9	1,860
Global Beam (multicarrier)	20.9	1,290
Spot Beam (single carrier)	31.9	4,350
Spot Beam (multicarrier)	25.7	3,160

Two methods of calculation are used to test this philosophy; both arrive at essentially the same conclusion and differ only slightly from the original calculations. This difference, whose magnitude is shown by the scales at the left of Figures 1 and 2, is attributed to a refinement in the method of calculation.

RF out-of-band emission criteria calculations have been performed for each of four cases shown on the scales in Figures 1 and 2:

- multicarrier spot-beam transponders,
- single-carrier spot-beam transponders,
- multicarrier global-beam transponders,
- single-carrier global-beam transponders.

Each case has been calculated separately by using the same general approach of finding the up-link C/N ratio and then determining the emission level in dBW/4 kHz which, when added to the up-link, will cause the total space-segment noise budget to increase from 7,500 to 8,000 pWp. For the sake of brevity, only the spot-beam multicarrier case has been treated here.

METHOD 1, MULTICARRIER SPOT-BEAM TRANSPONDER CASE

The calculations for a multicarrier spot-beam transponder (Figures 4 and 5) are as follows:

- total transponder up-link power at the multicarrier spot-beam operating point (beam edge):

$$\begin{aligned}
 P_E &= W_s - BO_i + PL|_{6\text{GHz}} - \text{gain } 1 \text{ m}^2 + \text{G.A.}|_U \\
 &= -57.2 - 16 + 200.6 - 37 + 0 \\
 &= 90.4 \text{ dBW}/32.4 \text{ MHz} \\
 &= 51.4 \text{ dBW}/4 \text{ kHz}
 \end{aligned}$$

$$\begin{aligned}
 \text{where conversion factor} &= \frac{32.4 \times 10^6}{4 \times 10^3} \\
 &= 8.1 \times 10^3 \\
 &= 10 \log_{10} 8.1 \times 10^3 \\
 &= 39 \text{ dB}
 \end{aligned}$$

- total transponder up-link C/T over 32.4 MHz:

$$\begin{aligned}
 C/T|_U &= P_E - PL|_{6\text{GHz}} + G/T|_{\text{sat.}} + \text{G.A.} \\
 &= 90.4 - 200.6 - 17.6 + 0 \\
 &= -127.8 \text{ dBW/K}
 \end{aligned}$$

c. transponder up-link C/N :

$$\begin{aligned} C/N|_U &= \frac{C}{kTB} \\ &= -127.8 + 228.6 - 10 \log 32.4 \times 10^6 \\ &= -127.8 + 228.6 - 75.1 \\ &= 25.7 \text{ dB} \end{aligned}$$

d. total down-link C/T over 32.4 MHz at the transponder operating point:

$$\begin{aligned} C/T|_D &= \text{e.i.r.p.}|_{\text{sat.}} - BO_o - PL|_{4\text{GHz}} \\ &\quad + G/T|_{\text{es}} + G.A.|_D \\ &= 34.2 - 8.8 - 196.7 + 40.7 + 1.0 \\ &= -129.6 \text{ dBW/K} \end{aligned}$$

e. transponder down-link C/N :

$$\begin{aligned} C/N|_D &= \frac{C}{kTB} \\ &= -129.6 + 228.6 - 75.1 \\ &= 23.9 \text{ dB} \end{aligned}$$

f. transponder intermodulation C/N :

$$\begin{aligned} C/N|_I &= C/N|_{\text{total}} - C/N|_U - C/N|_D \\ C/N|_I &= 21 - 25.7 - 23.9 \\ &\equiv 7,500 \text{ pWp} - 2,600 \text{ pWp} - 3,800 \text{ pWp} \\ &= 1,100 \text{ pWp} \\ &\equiv 29.4 \text{ dB} \end{aligned}$$

g. amount of RF out-of-band emission necessary to add 500 pWp of noise to the up-link:

- change from 2,600 pWp to 3,100 pWp: 0.75 dB
- noise level 25.7 dB down from 51.4 dB/4 kHz:
 $51.4 - 25.7 = 25.7 \text{ dBW/4 kHz}$
- emission necessary to increase the noise level by 0.75 dB (500 pWp):
 $OBE + 25.7 = 26.4 \text{ dBW/4 kHz}$
 $OBE = 18.0 \text{ dBW/4 kHz (500 pWp of added noise).}$

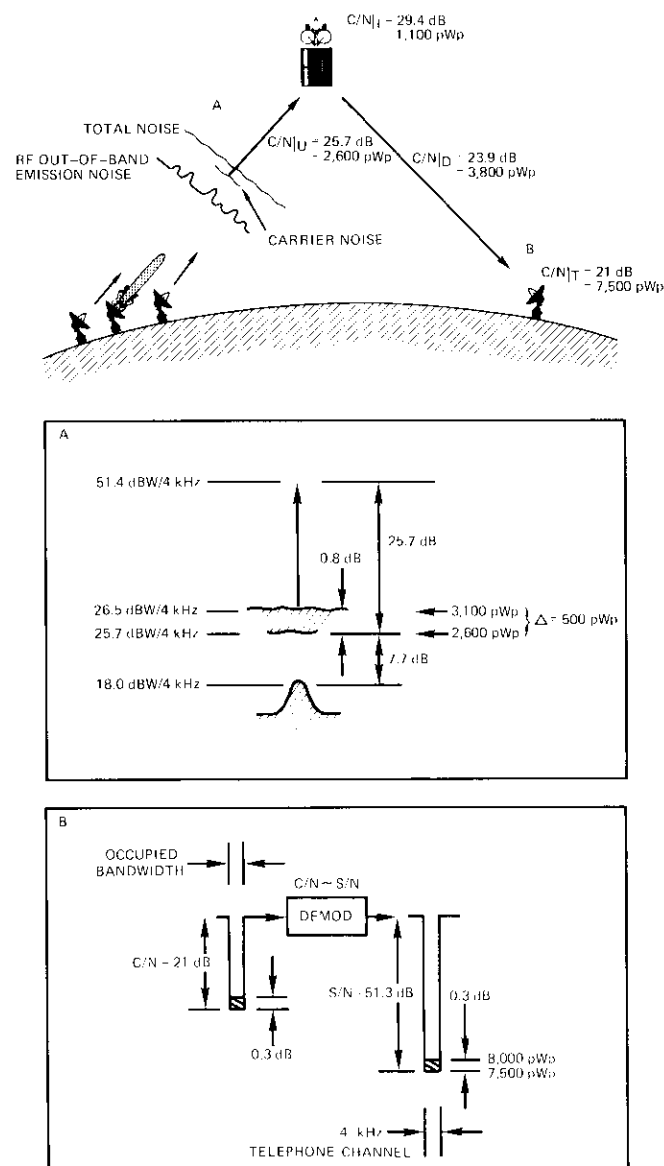


Figure 4. Calculation of RF Out-of-Band Emission, Multicarrier Spot-Beam Transponder (emission level necessary to add 500 pWp of noise)

lishes the noise level that will change with an increase in out-of-band emission, only the up-link should be treated as specified in method 2. Fortunately, emission levels derived by using the two methods differ by only a few hundred pWp.

Review of RF out-of-band emission criteria

The standard of 26 dBW/4 kHz was derived on the premise that, if an emission product at this level were to fall under a spot-beam carrier, for example, the up-link power of the affected carrier could be increased to overcome the added emission noise with a better up-link C/T . Hence, it was felt that the total up-link, down-link, satellite intermodulation, and earth station intermodulation noise could be kept within the budgeted noise allocation of 8,000 pWp per channel.

However, by 1975, and in some cases sooner, transponder loading will be saturated to the extent that increasing the power of one carrier will upset the delicate power balance which must be maintained by the neighboring carriers to operate the transponder at optimum channel capacity. In other words, by 1975, control of out-of-band emission using the concept envisioned in 1969 will no longer be possible. The following example will illustrate this point.

As shown in Figure 1, a large $A + B - C$ product falls in spot-beam transponder 1 under the BM and RA carriers at a level of approximately 26 dBW/4 kHz. Since this product occurs in the spot-beam transponder, its impact on the BM and RA carriers is equivalent to the addition of 2,800 pWp of noise to the up-link of each carrier.

As mentioned previously, the original solution to this problem was to increase the power level of the two affected carriers until the up-link C/T was sufficient to compensate for the additional noise, i.e., about 1 dB for each carrier. Since transponder 1 has no excess power margin for its particular carrier arrangement, several changes will occur if the e.i.r.p. of the affected carriers is increased:

- a. a new transponder backoff (closer to saturation) will be produced, resulting in a higher intermodulation level;
- b. the optimized power balance of the other carriers will be upset;
- c. the total C/T available for all carriers will be less so that the power margin will be degraded.

An interesting situation will therefore exist in 1975. Only the intermodulation products from the station with heavy traffic will create troublesome

emission levels. Although these levels will be within the current INTELSAT criteria, they will still produce far more noise than was allocated in the system noise budget. For this particular earth station (ET), three steps have been taken to ensure that the system noise budget will be met:

- a. To reduce waveguide loss, the original 8-kW HPA has been relocated near the antenna feed. In addition, a 12-kW HPA has been installed to operate the transmitter safely under peak loading conditions.
- b. Steps have been taken to minimize the possibility that a 432-channel/17.5-MHz contingency carrier will be required for future cable restoration. A new restoration plan which will transfer this service to other earth stations under normal operating conditions has been devised.
- c. The feasibility of using notch filters with an attenuation of 10–15 dB is under active investigation. These filters would be inserted into the system if a contingency carrier were to be transmitted.

As indicated by this example, there are alternative solutions to the problem of limiting out-of-band emission to 500 pWp in addition to the one envisioned in 1969.

TWT vs klystron systems for earth station HPAs

To determine the type of transmitter which is to be used for an earth station HPA, several factors must be considered. One of these, of course, is out-of-band emission; however, other equally important factors, many of which are peculiar to an individual earth station, must also be considered. For example, the cost of a multiplexed klystron system handling large carriers would have to be compared with that of a TWT system. In addition, it is more difficult to reduce group-delay distortion in klystrons when large carriers are transmitted. Operational features must also be examined if it is expected that new carriers will be introduced frequently. In essence, there are problems associated with either alternative so that the final decision will be a tradeoff among several factors.

Future satellite systems

The next generation of INTELSAT satellites, INTELSAT IV-A, will be introduced in the Atlantic region in the 1976 time frame. A detailed analysis of RF out-of-band emission for this system is still being studied, but some points are already becoming clear. Because of the exchange between

higher satellite receive antenna gain and interference effects of frequency reuse, the carrier-to-noise ratio of INTELSAT IV-A carrier sizes will be less than or equal to those of the INTELSAT IV system. The use of multibeam antenna configurations on the INTELSAT IV-A will result in the transmission of more carriers per earth station, thus spreading out the intermodulation spectrum generated by wideband TWTs. The tradeoff between a higher satellite receive gain and the requirement to transmit more carriers is likely to result in transmitter backoffs very close to those of the INTELSAT IV system).

Conclusion

This review has shown that RF out-of-band emission will have a somewhat higher impact on the INTELSAT IV system than was originally projected by early studies. The central problem area consists of those earth stations handling large traffic trunks with wideband TWT transmitters. The impairment will first become apparent in the Atlantic and then, as traffic levels increase, in the Pacific and Indian Ocean regions.

It was originally envisioned that RF out-of-band emission could be overcome by simple adjustment of an affected carrier's up-link power level. However, in actual practice this method will be difficult to employ when the traffic handling capacity of an INTELSAT IV satellite is raised above the original estimates to meet increased traffic requirements. Increase in traffic was actually accommodated both by using the available margin and by improving the performance of the INTELSAT IV satellite series above specifications. However, the power margin originally reserved for balancing RF out-of-band emission is eventually depleted. The problem is not due to the inability of earth stations to meet the original criteria, but is reflected in a somewhat different method of system operation than was originally planned to meet an increase in traffic requirements.

Two actions are necessary to ensure that the effects of out-of-band emission are kept within the prescribed noise budget of 500 pWp. First carrier frequency assignments for earth stations with heavy traffic must be selected so that intermodulation products fall where they create the least problem, preferably out of the satellite band. Second, if, because no other alternative exists, large products do fall in-band, appropriate measures must be taken at the earth stations to reduce the products to acceptable levels.

Implementation of new satellite systems such as INTELSAT IV-A or INTELSAT V will require reexamination of RF out-of-band emission criteria.

Acknowledgments

Thanks are due to Mr. J. Dicks for his contributions to the decisions regarding RF out-of-band emission criteria and his guidance in the preparation of this paper.

Glossary

- BO_i Satellite transponder TWT input backoff in dB
 BO_o Satellite transponder TWT output backoff in dB
 $C/N|_D$ Down-link carrier-to-noise ratio in dB
 $C/N|_I$ Carrier-to-intermodulation noise ratio in dB
 $C/N|_T$ Total carrier-to-noise ratio in dB
 $C/N|_U$ Up-link carrier-to-noise ratio in dB
 $C/T|_D$ Down-link carrier-to-noise temperature ratio in dBW/K
 $C/T|_I$ Carrier-to-intermodulation noise temperature ratio in dBW/K
 $C/T|_T$ Total carrier-to-noise temperature ratio in dBW/K
 $C/T|_U$ Up-link carrier-to-noise temperature ratio in dBW/K
 C_M/N_o Multicarrier-to-noise density in dB-Hz
e.i.r.p._{sat.} Satellite transmit e.i.r.p. for single-carrier saturation at beam edge in dBW
 G/T_{es} Earth station gain-to-noise temperature ratio in dB/K
 $G/T_{sat.}$ Satellite gain-to-noise temperature ratio at beam edge in dB/K
 $G.A.|_D$ Down-link geographic advantage for a typically oriented earth station in a spot beam
 $G.A.|_U$ Up-link geographic advantage at beam edge (global beam)
gain 1 m^2 Effective gain over isotropic of a 1-m^2 antenna at 6 GHz in dB
 P_E Earth station e.i.r.p. in dBW required to reach the transponder operating flux density
 $PL|_{4\text{GHz}}$ Path loss at 4 GHz
 $PL|_{6\text{GHz}}$ Path loss at 6 GHz
pWp Picowatt psophometrically weighted
 W_s Flux density for single-carrier saturation in dBW/m²
 $1/k$ $1/\text{Boltzmann's constant} = 1/(1.38 \times 10^{-23} \text{ joule/K})$
 $= -10 \log k$
 $= 228.6 \text{ dBW/K-Hz}$

References

- [1] "Performance Characteristics of Earth Stations in the INTELSAT IV System," ICSC-45-13 (Rev. 1), 23 June 1973.
- [2] N. K. M. Chitre and J. C. Fuenzalida, "Baseband Distortion Caused by Intermodulation in Multicarrier FM Systems," *COMSAT Technical Review*, Vol. 2, No. 1, Spring 1972, pp. 147-172.
- [3] J. C. Fuenzalida, O. Shimbo, and W. L. Cook, "Time-Domain Analysis of Intermodulation Effects Caused by Nonlinear Amplifiers," *COMSAT Technical Review*, Vol. 3, No. 1, Spring 1973, pp. 89-143.

Martin P. Brown, Jr. received his B.E.E. degree from the Georgia Institute of Technology in 1966. Before entering the service, he worked with IBM at Cape Kennedy on the Saturn V launch vehicle. From 1967 to 1971, he served as an engineering communications officer with the U.S. Air Force. He joined COMSAT Laboratories in 1971 and is presently a systems engineer with the International Systems Division studying multicarrier transmission impairments.



Mr. Brown is active in C.C.I.R. Study Group IV and the Aerospace and Electronics Systems Group of the IEEE. He is a member of the AIAA and a registered professional engineer.

Index: earth stations, propagation, statistical distribution, radiometers, rainfall, attenuation.

15.3-GHz precipitation attenuation measurements using a transportable earth station at Utibe, Panama

H. J. MEYERHOFF, A. BUIGE, and E. A. ROBERTSON

(Manuscript received October 17, 1973)

Abstract

A measurement program to collect propagation data at 15.3 GHz using a transportable earth station at Utibe, Panama, is described.

Data were collected over an interval of approximately one year. Attenuation measurements were obtained by using a radiometer whose output was proportional to the sky noise temperature. The antenna was pointed at one position to obtain a constant reference point. The attenuation measurements were correlated with regional rainfall data, and plots of various statistical distribution functions linked rainfall rate to attenuation at 15.3 GHz. The results of this program provided estimates of the gain margin required to achieve a certain link availability for tropical earth stations using higher frequencies.

Introduction

As part of the INTELSAT project on propagation research, COMSAT Laboratories conducted a measurement program using a transportable

This paper is based upon work performed in COMSAT Laboratories under the sponsorship of the International Telecommunications Satellite Organization (INTELSAT). Views expressed in this paper are not necessarily those of INTELSAT.

The servo power amplifier, located in the shelter's equipment rack, is operated by the control indicator unit. It utilizes 200-W, solid-state linear amplifiers in each axis. The panel contains circuit breakers, "ON" indicators, and overheating indicators for both axes.

The antenna assembly consists of a 3-m-diameter, solid-surface, aluminum paraboloid; a 15.3-GHz focal point feed; a polarization rotator; and a pedestal-to-reflector adapter. The antenna position can be adjusted to any direction between horizontal and vertical. The antenna gain is a minimum of 48 dB with a nominal 0.5° half-power beamwidth, and the maximum VSWR is 1.5 to 1. The feed attaches to the vertex area of the reflector and is also supported by three stainless steel guy rods between the end of the feed and the reflector surface.

Receiver subsystem

The radiometer receiver subsystem consists of an RF down-converter, a Dicke switch, a tunnel diode amplifier, and a single-sideband mixer (SSM)/preamplifier. The SSM permits a single down-conversion from 15.3 GHz to 60 MHz while maintaining at least 20-dB image rejection. The IF bandwidth is 60 MHz. A solid-state calibration noise source is provided for increasing the effective antenna temperature by 290K. All of this equipment is contained in a temperature-controlled equipment enclosure at the antenna assembly.

Radiometer subsystem

The A.I.L. (Airborne Instrument Laboratories) radiometer subsystem receives 60-MHz input signals from the receiver subsystem. A ferrite switch preceding the RF down-converter is used as a Dicke switch in the radiometer mode to switch between the antenna input signal and the reference signal at a 400-Hz rate. The radiometer output may be recorded on a stripchart or on magnetic tape. Both switched and total power measurement modes are available. For the measurements described in this paper, the system was operated in the switched mode.

Output data and recording subsystem

The output data and recording subsystem consists of the following units:

- a. computer,
- b. D/A converter,
- c. teletype terminal,
- d. stripchart recorder,
- e. counter,
- f. monitor panel.

These units are contained in the shelter's equipment cabinets. The computer is a 16-bit-word unit containing a 4,000-bit memory. Communication with the computer is established through a model 33 teletype terminal. Pedestal position data from the antenna are loaded into 14-bit optical encoders. The two encoder inputs are then multiplexed into a common buffer by the computer. Digital error signals are separately buffered into two 8-bit D/A converters.

Command, control, and power subsystem

The command, control, and power subsystem consists of the model 33 teletype terminal, the manual and automatic control provisions (including the mode control and monitor panel), and the input power, lighting, and air conditioning subsystem. It may be operated in either manual or automatic programmed modes. In the programmed modes the model 33 terminal is used to load commands into the system via the computer.

Techniques for attenuation measurement

The original specifications for this experiment called for a relatively simple, low-cost, transportable, 15.3-GHz receiving system for measuring atmospheric attenuation from the NASA ATS-5 satellite transmissions. Because of the limited availability of the ATS-5 satellite, most of the attenuation data were obtained from radiometric measurements of increases in sky noise temperature with the antenna pointed at the mean position of ATS-5 at an elevation angle of 55° . The increases in sky noise temperature were converted to rain attenuation by using the technique described in the following paragraphs.

The ATS-5 satellite beacon was monitored for two brief periods. During one 45-minute period no attenuation occurred. During the second period a severe storm passed over the terminal five minutes after acquisition of the ATS-5 signal. The satellite signal was attenuated by more than the dynamic range of about 12 dB. The satellite was turned off before reacquisition could be accomplished.

Attenuation derived from antenna temperature measurements

Radiometric measurements of rain attenuation can be obtained in two ways. In the experiment described in this paper the increase in the sky noise temperature viewed by the antenna when the antenna beam is intercepted by precipitation was measured. During these measurements, the antenna azimuth and elevation were fixed in the approximate direction of ATS-5.

Attenuation data can also be obtained by measuring the attenuation of noise power from a celestial source such as the sun. This technique has been successfully employed by several experimenters [2], [3]. However, measurements utilizing the sun can be obtained only during daylight hours. Furthermore, the data are obtained over a continually varying azimuth and elevation angle. Therefore, for the experiment described here no measurements were obtained by using the sun as a signal source.

Since sky noise temperature measurements are only an indirect measurement of attenuation, a discussion of the factors which are involved in converting sky noise temperature to attenuation is appropriate. As described in the previous section, a Dicke switch radiometer has been used to measure the sky noise temperature in this experiment. When the radiometric receiver is used, the output of the radiometer is roughly proportional to the noise temperature at the input of the Dicke switch. This noise temperature is related to various systems and atmospheric parameters by the relationship

$$T_{\text{meas}} = \left(1 - \frac{1}{L_f}\right) T_f + \frac{1}{4\pi L_f} T_g \left[\int_{\text{ground}} G(\Omega) d\Omega + \int_{\text{sky}} T_b(\Omega) G(\Omega) d\Omega \right] \quad (1)$$

where T_{meas} = noise temperature at the input to the Dicke switch

T_f = physical temperature of the antenna feed system

T_g = approximate physical temperature on the ground

$T_b(\Omega)$ = brightness temperature of the medium surrounding the antenna as a function of the solid angle Ω

L_f = loss ratio in the antenna feed system

$G(\Omega)$ = antenna gain as a function of the solid angle Ω .

In equation (1) the quantity which is related to rain attenuation is the term $T_b(\Omega)$. If the rain were a perfect absorber (i.e., if there were no scattering), then the relationship between the brightness temperature and the attenuation would be

$$T_b(\Omega) = \int_0^{\infty} \left\{ \alpha(\Omega, r) T_r(\Omega, r) \exp - \left[\int_0^r \alpha(\Omega, t) dt \right] \right\} dr \quad (2)$$

where α is the power absorption coefficient of the rain and T_r is the actual temperature of the rain at a given point in space. The ratio of energy absorption to energy scattering at 15 GHz varies with rainfall rate, however.

Over the range of 10–50 mm/hr, the ratio is never less than 4:1 even at the highest rain rates [4].

Equation (2) can be simplified by employing the following assumptions:

- the average temperature in the direction Ω is $T_r(\Omega)$,
- the equivalent cloud thickness in the direction Ω is S ,
- the average power absorption through the cloud in the direction Ω is $\alpha(\Omega)$.

The resulting relationship between brightness temperature and attenuation is

$$T_b(\Omega) = \left[1 - \frac{1}{L_r(\Omega)} \right] T_r(\Omega) \quad (3)$$

where $L_r(\Omega) = e^{\alpha(\Omega)S}$ is the attenuation through the rain in the direction Ω .

Equation (3) provides a simple means of estimating $L_r(\Omega)$ if $T_b(\Omega)$ can be obtained by measuring the input noise temperature according to the method described previously. To obtain $T_b(\Omega)$ from equation (1), the second term on the right-hand side of the equation must be known. Also, the antenna should have a narrow beamwidth so that its response is minimal except in the direction $\Omega = \Omega_0$ in which the attenuation $L(\Omega_0)$ is to be measured.

For a good horn reflector antenna with a narrow beamwidth, $L_f \simeq 1$, and $\int_{\text{ground}} G(\Omega) d\Omega \simeq 0$. Hence, the measured noise temperature becomes

$$T_{\text{meas}} = \frac{1}{4\pi} \int_{\text{sky}} T_b(\Omega) G(\Omega) d\Omega \simeq T_b(\Omega_0) \quad (4)$$

where Ω_0 is the direction of the antenna main beam axis.

It is important to realize that the use of equation (3) can still result in errors in attenuation estimates. The most important of these errors is attributed to energy scattering from raindrops. This scattering contributes to the transmission loss through a rain storm, but does not directly add to the brightness temperature. Moreover, this effect is partly neutralized because the drops scatter radiation from the ground into the antenna; thus, the noise temperature again increases.

Additionally, if the loss through a rain storm is large in every direction, then a large amount of multiple scattering occurs and some of the energy is absorbed at each scattering. Since the loss is high in every direction, almost none of the energy which is scattered from each drop emerges from the cloud. This suggests that the energy is all eventually absorbed and that, as a result, the cloud appears as a black body at the physical temperature of

the rain. Based on these very qualitative arguments, equation (3) should be valid for losses greater than about 3 dB. For lower losses, however, scattering should result in a value of $T_b(\Omega)$ which is smaller than that predicted by equation (3).

It should also be noted that the physical temperature of rain is not a constant, but decreases with increasing altitude. This means that, when losses are high, the receiving antenna sees primarily the radiation from drops which are low in the atmosphere; hence, the effective T_r to be used in equation (3) will be larger than it would be for lower losses. Additionally, since the lower drops are more effective in scattering radiation from the ground into the antenna, the contribution of ground radiation to $T_b(\Omega)$ will be higher (assuming that the ground is warmer than the rain).

The preceding discussion indicates that a unique relationship between $T_b(\Omega)$ and $L_r(\Omega)$ in equation (3) probably does not exist, and that the values for T_r which are used in equation (3) should at least be a function of $L_r(\Omega)$. Since T_r is also a function of altitude, for a given storm and for a particular value of Ω , $T_b(\Omega)$ and T_r will depend upon the distance of the storm from the antenna even if $L_r(\Omega)$ is constant.

In addition to the problem discussed in the preceding paragraph, the effect of the finite antenna beamwidth must be considered. In short, the quantity of interest is generally the loss which is experienced by transmissions to and from a point source, that is, a specific $L_r(\Omega_0)$, in the rain. However, radiometric techniques actually measure a quantity which is proportional to the loss, but which is weighted by the antenna gain pattern and integrated over the entire sky. At best, the radiometer output is proportional to the average loss through the region subtended by the main beam of the antenna. This value may be more or less than the loss in the direction of a satellite. Therefore, a large antenna should provide radiometric measurements which are more closely related to $L_r(\Omega_0)$ than those of a smaller antenna.

For losses less than approximately 10 dB, radiometric measurements provide reliable estimates of the path loss to a satellite. The major uncertainty is the proper value for the physical temperature of the rain. This value is determined experimentally from data for very intense storms which produce high attenuation. Equation (3) shows that, during high attenuation, $T_b(\Omega)$ reaches a limiting value. This limiting value, experimentally determined from a series of heavy storms, is used in equation (1) to convert the sky noise temperature measurements to attenuation.

The long-term attenuation data collected from radiometric measurements in this experiment will be summarized in the following section.

Presentation of reduced data

The raw data were analyzed to provide the following outputs:

- distribution function for attenuation,
- fade duration histogram,
- fade occurrence histogram.

The distribution function indicates the percentage of time during which the attenuation can be expected to exceed a given value. The fade duration and fade occurrence histograms provide statistical information concerning the distribution of the attenuation over the observing time, i.e., the duration of a particular depth of fade and the time of day when the fades occur.

Attenuation data derived from radiometric measurements were obtained for the period of 23 September 1971 to 29 June 1972, during which six separate equipment failures occurred. Most of the outage, corresponding to 7.4 percent of this interval, occurred during the period of 17 April 1972 to 5 May 1972 and was caused by air conditioner failure. Some rain attenuation statistics were lost, but the effect of this loss is not considered to be appreciable.

For radiometric measurements, the antenna was pointed at the mean position of ATS-5 at an elevation angle of 55°. Table 1 lists the number of minutes for which the attenuation exceeded given dB values up to a maximum of 10 dB (the limit for the radiometric technique).

TABLE 1. TOTAL MINUTES ATTENUATION AT 15.3 GHz EXCEEDS INDICATED VALUES (SEPTEMBER 23, 1971-JUNE 29, 1972, UTIBE, PANAMA)

Month	Minutes Attenuation Exceeds Indicated Values									
	1 dB	2 dB	3 dB	4 dB	5 dB	6 dB	7 dB	8 dB	9 dB	10 dB
September 1971	514	260	194	151	128	104	85	78	62	48
October 1971	2,027	807	521	416	338	269	206	171	126	84
November 1971	929	694	514	396	297	237	177	152	126	88
December 1971	21	14	12	7	1	0				
January 1972	78	20	7	4	1	0				
February 1972	62	44	42	41	37	35	28	27	17	11
March 1972	90	37	24	17	11	7	2	1	0	
April 1972	334	179	118	68	51	48	46	45	41	40
May 1972	704	379	285	219	186	158	136	122	100	80
June 1972	965	444	288	194	140	107	93	65	38	23

Rain data were available twice daily at Tocumen Airport, which is six miles from the Utibe earth station, as indicated in Figure 2, and hourly at Balboa Heights, 20 miles from the Utibe earth station. The average monthly rainfall for Tocumen and Balboa Heights shows considerable variation, but there is a similarity between the hourly distribution of rain and fade durations greater than 4 dB over a 24-hour period at Balboa Heights and Utibe, respectively (see Figures 3 and 4). The time shift of one hour in hours of peak rainfall and hours of maximum minutes of attenuation may result from the 20-mile separation between the locations at which rainfall and attenuation were measured. This shift also becomes apparent when the distribution for the number of rainfall hours measured over a 24-hour period at Balboa Heights (Figure 5) is compared with the fade durations measured at Utibe.

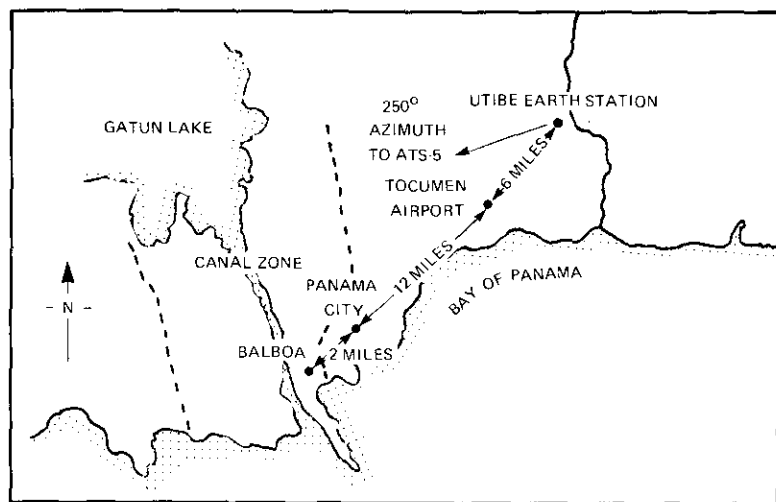


Figure 2. Regional Map of Utibe, Panama

On the basis of these similarities, the rain data available at Balboa Heights will be considered to apply to the Utibe earth station in an average statistical sense. For correlating rain data with attenuation statistics, the useful parameter is the instantaneous rain rate. The data at Balboa Heights are measurements of hourly rainfall, which can be converted to instantaneous rain rate by using a curve-fitting procedure that has been found to give reasonably accurate results [5]:

$$P = P_0 R^{-K} \tag{5}$$

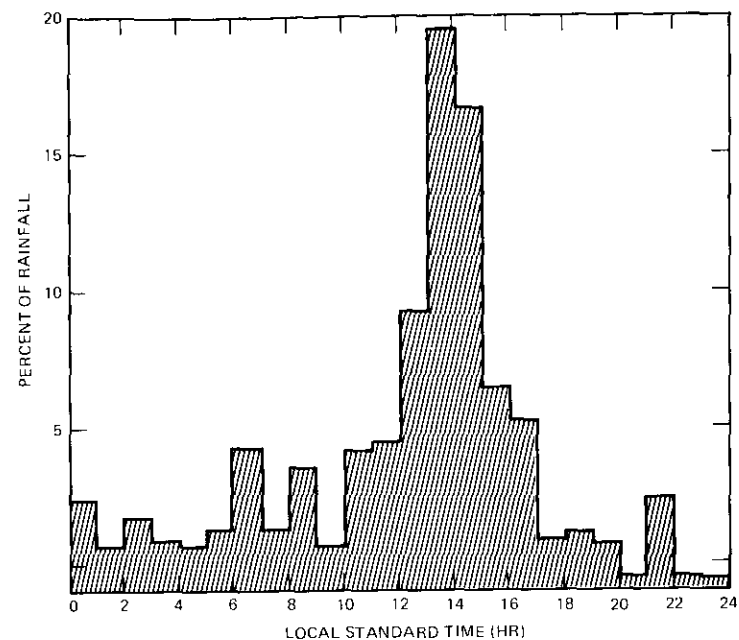


Figure 3. Percentage of Rainfall at Balboa Heights, Panama, over a 24-Hour Period

where $K = \frac{6.5}{R_0 + 1.5}$

R = rain rate in mm/hr measured over an hourly interval

R_0 = average rain rate in mm/hr
= total rainfall divided by the number of hours in which it rained

P_0 = percentage of time in hours during which it rained from September 1971 to June 1972

P = percentage of time during which the instantaneous rain rate was exceeded.

Hourly and instantaneous curves for the rain rate are plotted in Figure 6.

The data from Table 1 have been plotted in Figure 7 to show the percentage of the time during which attenuation exceeds the values given in the abscissa. Combining these results with those of Figure 6 makes it

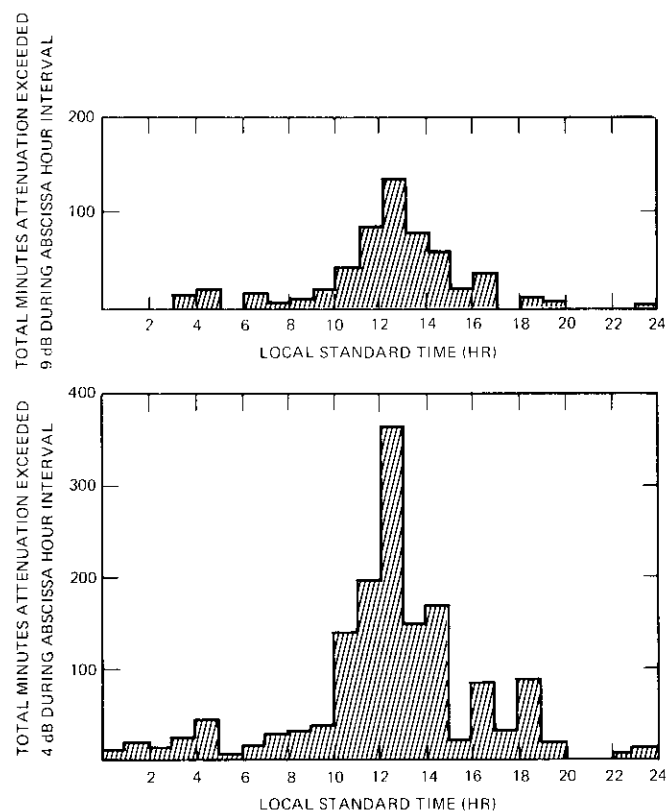


Figure 4. Distribution of Fades Throughout the Day at 15.3 GHz, Utibe, Panama

possible to obtain a curve of attenuation in dB versus instantaneous rain rate (Figure 8).

Figure 7 shows that 10-dB attenuation was exceeded during 0.1 percent of the time (or about nine hours per year) at a frequency of 15.3 GHz. The 1971 WARC allocated the 14-GHz frequency band for the up-link and the 11-GHz frequency band for the down-link to be used by satellite services. On the basis of theoretically derived scaling relationships, attenuation of 8.3 dB at 14 GHz and 5.1 dB at 11 GHz could be expected to occur during 0.1 percent of the time at Utibe.

Figure 9 provides fade duration histograms for fades of 4 and 9 dB. It can be seen that several fades of each depth exceeded 10 minutes.

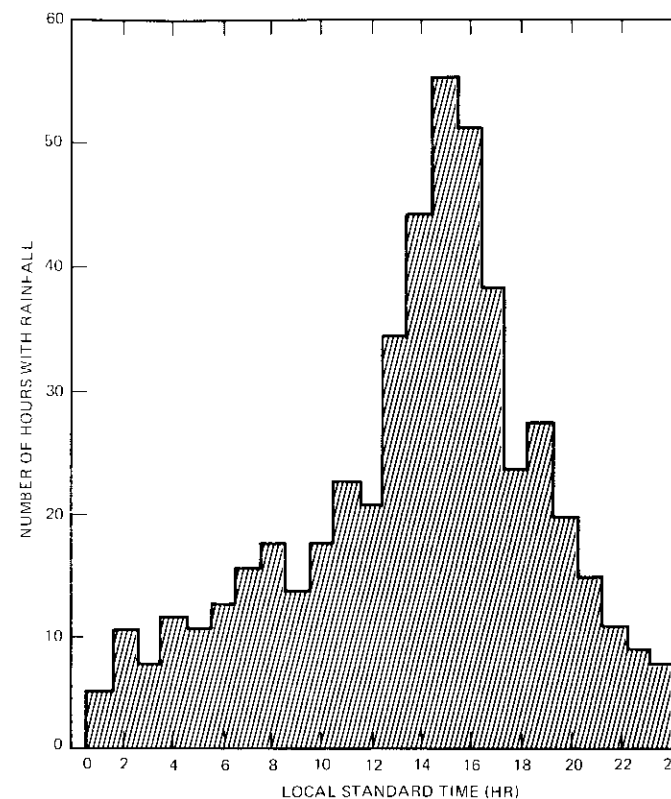


Figure 5. Distribution of Hours with Rainfall over a 24-Hour Period (September 1971-July 1972)

Figure 4 breaks down the minutes of 4- and 9-dB attenuation according to the hours during which they occurred. It can be seen that most of the thunderstorm activity occurs during the midday hours between 10 AM and 3 PM local time.

Conclusion

Propagation attenuation measurements were taken at Utibe, Panama, over a period of approximately one year using a 15.3-GHz transportable earth station. The attenuation data were obtained with a radiometer whose output was proportional to the sky noise temperature. Utibe was selected as a tropical site for which rain statistics were available.

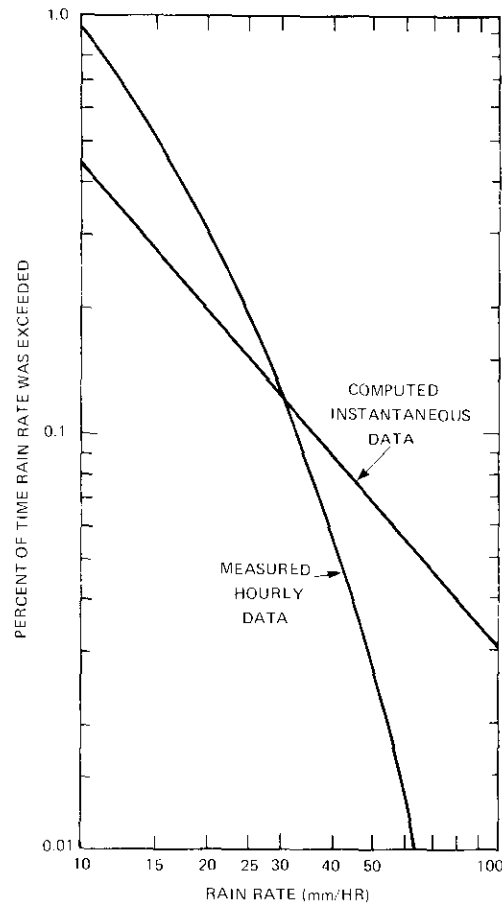


Figure 6. Percentage of Time During Which the Rain Rate was Exceeded at Balboa Heights, Panama

The antenna was pointed at the mean position of ATS-5 at an elevation angle of 55° . The number of minutes that the attenuation exceeded various dB levels was recorded, and distribution functions were plotted up to a maximum attenuation of 10 dB. Thus, it was found that 4-dB attenuation was exceeded during 0.4 percent of the time, while 10-dB attenuation was exceeded during 0.1 percent of the time. The rainfall rate distribution function was also plotted from rainfall data available on an hourly basis at neighboring Balboa Heights. A simple curve-fitting procedure made it

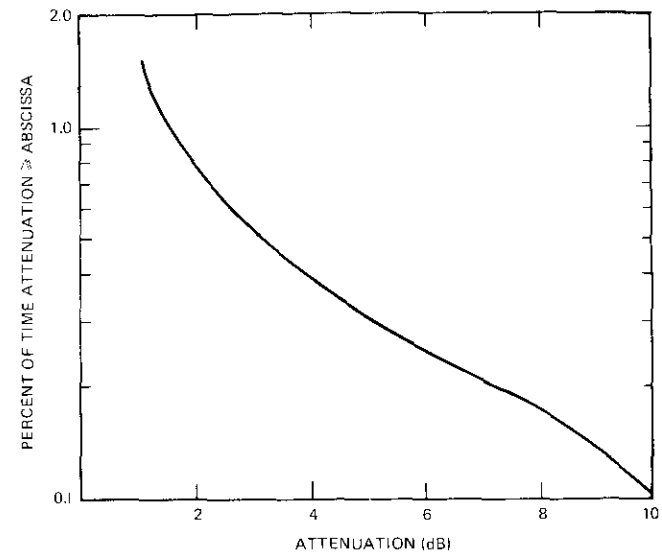


Figure 7. 15.3-GHz Attenuation Statistics for Utibe, Panama

possible to transform this function into an equivalent instantaneous rain rate distribution function which, combined with the attenuation distribution function, yielded a plot of instantaneous rain rate versus attenuation at 15.3 GHz.

A good correlation between the distribution of hourly rainfall over a 24-hour period at Balboa Heights and the distribution of fade durations greater than 4 dB at Utibe was obtained.

References

- [1] R. C. Medhurst, "Rainfall Attenuation of Centimeter Waves: Comparison of Theory and Measurement," *IEEE Transactions on Antennas and Propagation*, AP-13, July 1965, pp. 550-564.
- [2] R. W. Wilson, "Sun Tracker Measurements of Attenuation by Rain at 16 and 30 GHz," *Bell System Technical Journal*, Vol. 48, No. 5, May-June 1969, pp. 1383-1404.
- [3] P. G. Davies, "Radiometer Studies of Atmospheric Attenuation of Solar Emission at 19 GHz," *Proceedings of IEE*, Vol. 118, No. 6, June 1971, pp. 737-741.

- [4] D. E. Setzer, "Computed Transmission Through Rain at Microwave Frequencies," *Bell System Technical Journal*, Vol. 49, No. 8, October 1970, pp. 1873-1892.
- [5] A. Buige, "A Comparison of Precipitation-Scattered Signal Intensities and Surface Rainfall Rates," *Fall URSI Meeting*, December 1972.

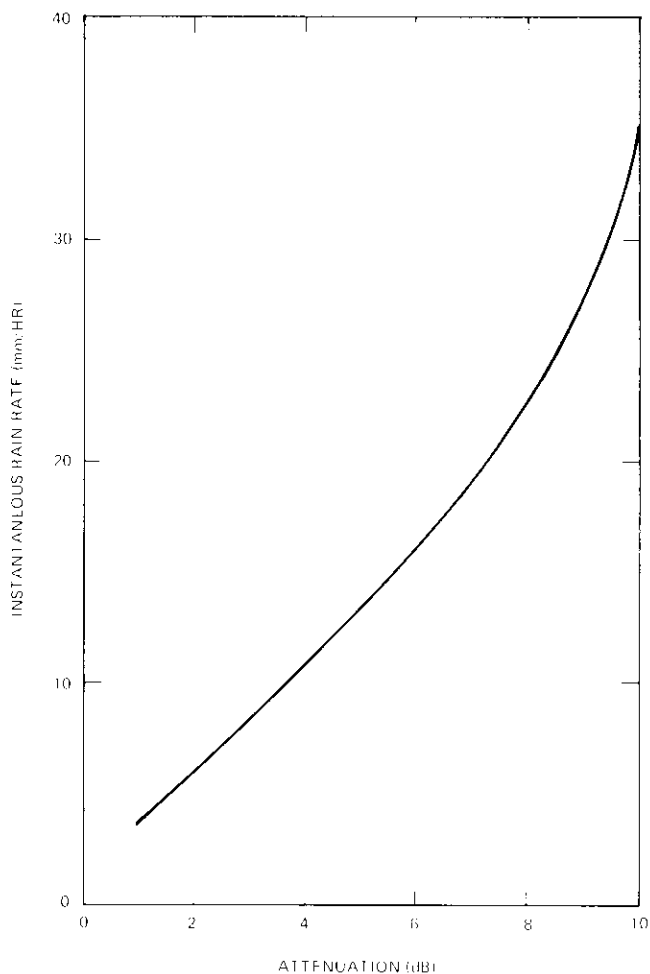


Figure 8. 15.3-GHz Attenuation vs Rain Rate

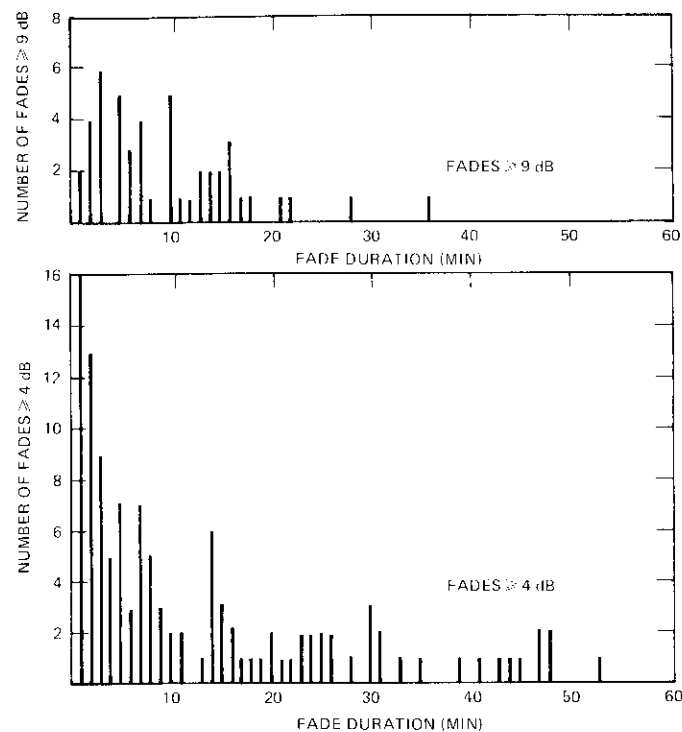


Figure 9. 15.3-GHz Fade Duration Histogram, Utibe, Panama



Henry J. Meyerhoff graduated from Edinburgh University with a B.Sc. with Honors in Electrical Engineering in 1956. He spent three years with Marconi's W. T. Co. Ltd., then, with the aid of a D.S.I.R. fellowship, received a Ph.D. in Automatic Control from Cambridge University in 1963. He is a member of IEEE and a former member of S.E.G. Since joining COMSAT Laboratories in 1968, he has worked on systems and propagation studies related to new satellite systems. He also has taught

postgraduate courses at Waterloo University, Ontario, and Rice University, Houston.



Anthony Buige received a B.S. degree in mathematics from St. Francis College in 1959. He spent seven years with the NASA Goddard Space Flight Center, where he was the Manager of the Data Acquisition Section in the Tracking and Data Systems Directorate. He joined COMSAT Laboratories in 1967 and was formerly Manager, Laboratory Simulation, in the Systems Division, engaged in transmission modeling and system simulation programs. Mr. Buige is presently the

Acting Manager for Telemetry and Command in the Space Segment Engineering Division of American Satellite Corporation. He is a member of IEEE and Delta Epsilon Sigma.

Ernest Robertson is Manager of the Space Systems Engineering Department of the Engineering Studies Division of COMSAT. Prior to assuming his present position, Mr. Robertson was a member of the Propagation Department of COMSAT Laboratories.

Before joining COMSAT Laboratories in 1969, Mr. Robertson was employed at Bell Telephone Laboratories, Whippany, New Jersey, as a member of the technical staff. He was involved in engineering and analysis of the performance of the SPARTAN missile subsystem of the SAFEGUARD Anti-Ballistic Missile System.

Mr. Robertson holds the Master of Science (1965) and the Bachelor of Science degrees (1963) from M.I.T.



CTR Note

R. R. TAUR

Rain depolarization: theory and experiment

Because of the rapid growth of commercial satellite communications, the allocated spectrum has become more and more crowded. The use of two orthogonal polarizations offers the possibility of expanding the communications capacity. However, rain and tropospheric turbulence can depolarize the electromagnetic waves. At 4 and 6 GHz, the oblate raindrops are the main cause of depolarization. This note presents certain theoretical predictions and the results of recent rain depolarization experiments.

One possible method of calculating the rain depolarization begins by obtaining the differential attenuation and phase shift between the polarizations along the major and minor axes of the nonspherical raindrops. The attenuation and phase shift are calculated by expanding the incident, transmitted, and scattered electromagnetic fields into a series of spherical vector wave functions, and the complex coefficients in the expansion are determined by matching the boundary conditions of finite points on the surface of the raindrop. Since the drop-size distribution of various rain rates is known, the effects of raindrops of various sizes can then be determined. A detailed description of this method is given by Oguchi [1]. Once the differential attenuation and differential phase shift are determined, cross-polarization discrimination for circularly polarized waves can be calculated by using the expression

This note is based upon work performed in COMSAT Laboratories under the sponsorship of the International Telecommunications Satellite Organization (INTELSAT). Views expressed in this note are not necessarily those of INTELSAT.

R. R. Taur is a Member of the Technical Staff of the Propagation Studies Department, Transmission Systems Lab, COMSAT Laboratories.

$$XPD = 20 \log \left| \frac{1 + e^{A+iB}}{1 - e^{A+iB}} \right| \text{ in dB} \quad (1)$$

where XPD = cross-polarization discrimination
 A = differential attenuation
 B = differential phase shift.

Equation (1) and the differential attenuation and phase shift data of Oguchi [2] are used to calculate the rain depolarization for normal incidence as a function of rain rate at 4, 6, and 11 GHz for assumed path lengths of 2.5, 5, and 10 km. Figure 1 is a plot of theoretical curves for circularly polarized waves at 6 and 11 GHz and path lengths of 2.5, 5, and 10 km. Figure 2 shows the theoretical values for circularly polarized waves at 4 GHz.

To test the theory, an experiment to measure the rain depolarization of a satellite-earth propagation path was implemented. A 4-GHz circularly polarized wave with axial ratio of about 1 dB was transmitted by the spot-beam antenna of an INTELSAT IV satellite. The receiving antenna, which was located at COMSAT Laboratories in Clarksburg, Maryland, separated the right- and left-hand circular polarizations so that the power levels of both polarizations could be monitored simultaneously. After approximately one year of observation, it was found that the experimental values generally agree with the theoretical predictions. However, theory yields higher values of cross-polarization discrimination. For example, in Figure 2 it can be seen that the recorded cross-polarization discrimination as a function of rain rate during the rainstorm on April 1, 1973, was generally lower than the theoretically predicted value calculated from the attenuation data. This difference is attributable to near-field effects, and to the error introduced by assuming ellipsoidal raindrops.

Acknowledgment

The author wishes to thank Dr. T. Oguchi for providing the most valuable rain attenuation and phase shift data. The author also wishes to thank Mr. E. Podraczky, who first suggested the experiment.

References

- [1] T. Oguchi, "Attenuation and Phase Rotation of Radio Waves Due to Rain: Calculations at 19.3 and 24.8 GHz," *Radio Science*, Vol. 8, No. 1, January 1973, pp. 31-38.
- [2] T. Oguchi, private communication.

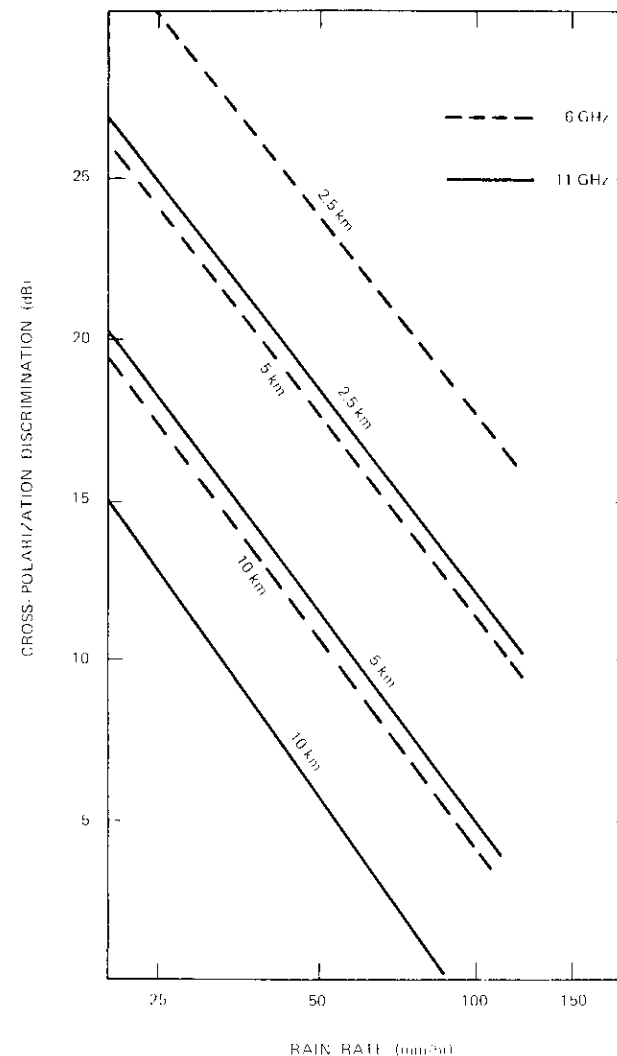


Figure 1. Theoretical Rain Depolarization for Circularly Polarized Waves

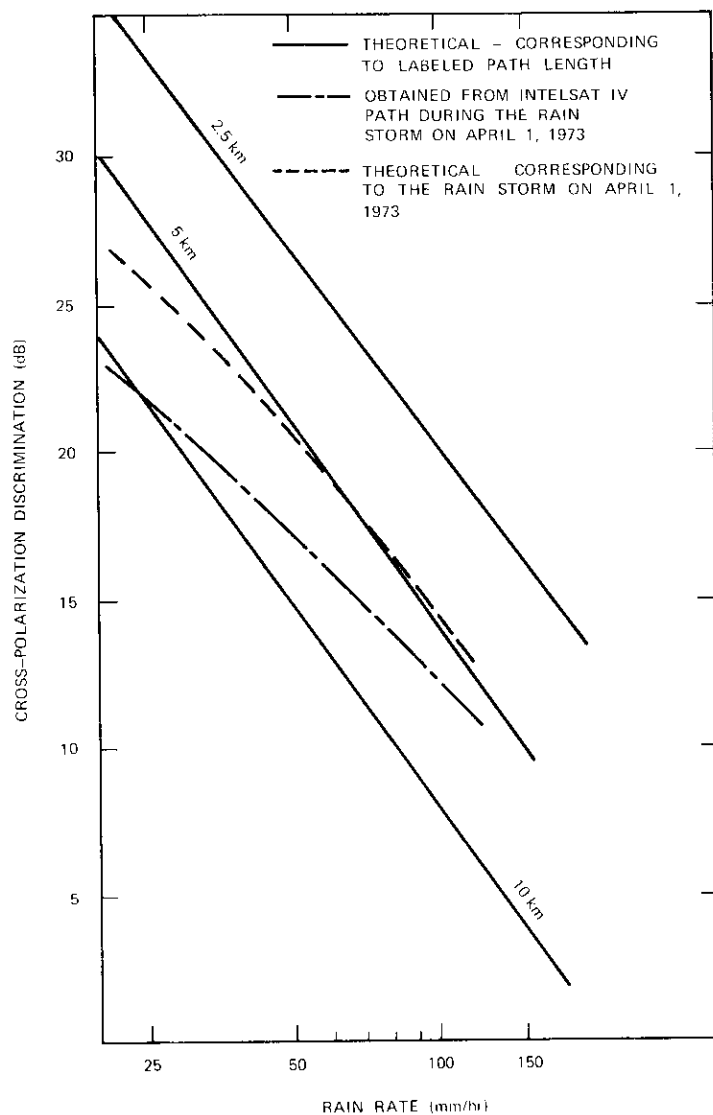


Figure 2. Theoretical Prediction and Experimental Results of Rain Depolarization for Circularly Polarized Wave at 4 GHz

Translations of Abstracts

Effet du couple dû au gradient de gravité sur un satellite INTELSAT IV en orbite de transfert

V. J. SLABINSKI

Sommaire

On calcule le couple dû au gradient de gravité sur un satellite à double rotation, en fonction des propriétés de masse de chaque partie. Des fonctions élémentaires fournissent le déplacement de l'axe de rotation qui en résulte en fonction de la position du satellite sur son orbite elliptique, ainsi que le déplacement de l'axe de rotation par période d'orbite. Des graphiques montrent le mouvement de l'axe de rotation du satellite INTELSAT IV F-4 dans son orbite très elliptique de transfert, et en orbite synchrone. Le déplacement net de l'axe de rotation en orbite synchrone a la valeur négligeable de 10^{-4} degrés/jour.

Les données du capteur solaire d'INTELSAT IV F-4 montrent que la direction de l'axe de rotation dans l'espace est déplacée de 0,05 degré à chaque passage au périégée, en orbite de transfert. Ceci est en accord avec la valeur théorique, compte tenu de la précision de mesure de 0,01 degré.

Aspects de stabilisation d'un système d'emmagasinage d'énergie et de stabilisation d'orientation utilisant des roues destiné aux satellites géostationnaires

M. H. KAPLAN

Sommaire

On présente une étude au point de vue de la stabilisation sur un système à roues pour l'emmagasinage d'énergie et la stabilisation d'orientation, destiné à une configuration de satellite géostationnaire, à stabilisation selon les trois axes par la rigidité gyroscopique du moment.

On suppose un système d'emmagasinage d'énergie et de commande d'attitude constitué de deux roues jumelées en contre-rotation ayant un moment résultant non nul. On a inclus les relations exprimant l'équilibre